Sediment accumulation rates and carbon burial in West Antarctic Peninsula fjords

Submitted by Matthew James Mason to the University of Exeter
as a thesis for the degree of
MSc by Research in Physical Geography
in December 2022

Word count: 18,506

Acknowledgements

First, I would like to thank my supervisor James Scourse for his continued support and mentorship over the past years and his many insightful comments and suggestions for this thesis. I would also like to thank Sev Kender for co-supervising this project, and for his advice over the course of this research. I'd also like to express my gratitude to Alejandro Román-González, not just for generously sharing his carbon data with me, but also for his support and help throughout the project on many other matters.

The team at the Consolidated Radio-isotope Facility (CORIF) at the University of Plymouth have been incredibly helpful over the course of this project, providing both analytical assistance and many insightful discussions regarding subsequent analysis and age-depth modelling. In particular I would like to thank Will Blake, Geoff Millward and Martha Hall.

On a similar note, the team at the University of Exeter Geography Radiometry Laboratory – Stephen Haley, Joana Zaragoza-Castells, and Karen Leslie – were very accommodating, despite the short-notice of my request to run further samples there, and for that I'm very grateful. In particular I would like to thank Karen for her kind offer to run the samples, saving me many hours of travelling from Cornwall to Streatham campus.

I would also like to thank all those involved with the ICEBERGS project for providing the cores analysed, and the SEACHANGE project for providing funding for the analysis at CORIF. Many of the researchers on both projects have also provided useful advice and suggestions, and I would specifically like to thank Kate Retallick, Katrien Van Landeghem, and Kirsty Penkman.

Abstract

Fjords act as palaeoenvironmental archives, recording past glacial histories in remarkably thick sediment accumulations. Furthermore, high primary productivity combined with rapid burial make fjords important organic carbon sinks. Reconstructing recent rates of sediment accumulation provides context for assessing past and future changes, and, in combination with measurements of carbon content, can inform on carbon sequestration potential. Recent research has indicated that fjords may represent areas of high carbon burial. However, these estimates are based on surface sediment carbon stocks combined with global averages of carbon preservation, without consideration of regional variability in burial efficiencies.

Here, seven sediment cores from three fjords on the Antarctic Peninsula are analysed. ^{210}Pb, a radio-isotope with a half-life of 22 years, is used to construct age-depth models and estimate rates of sediment mass accumulation. These data are then combined with measurements of core carbon content to estimate rates of modern carbon deposition and long-term carbon burial.

Core-averaged sediment mass accumulation rates ranged from 0.08 to 0.42 g cm^{-2} yr^{-1}. No long-term trends in accumulation rates were observed at any of the sites over the past century, though in Börgen Bay synchronous peaks in sedimentation rates were observed at similar ages across different sediment cores. At Marian Cove, South Shetland Islands, the typical proximal-distal gradient in accumulation rates was absent, suggesting a diverse source of sediments, most notably the input from pro-glacial meltwater streams from land-terminating ice.

Surface deposition rates of organic carbon ranged from 3 to 26 g C m^{-2} yr^{-1}. However, whilst surface sediment organic carbon flux was high, burial efficiencies were found to be significantly lower than those previously reported for other sites on the continental shelf, resulting in similar rates of long-term storage. This has important implications for our understanding of the carbon sequestration potential of high-latitude fjords.

Contents

List of Figures and Tables

Contribution declaration

Procedure	Person(s)	Location
Collection of Material	JR18003 JR19002	-
^{210}Pb Sample Preparation	Matthew Mason (Author)	University of Exeter (Penryn Campus)
Gamma Spectroscopy	Dr Martha Hall	University of Plymouth Consolidated Radio-isotope Facility (CORIF)
Gamma Spectroscopy	Dr Karen Leslie	University of Exeter Geography Radiometry Laboratory (Streatham Campus)
Carbon Analytics	Dr Alejandro Román-González	University of Exeter Geography Radiometry Laboratory (Streatham Campus)
Data Analysis and Interpretation	Matthew Mason (Author)	-

Chapter 1: Introduction

1.1 Background and Research Aims

The Antarctic Peninsula is a region of global significance regarding climate change, sea-level rise, and biodiversity (Barnes et al., 2020; Grange & Smith, 2013; Hock et al., 2009). Atmospheric temperatures have risen at a rate unparalleled elsewhere, with an increase of up to five times the global average (Turner et al., 2014). This, along with changes in oceanographic regime, has resulted in the widespread loss of ice-shelves (Cook & Vaughan, 2010) and the acceleration and retreat of glaciers in the region (Cook et al., 2016).

The Antarctic Peninsula ice sheet is primarily drained by steep, fast flowing tidewater glaciers, typically terminating into fjord systems. These are generally separated from adjacent shelf waters by one or more entrance sills, and as such act as natural sediment traps, preserving glacial sediment histories and providing important habitat for benthic species (Bianchi et al., 2020). Fjord systems on the West Antarctic Peninsula are typically highly productive, with fjord basins exhibiting substantially higher benthic megafaunal abundance than the open shelf (Grange & Smith, 2013).

The carbon sequestration potential of fjords has traditionally been overlooked in favour of more productive ecosystems such as mangrove swamps, seagrass beds and salt marshes, however recent studies have highlighted the importance of fjords in the global carbon cycle (Smith et al., 2015) and the potential of Antarctic fjords in mediating climate warming trends (Barnes et al., 2020). As ice retreats and new habitat is uncovered, these fjords may play an important role in mitigating climate change through the sequestration of ‘blue carbon’ (Nellemann et al., 2009) acting as a negative feedback on climate change (Barnes et al., 2020). Sediment yield and accumulation plays a dynamic role in this process by limiting productivity (Grange & Smith, 2013) while conversely increasing the percentage of captured carbon being successfully sequestered (Betts & Holland, 1991).

Sediment accumulation in tidewater glacier adjacent fjord systems is still relatively poorly understood and is influenced by various factors including geometry and oceanographic regime, climate, meltwater processes and sediment resuspension (Domack & Ishman, 1993; Eidam et al., 2019). Accurate estimations of modern sediment mass accumulation rates are important for informing reconstructions of past environments (e.g. Cowan et al., 2014), estimations of erosion rates (e.g. Koppes et al., 2015), and providing context for past and future changes in glacial dynamics (Boldt et al., 2013). Furthermore, when combined with measurements of sediment composition (e.g. carbon content), they can provide estimates of burial rates, important for calculating global marine budgets and informing biogeochemical models and palaeoceanographic reconstructions.

This study reports sediment mass accumulation rates and carbon fluxes in three glacimarine fjords on the West Antarctic Peninsula, and in doing so aims to:

- Determine modern rates of mass accumulation to provide context for past and future change
- Assess spatial and temporal variations or trends in mass accumulation rates and their causal factors
- Determine carbon deposition, burial rates, and burial efficiencies, and compare these with other sites in the region, and other fjords around the world.

1.2 Fjord Systems: A Review

Fjords are deep mid- and high-latitude estuaries that are excavated by glacial ice. They are typically long and narrow with steep sided inlets, though exhibit diverse morphologies ranging from simple straight troughs to branching, intricate systems (Domack & Ishman, 1993). Entrance sills are often present, which act to inhibit bottom currents and thus provide a degree of isolation from regional oceanographic conditions, resulting in complex and variable circulation patterns (Howe et al., 2010). Sills also act to trap sediment, allowing remarkably thick accumulations of up to hundreds of meters (Andrews et al., 1994).

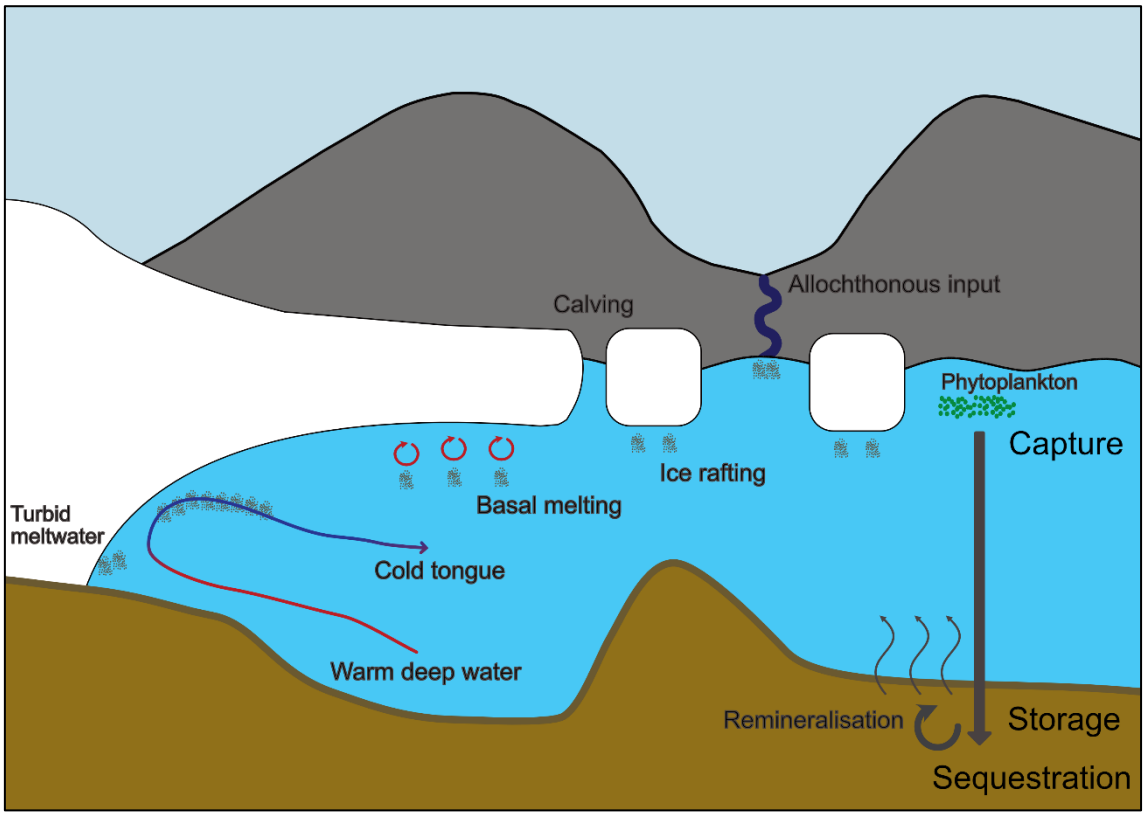

Figure 1.1. Physical and biological processes in polar and subpolar fjords. Author's own work.

1.2.1 Glacial Retreat in Fjords

Glacial retreat in fjords occurs primarily by subaqueous (basal) melt and ice-front calving (Benn et al., 2007; Rignot & Jacobs, 2002), with additional ice loss from surface ablation (Cook et al., 2005). Rates of basal melting are dependent on water temperatures at the marine-ice interface, the delivery of this water to the front, and the effectiveness of heat transfer across the water-ice boundary layer (Truffer & Motyka, 2016). These factors are highly spatially variable, explaining how glacial retreat rates can differ remarkably across a short spatial scale despite relatively similar climatic conditions. Cook et al. (2016) demonstrated a strong correspondence between mid-depth ocean temperatures and glacier front changes along the western coast of the Antarctic Peninsula using satellite and aerial imagery data. They showed that glaciers terminating in the relatively warm Circumpolar Deep Water (CDW) in the southern region of the Antarctic Peninsula exhibited greater ice loss than those terminating in the cooler Bransfield Strait

Water (BSW), a mixture of CDW and Shelf Water (SW) from the Weddell Sea, in the northern region of the Antarctic Peninsula.

On a local scale, the delivery of this warmer water to the glacier front is highly dependent on fjord morphology and the position of the grounding line of the ice. Where large submarine troughs are present, warmer, deeper water can readily access the ice front and produce enhanced basal melting, whilst this process is limited by the presence of one or more entrance sills (Pritchard et al., 2012). Similarly, the position of the ice grounding line and interior fjord geometry can have profound effects on glacial retreat, with the presence of submarine cavities greatly enhancing heat transfer and subsequent melting (Smith et al., 2017). Melt water plumes, driven by the positive buoyancy of meltwater, are the primary process driving the effectiveness of heat transfer across the water-ice boundary layer, and are strongly influenced by local geometry (Werner et al., 2018).

Ice-front calving is another key driver of glacial retreat in fjords. Calving occurs where fractures on the ice sufficiently propagate to isolate ice blocks from the main body of the glacier, which can occur by several methods (Benn & Astrom, 2018), principal of which are a down-stream change in resistance from the glacier bed, undercutting by basal melting, and torque arising from buoyant forcing. Thus, calving is most common where glaciers reach deep water or flow into a wider part of the fjord (Bianchi et al., 2020), and the rate of calving is heavily dependent on fjord morphology.

1.2.2 Hydrography in Fjords

Fjord hydrography - the processes of tides, Coriolis force, internal waves, and jets – is relatively poorly understood in Antarctic fjords but has been studied extensively in northern latitude fjords. Estuarine circulation is common in fjords: in summer, fjords are strongly stratified, with a layer of cold glacially-sourced freshwater overlying warmer salty oceanic water (Bianchi et al., 2020). This strong density gradient inhibits vertical mixing, thus decoupling the surface circulation from circulation at depth, and generating a pressure gradient causing outward surface flow. This is compensated by the inward flow of ocean water at mid-depth, with the resultant velocity shear inducing upward transfer of salinity

and volume via entrainment (Llanillo et al., 2019). Further water exchange between the fjord and the surrounding shelf waters is caused by low frequency density fluctuations at the fjord mouth. These pulses of ventilation are associated with depressed isopycnals, originating with a negative density anomaly and positive bottom pressure anomaly, preceded by along-shore, down-welling favourable winds on the shelf (Jackson et al., 2014).

Glacier-ocean interactions are an important control on internal fjord circulation, with significant buoyancy-driven flow from meltwater discharge (Cape et al., 2019). Meredith et al. (2022) have demonstrated that ice calving events may lead to significant mixing through the observed propagation and breaking of internal tsunamis, which is estimated to represent a process of equal magnitude to wind forcing in driving shelf mixing on the West Antarctic Peninsula.

The interaction between tidal action and fjord topography is another key driver of mixing in glacimarine fjords. Mortensen et al. (2011) identify the Subpolar Mode Water as an important local heat source for fjords around the Greenland Ice Sheet, with primary heat transfer being a result of deep tide-induced mixing at the outer sill region. In shallower systems, mixing is primarily a result of local wind stresses on surface waters, and in such circumstances ventilation of fjord bottom waters can be as rapid as 2.7 days (Gustafsson & Bendtsen, 2007). Sea ice formation and the resulting destabilizing buoyancy fluxes via salt rejection also result in some, albeit minor, mixing of water masses (Fer & Widell, 2007).

1.2.3 Sedimentation in Fjords

Terrigenous sediment production and accumulation in polar and subpolar fjords is driven by glacial erosion, and the subsequent delivery of these products to the fjord basin (Koppes et al., 2015). This is modulated by meltwater production, with increased meltwater resulting in a reduction in effective basal pressure and increased erosion (Benn & Evans, 2010). As such, the nature of glaciation at the head of the fjord dictates mass accumulation rates therein (Boldt et al., 2013).

Mid-latitude glaciers typically produce far greater sediment yields than sub-polar and polar glaciers, resulting in a latitudinal gradient of fjord mass accumulation

rates (Boldt et al., 2013). Furthermore, under changing climatic conditions fjords can transition from one type of system to another, which will be reflected in down-core mass accumulation rate variation. However, direct inference of glacial history from changes in sediment accumulation rates is complicated by the varied response of different systems to external forcings, with site specific factors often overriding general trends (Boldt et al., 2013). For example, an increase in sediment accumulation rate can be a result of both rapid deglaciation (Koppes & Hallet, 2006), and glacial advance during surging events (Humphrey and Raymond, 1994). This matter is complicated by the fact that as a glacier retreats (or advances) the distance from the core site to the glacier front will change, resulting in decreased (or increased) sediment reaching that location before settling. As such, even in sites with documented glacier retreat, there may be no apparent change in sediment accumulation rates (e.g. Boldt et al., 2013).

Subsequent deposition and redistribution of these sediments is driven by bathymetry, bay geometry and oceanographic regime (Domack & Ishman, 1993). Sedimentation in glacimarine settings is dominated by meltwater processes and ice-rafting. Sediment laden meltwater is discharged from the base of the glacier front, and its subsequent vertical trajectory is determined by its turbidity (and thus density). Generally, the meltwater is much less dense than the ambient seawater, and so rises as a positively buoyant forced plume. Upon reaching the surface it spreads as a radial surface gravity current (overflow), with sedimentation occurring according to grain-size and flocculation (Mugford & Dowdeswell, 2011). This typically results in drapes of sediment, conformable to the bottom topography (Bianchi et al., 2020). In cases of exceedingly high turbidity underflow currents can form (Mulder & Syvitski, 1995), or, under certain hydrographic regimes deep (saline) water can become entrained within submarine cavities, with consequent melting and sediment entrainment leading to the formation of intermediate-depth ‘cold tongues’ (Domack & Williams, 1990). Subsequent trajectory of these deeper flows (and thus sedimentation patterns) is dictated by fjord bathymetry, whereby submarine sills can limit dispersal, and, along with gravitational processes, cause ponding in bathymetric lows. Sediment rafting on ice-bergs is also an important mechanism by which coarser sands and gravels can be transported significant distances from the glacier terminus (Vermassen et al., 2019).

Bay geometry also plays an important role in determining sedimentation patterns. Fjords with a linear geometry (high length to width ratio) typically exhibit relatively simple sedimentation patterns, with deposits thinning exponentially down-fjord (Syvitski et al., 1985). Limited iceberg dispersal due to a barrier effect, whereby drifting ice accumulates at the narrow glacier terminus, results in low ice-berg rafted debris content towards the fjord mouth. The narrow width of these systems also limits the Coriolis effect, and the establishment of eddy circulation, further simplifying sedimentation patterns (Domack & Ishman, 1993). In fjords with complex bay geometries however, distinct intra-bay oceanographic regimes develop that result in the separation of terrigenous and biogenic material; mid- and deep-water turbid cold tongues and Coriolis deflection cause terrigenous sediments to accumulate in the inner fjord and along the western edges, whilst warm outer bays favour the productivity of phytoplankton in surface waters, with subsequent facies consisting of siliceous muds with ice-rafted debris (Domack & Ishman, 1993).

However, these typical patterns of fjord sedimentation are not always apparent. Eidam et al. (2019) found sedimentation rates in Andvord Bay to be highly spatially variable, interpreted to be the result of diverse sources of sediment input acting to dampen the typical proximal-distal gradient. Furthermore, Munoz and Wellner (2016) found an inverse relationship in Flanders Bay (West Antarctic Peninsula), with grain-size typically coarsening down-fjord, attributed to winnowing from currents adjacent to the fjord mouth.

1.2.4 Carbon in Fjords

Fjord systems are carbon burial hotspots, burying the largest amount of carbon per unit area in the world (Smith et al., 2015), and thus are considered key components of the global carbon cycle. Carbon in fjords can be divided into the autochthonous and allochthonous component. The autochthonous component (i.e. produced *in situ*) is derived primarily from phytoplankton production, with smaller contributions from macroalgae and sea ice-algae, whilst the allochthonous component is sourced from terrestrial plant tissue, petrogenic sediments, and glacier discharge (Berg et al., 2021; Cui et al., 2016).

Annual phytoplankton primary productivity is strongly related to light availability, driven primarily by the duration of the growing season (Eilertsen & Degerlund, 2010) as well as seasonal sea ice cover (Rysgaard et al., 1999) and turbidity (Cloern et al., 1987). Further interannual variation occurs as a result of variable supply of freshwater and the inflow of seawater resulting in variations in the mixed layer depth and stability (Costa et al., 2020; Hegseth & Tverberg, 2013). Nutrient availability also plays a key role in driving variations in phytoplankton production, with iron, required by phytoplankton for photosynthesis and nutrient assimilation, being the main limiting factor on phytoplankton growth during the summer months (Henley et al., 2020). This is highly spatially variable, with iron tending to be higher in regions with high rates of glacial melt and iceberg calving due to the release of iron-rich terrigenous material (Van der Merwe et al., 2019). Macronutrient (nitrate, phosphate and silicic acid) availability can also limit phytoplankton growth (Moore et al., 2013). On the West Antarctic Peninsula phytoplankton assemblages are dominated by diatoms, and productivity is characterised by intense periods of growth, known as blooms (e.g. Costa et al., 2020).

The organic carbon (OC) fixed from CO_2 by primary producers can then follow various pathways, eventually being either sequestered in the sediment, or, more commonly, broken down by microbes and re-released to the atmosphere as CO_2 or sequestered in the deep ocean as refractory dissolved organic carbon (Henley et al., 2020).

A small, but highly variable fraction of phytoplankton biomass can sink and be directly sequestered (Ducklow et al., 2007), whilst a greater proportion is grazed by zooplankton (Arendt et al., 2016). Zooplankton faecal pellets represent an important pathway for carbon sequestration. In the West Antarctic Peninsula krill are the dominant zooplankton, and population dynamics closely track diatom blooms. Owing to both the relatively large size of krill faecal pellets (and thus rapid sinking speed) and their occurrence in large swarms, a high proportion of krill faecal pellets (and the OC contained within) avoid fragmentation and ingestion and successfully sink to the seafloor (Belcher et al., 2019). Another key component of carbon sequestration in Antarctic fjords is via consumption by

benthic organisms (Ziegler et al., 2020), both infaunal (Zwerschke et al., 2022) and epifaunal (Barnes et al., 2020).

Allochthonous OC can constitute a significant portion of sedimentary carbon in fjords. In low latitude glacimarine fjords the transport of biomass and the erosion of active terrestrial soils can contribute over half of OC buried in fjord sediments (Cui et al., 2016; Zaborska et al., 2018), although this source is limited in Antarctica due to sparse vegetation cover and shallow or non-existent organic soils. Furthermore, supraglacial algae can fix carbon, which is then entrained within the meltwater and transported to the marine environment, where it may subsequently be buried within fjord sediments (Lamarche-Gagnon et al., 2019; Stibul et al., 2015; Yallop et al., 2012). Although this process is again more prominent at lower latitudes, substantial algal blooms have been observed on glaciers in the West Antarctic Peninsula (Gray et al., 2020).

Petrogenic OC, which has been sequestered in sedimentary (or metamorphic) rocks for millions of years, represents another important source in fjord sediments, as it can be eroded by glacial action. When exposed, some of this may be remineralised and released to the atmosphere as CO_2, while some will be exported into the marine environment where it may be re-buried, contributing to the standing stock of OC in the sediment (Berg et al., 2021). In one sub-Antarctic fjord (Cumberland Bay, South Georgia), Berg et al. (2021) found that up to 60% of fjord sediment OC was of petrogenic origin, with highest levels found proximal to the present-day calving front. It is important to note that whilst modern terrigenous and marine OC represent a potential sink for atmospheric CO_2, petrogenic OC is at best neutral (if successfully re-buried), or, if remineralised, a source.

For carbon that reaches the seafloor to be successfully sequestered it must be further buried below the activity of the microbial loop (Henley et al., 2020). Benthic remineralisation of OC follows a progression of distinct metabolic pathways as electron acceptors become utilised and depleted (Canfield & Thamdrup, 2009), the order of which is consistent, based on the thermodynamics (and efficiency) of the processes (Froelich et al., 1979). This general order of utilisation creates distinct redox zones within the sediment profile, termed the oxic, suboxic and

anoxic zones; whilst there is some overlap, each successive process does not begin in full effect until the electron acceptor for the proceeding process is exhausted (Canfield & Thamdrup, 2009).

The oxic zone, where oxygen is freely available, is dominated by aerobic respiration. Following oxygen depletion, in the suboxic zone, nitrate, manganese, and iron reduction processes dominate, though due to the limited supply of these species to ocean sediments these processes are typically not biogeochemically important (Jørgensen & Kasten, 2006). In the absence of oxygen, nitrate, manganese and iron redox species, reduction via sulphate, which is widely distributed in the ocean (Henrichs & Reeburg, 1987), becomes the primary method of carbon remineralisation. This too decreases with depth as sulphate is depleted, with the majority of sulphate reduction occurring at the top of the anoxic layer (Jørgensen & Kasten, 2006). On much longer timescales, where sediment is buried deep below the anoxic layer, methanogenesis can occur, whereupon methane slowly accumulates and diffuses upwards. Upon reaching the sulphate layer it is oxidised to carbon dioxide. Rates of methanogenesis are typically low, with estimates suggesting that 3-4% of global carbon flux to the seafloor undergoes this process (Egger et al., 2018).

Thus, as OC is buried deeper within the sediment, the rate of remineralisation decreases due to the efficiency of available redox processes, as a result of the progressive depletion of the different electron acceptors. This is exacerbated by the fractionation of the organic matter itself, whereby the more labile components are preferentially respired, leaving behind only the more refractory organic matter, which is inherently resistant to degradation (Burdige, 2007). Resultingly, OC within the upper sediment layers is far more susceptible to remineralisation whilst the OC buried at depth is likely to remain sequestered. Typically, after 80-100 years carbon remaining within the sediment is likely to avoid further remineralisation (Koziorowska et al., 2018), though ultimately this constitutes only a small fraction of the carbon originally deposited.

There are various processes which may affect the fraction of OC that successfully avoids remineralisation (burial efficiency) and becomes buried deep within the sediment (sequestered). Processes influencing the depth of the oxic zone, and

thus the length of time accumulating particles are exposed to oxygen and aerobic respiration, are considered the most influential (Hartnett et al., 1998). The most important parameters which influence the depth of the oxic zone are the O_2 concentration of bottom waters, flux of organic matter (higher fluxes result in more rapid utilisation and depletion of oxygen), and sedimentation rate. Interestingly, sedimentation rate has been found to be far more influential on OC burial rates than the other two factors (Toth & Lerman, 1977; Müller and Suess, 1979; Henrichs & Reeburgh, 1987; Canfield, 1989; Betts & Holland, 1991), due to the rapid burial of freshly deposited material beneath the oxygenated layer (Arndt et al., 2013). Another important process is the adsorption and co-precipitation of dissolved organic carbon to iron (Bianchi et al., 2020): up to 20% of total organic carbon in sediments may be bound to iron, indicating that such processes may enhance long-term burial (Lalonde et al., 2012; Faust et al., 2021).

Macrofauna also play a role, acting to both increase and decrease carbon burial efficiencies through conflicting processes. Bioturbation of sediments, through burrowing and feeding activity, results in organic matter being repeatedly exposed to oxygen when transported towards the surface, as well as introducing oxygenated porewaters to greater depths (bio-irrigation) (Jørgensen & Kasten, 2006). Furthermore, a process known as priming, whereby the introduction of fresh organic matter to older deposits can stimulate the degradation of refractory organic matter, is also considered important (Burdige, 2007). Conversely, though, the production of tube linings, halophenols, or body structural products could act to inhibit degradation (Arndt et al., 2013). Additionally, it has been hypothesised that infaunal benthos may enhance the rapidity at which fresh organic matter is buried below the oxic layer through physical downward transport (Zwerschke et al., 2022).

In Antarctica, the sequestration potential of fjords may act as an important negative feedback on climate change. Barnes et al. (2021) identify three potential negative feedbacks on climate change in Antarctica: sea-ice loss, ice-shelf loss, and glacier retreat. Sea-ice loss is identified to have the most sequestration potential (60-100 Mt C yr^{-1}), with increased light penetration resulting in enhanced phytoplankton blooms. Sub ice-shelf communities are typically sparse and slow growing, limited by both nutrient and light availability: ice shelf disintegration can

lead to substantial increases in productivity, which, along with the creation of new habitat by dropstones (Ziegler et al., 2017), and ocean fertilisation by iceberg melt (Duprat et al., 2016) is considered to have the sequestration potential for 4-40 Mt C yr^{-1}, even after accounting for the negative impacts of iceberg scouring on benthic communities (Barnes & Souster, 2011). Finally, glacier retreat is identified as a smaller, yet poorly constrained negative feedback mechanism. As tidewater glaciers retreat, new phytoplankton blooms occur driven by increased light and nutrient input. Furthermore, new benthic habitat emerges from beneath the previously grounded ice (Grange & Smith, 2013; Barnes et al., 2020), further enhancing sequestration potential. Benthic organisms are likely to be particularly effective at sequestering carbon, due to their inherent proximity to the seabed (Zwerschke et al., 2022).

Over 90% of glaciers on the West Antarctic Peninsula are retreating (Cook et al., 2016). Although this is a comparatively small amount of marine-ice loss compared to the wider Antarctic Peninsula shelf seas, the setting in which it is occurring (fjords) may allow for a disproportionately high level of carbon sequestration, estimated at ~1 Mt C yr^{-1} (Barnes et al., 2021). However, due to limited experimental and observational data this is highly uncertain, and is complicated by potential negative effects of glacier retreat on benthic communities such as freshening and high sediment loads (Sahade et al., 2015), and the release of carbon trapped in glacial ice (Legrand et al., 2013).

1.3 ^{210}Pb Dating

1.3.1 Principles of ^{210}Pb Dating

^{210}Pb dating is a form of uranium-series dating concerned with the decay chain from ^{210}Pb to ^{206}Pb. Radon gas (^{222}Rn) escapes from the earth's crust and enters the atmosphere, where it decays to the solid ^{210}Pb. This is subsequently removed from the atmosphere via precipitation, deposited into the water column, and adsorbed onto suspended particulate matter. Upon burial, this sediment is closed off from the supply of ^{210}Pb from the atmosphere and thus the system becomes closed. ^{210}Pb is an unstable isotope of lead, and decays with a half of life of 22 years to form stable ^{206}Pb. As such, the concentration of ^{210}Pb in a particular

sediment layer relative to surface concentrations can be used to provide an estimate of the time that has elapsed since deposition occurred (Walker, 2005).

The use of ^{210}Pb as a geochronometer was first demonstrated by Golberg (1963), who applied this theory to a core from the Greenland Ice Sheet covering a period of roughly 20 years, with the data acquired in agreement with the stratigraphic evidence at the site. This technique was further developed by Crozaz et al. (1964) on Antarctic ice cores, demonstrating its viability over a span of around 200 years. The first application of this technique to marine sediments was by Koide et al. (1972) on varved deposits from the Santa Barbara basin, which provided a robust, independent chronology against which the accuracy of ^{210}Pb dating, and the validity of assumptions concerning it, could be assessed. The results showed a close correlation between the ages determined from ^{210}Pb dating and those from the varves, demonstrating the suitability of the ^{210}Pb methodology for dating marine sediments.

One complication that arises in the use of ^{210}Pb as a geochronometer is the presence of ^{210}Pb within the soil that is not derived from atmospheric fallout. This fraction of the ^{210}Pb is continuously produced within the sediment column from its parent radionuclide, ^{226}Ra, and is considered “supported” (Walker, 2005). This process occurs in secular equilibrium and is thus time-independent and unusable as a geochronometer. As such, the “unsupported” fraction of ^{210}Pb, produced in the atmosphere and then deposited and buried within the sediment (also known as excess ^{210}Pb, or $^{210}Pb_{ex}$), must be isolated from the supported fraction (Walker, 2005). This is typically achieved by the concurrent measurement of the activity of ^{226}Ra in the sample which provides an estimate of the production of supported ^{210}Pb: after initial subsampling the sealed container is left for three weeks to allow ^{222}Rn and its daughter nuclides to reach radioactive equilibrium and then the activity of one of the daughter nuclides, ^{214}Pb, is measured (Kirchner & Ehlers, 1998). Alternatively, if the core is of sufficient depth that all $^{210}Pb_{ex}$ has decayed (indicated by consistent down-core values), total ^{210}Pb values at the base of the core can be taken as the supported fraction, and subtracted from measurements of ^{210}Pb for the rest of the core.

There are three methods by which ^{210}Pb can be measured: alpha spectrometry (measurement of the ^{210}Po activity); beta spectrometry (measurement of ^{210}Bi activity); and gamma spectrometry (direct ^{210}Pb measurement based on the emission of a 46.5 keV gamma photon). Both alpha and beta spectrometry require destructive sampling methods; samples prepared for alpha are spiked with ^{209}Po and digested using perchloric acid and hydrofluoric acid (Zaborska et al., 2007), whilst beta analysis relies on liquid scintillation (Bonczyk, 2013). Gamma spectrometry, on the other hand, is non-destructive, in addition to providing simultaneous measurements of other gamma-emitting radioisotopes which can be used as an independent age validation, whilst being comparably accurate to the other techniques (Appleby et al., 1986; Zaborska et al., 2007).

1.3.2 Age-depth Model Construction

In an ideal sediment profile, deposited under stable conditions in which there is no variation in sediment accumulation rates or flux of ^{210}Pb to the sediment, an age-depth model would simply be the profile of ^{210}Pb concentration along the core as an exponential curve, described by the radiometric decay law (Sánchez-Cabeza & Ruiz-Fernández, 2012). In such settings one might apply the Constant Initial Concentration (CIC) model (Goldberg, 1963), which works under the hypothesis that $^{210}Pb_{ex}$ concentration contemporary to the formation of each sediment layer is constant (i.e., each sample originally contained the same concentration of $^{210}Pb_{ex}$, and any differences measured analytically are simply a function of radiometric decay, and thus time since deposition). This model can be described as:

$$t = \frac{1}{\lambda} \ln \frac{C_0}{C_i} \quad (1)$$

where t = age, λ = the ^{210}Pb decay constant of 0.03118 ± 0.00017 yr^{-1} (DDEP, 2022), and C_0 and C_i represent $^{210}Pb_{ex}$ concentration of the sediment at time of formation (assumed to be equal to present surface concentrations) and at the time of measurement, respectively, represented by the equations:

$$C\ (i, t = 0) = \frac{f(i)}{r(i)} \quad (2)$$

$$C(i) = C(i, t = 0)e^{-\lambda t} = \frac{f(i)}{r(i)}e^{-\lambda t} \quad (3)$$

with *f* and *r* representing the flux of $^{210}Pb_{ex}$ to the sediment and the mass accumulation rate for a particular section (i), which can itself be considered as:

$$r = \frac{dm}{dt} \quad (4)$$

with *m* representing the dry mass of a section.

Table 1.1 Nomenclature of formulae included in the text.

Nomenclature	**Interpretation**	**Unit**
t	Age of sediment	yr^{-1}
λ	^{210}Pb decay constant	yr^{-1}
C_0	$^{210}Pb_{ex}$ concentration at time of formation	Bq kg^{-1}
C_i	$^{210}Pb_{ex}$ concentration at time of measurement	Bq kg^{-1}
f	Flux of $^{210}Pb_{ex}$ to sediment	Bq m^{-2} yr^{-1}
r	Mass accumulation rate	kg m^{-2} yr^{-1}
m	Dry mass of a section	kg
k	Constant	
A(0)	Total cumulative inventory of $^{210}Pb_{ex}$	Bq m^{-2}
A(i)	Accumulated deposit of $^{210}Pb_{ex}$ below a particular sediment layer	Bq m^{-2}
S	Core cross section	m^2

However, more sophisticated models are necessitated by the complicated conditions that are found in the real world, with variable sedimentation rates

impacting the initial concentration of ^{210}Pb in the sediment. In ^{210}Pb-limited systems, if mass accumulation rate increases, and ^{210}Pb flux to the sediment remains the same, then the concentration of excess ^{210}Pb will be reduced (in effect being diluted by the extra sediment) (Sánchez-Cabeza & Ruiz-Fernández, 2012). Conversely, if mass accumulation rate decreases, concentration of excess ^{210}Pb is enriched. Thus, mass accumulation rate is inversely proportional to the concentration of excess ^{210}Pb found within the sediment. Given the variable rates of sediment production and low ^{210}Pb concentrations in Antarctic glacimarine environments, the CIC model is considered to be unsuitable for the purposes of this study.

The Constant Rate of Supply (CRS) model, on the other hand, operates under the hypothesis that, on the timescale that ^{210}Pb dating is concerned with (<200 years), there has been a constant atmospheric fallout of ^{210}Pb, and thus constant rate of supply of unsupported ^{210}Pb to the sediment. It makes no implicit assumption about mass accumulation rate or subsequent initial concentration of $^{210}Pb_{ex}$ (Appleby and Oldfield, 1978). This hypothesis can be described as:

$$f_i = f = k \tag{5}$$

where *k* is a constant (which will vary from site to site). Under such an assumption, the initial $^{210}Pb_{ex}$ for any sediment depth can be considered:

$$C(i, t = 0) = \frac{f}{r_i} \tag{6}$$

If we consider the dry mass of a section m, the *accumulated* deposit (*A*) can be obtained by integration:

$$A = \int_m^\infty C \, dm \tag{7}$$

Thus, the CRS model describes the age of a sediment layer as:

$$t_{(i)} = \frac{1}{\lambda} \ln \frac{A(0)}{A(i)} \tag{8}$$

where $A(0)$ represents the total cumulative inventory of $^{210}Pb_{ex}$ through the entire sediment depth and $A(i)$ represents the accumulated deposit of $^{210}Pb_{ex}$ below a particular sediment layer. When considering Eqs. (3) and (4), $A(0)$ can be considered as:

$$A(0) = f/\lambda \tag{9}$$

and $A(i)$ can be related to $A(0)$ by:

$$A(i) = A(0)e^{-\lambda t} \tag{10}$$

Thus, to determine age (t), the $^{210}Pb_{ex}$ inventory of the entire core must be determined. In some cases, where the core recovered spans a depth sufficient to reach the point at which all $^{210}Pb_{ex}$ is decayed (i.e., where $^{210}Pb_{total} = {}^{214}Pb$), this simply consists of determining the value at which this equilibrium is reached: the cumulative $^{210}Pb_{ex}$ value at that depth is $A(0)$. It should be noted however, that as radiometric decay is exponential, and analytical capabilities are limited, exact equilibrium will never be measured; instead at some point an arbitrary value must be considered as sufficient to represent equilibrium (typically 5% of surface $^{210}Pb_{ex}$). However, in many cases insufficient core length is recovered, and equilibrium depth is not reached, complicating determination of $A(0)$. In such circumstances, the missing $^{210}Pb_{ex}$ inventory can be determined in two ways:

a. The use of a reference date

This solution is possible if we can determine the age of a particular layer by other means. Age can then be used to solve for the cumulative inventory below this layer (j), in combination with the measured (incomplete) inventory of $^{210}Pb_{ex}$ (δA):

$$A(\mathrm{j}) = \frac{\delta A}{e^{\lambda t} - 1} \tag{11}$$

This can then be used to solve for total core inventory:

$$A(0) = \delta A + A(j) \quad (12)$$

b. Extrapolation

If the age of a particular layer cannot be determined by other means, equilibrium depth and $A(0)$ must instead be calculated by exponential regression analysis of the slope of the region of radiometric decay of $^{210}Pb_{ex}$. This is only suitable where the activity vs depth profile does not significantly deviate from an exponential relation in the lower part of the core.

The simplest way to then estimate mass accumulation rate for a given layer (r_i) is through the expression:

$$r_i = \frac{\Delta m_i}{S \Delta t_i} \quad (13)$$

where m_i is the mass of a section, t_i is the age of a section, and S is the core cross section. However, due to the non-independence of age, significant uncertainties are associated with the resulting mass accumulation rates (Sánchez-Cabeza et al., 2014). A better strategy is to incorporate the relationship between flux of ^{210}Pb, initial $^{210}Pb_{ex}$ concentration and mass accumulation rates described in eq. 3, such that:

$$r(i) = \frac{\lambda A_{b(i)}}{C(i)} \quad (14)$$

where A_b represents the cumulative inventory below the section. For further details on the specifics of ^{210}Pb modelling and the above equations the reader is directed to Appleby (2001) and Sánchez-Cabeza & Ruiz-Fernández (2012).

1.3.3 Independent Validation

Although these models provide a good estimation of age, independent validation should be sought to both verify and iteratively improve them (Sánchez-Cabeza & Ruiz-Fernández, 2012; Smith, 2001). The most commonly used technique for establishing age verification of ^{210}Pb models is the use of the global fallout radionuclides ^{137}Cs, $^{239+240}Pu$ and/or ^{241}Am (Huh & Su, 1999). These isotopes

were anthropogenically enriched by mid-20th century nuclear bomb testing, reaching a maximum in 1963 prior to the international Partial Test Ban Treaty, producing a signal which can be readily identified (Pennington et al., 1973). Furthermore, from an analytical perspective this requires relatively few additional resources as analysis is undertaken using the same gamma spectrometry techniques as ^{210}Pb analysis, simply adjusting for the alternate KeV lines. However, these techniques are not always possible as global fallout radionuclides are not always present in sufficient concentrations to be detectable (e.g. Masqué et al., 2002).

Numerous alternative methodologies have been used to provide an independent age validation. In sediments with a significant biogenic component the ^{14}C radiocarbon bomb pulse can be used, operating on the same principle of identifying a signal from the 1963 nuclear bomb testing maxima (Scourse et al., 2012). Natural events can be similarly used as a reference date, provided they are well documented. Volcanic eruptions, for example, result in the deposition of tephra, whilst earthquakes, floods, and tsunamis produce identifiable sedimentary sequences (Sabatier et al., 2022). On a local scale, changes in vegetation encoded in the pollen assemblage (Clark and Patterson, 1984), and changes in pollutant levels (Ruiz-Fernández et al., 2009) can potentially be traced back to documented events such as changes in land-use or industry. These are just a small subset of the potential techniques that can be used to independently validate ^{210}Pb chronologies, and each site will have different possible methodologies depending on the sedimentary features resulting from documented events and the analytical capabilities available.

1.3.4 Limitations of ^{210}Pb Dating

Several limitations apply to ^{210}Pb dating, arising from both analytical uncertainties and misapplication of theoretical models describing the relationship between ^{210}Pb activity profiles and age. All methods of measuring ^{210}Pb (and other radionuclides) have a limit of detection, arising from counting statistics and background radiation (MacKenzie et al., 2011). Typically, alpha counting has the lowest limit of detection (<1 Bq kg^{-1}), followed by well-type gamma detectors (<10 Bq kg^{-1}), with planar type gamma detectors falling somewhere between the two,

provided sufficient sample mass is available (Kirchner, 2011; MacKenzie et al., 2011).

As ^{210}Pb activity decreases exponentially (i.e., becomes infinitesimally small) the measured total $^{210}Pb_{ex}$ inventory of a core ($A(0)$), and the accumulated ^{210}Pb inventory below a specific layer (A_i) will always be under-estimations of the true values, as $^{210}Pb_{ex}$ activity below the limit of detection will be missed. Such an underestimation of $A(0)$, will lead to a fixed, small overestimation of age throughout the entire core. More problematically, the percentage underestimation of A_i will increase systematically with depth, resulting in an artificial overestimation of age that increases non-linearly with depth (MacKenzie et al., 2011). Generally, ages older than 100-130 years should be treated with caution (Barsanti et al., 2020; Binford, 1990). In addition, the uncertainties associated with ages will also increase with depth. Due to the logarithmic nature of ^{210}Pb distribution within the sediment column, and the random nature of radioactive decay, measured ^{210}Pb decreases with depth in the sediment column, such that measurement and other errors increase relative to the measured values (Binford, 1990). This problem is exacerbated at sites with low ^{210}Pb flux and high sedimentation rates which act to dilute ^{210}Pb activity.

The age at which this ‘dating horizon’ is reached will vary depending on the specific detection limit of the detector used, and the mass and activity concentration of the sample. The estimation of $A(0)$ and A_i are further complicated in instances where equilibrium depth is not reached, as discussed in the previous section. However, even where it can be considered that equilibrium depth has been reached in a core, the determination of the specific level at which equilibrium depth occurs is complicated by these analytical uncertainties, potentially introducing further error into the resulting age-depth model (Schirone et al., 2022).

In addition to analytical errors, an incomplete understanding of the processes that govern ^{210}Pb distribution within a sediment profile can lead to the misapplication of the theoretical models described above. Unlike analytical errors, these uncertainties cannot be quantified, though can be significant (Smith, 2001). Numerous processes can act to violate the assumptions of the various ^{210}Pb

dating models; notably, diffusion and bioturbation resulting in post-depositional mobility of ^{210}Pb, grain size effects, remobilisation of sediments, loss of surface material during sampling, and erosional processes (Kirchner, 2011; Robbins & Herche, 1993). For some of these problems the effects can be minimised by additional descriptive models. The addition of a mixing model, for example, is sometimes used to correct for bioturbation and physical mixing (e.g. Masqué et al., 2002), though these require independent measurements of the depth of the zone of mixing, and should be used with caution as even a small (~1cm) error in this estimate can result in dating errors as high as 20-30% (Binford, 1990), whilst the effect of ignoring minor mixing (<15% of the depth of the total $^{210}Pb_{ex}$ profile) is negligible (Binford, 1990; Appleby & Oldfield, 1992). Other complications, such as grain size effects, can be reduced by sampling procedures (e.g., sieving prior to analysis). Some processes, however, are particularly difficult to quantify (e.g., loss of surface sediment during sampling or via erosive processes), but can result in substantial error (e.g. Farmer et al., 2006; Olid et al., 2008).

Chapter 2: Study Area

2.1 The Antarctic Peninsula

The Antarctic Peninsula (AP) is a long, narrow, and heavily glaciated mountain-spine extending northwards from the main Antarctic continent. The eastern side of the peninsula is colder, with extensive ice shelves, whilst the western side is warmer and wetter with numerous marine-terminating glaciers (Cook et al., 2016). Climate on the AP is dominated by the circumpolar westerly winds. The region experienced rapid atmospheric warming (0.5˚C per decade) over the latter half of the 20th century (Turner et al., 2014), attributed to variations in the Southern Annular Mode, resulting in a poleward shift of these westerlies in the Indian Ocean sector and leading to a greater flow of mild air over the AP (Favier et al., 2017). At the turn of the century there was a marked hiatus in warming followed by a period of cooling, likely linked to the occurrence of stronger El Niño events (Oliva et al., 2017).

These westerly winds drive the flow of surface water in the Southern Ocean, propagating the eastward flowing Antarctic Circumpolar Current (ACC). Hydrographic conditions around the AP are in turn driven by interactions between the ACC, atmospheric temperatures, bathymetry and cryospheric processes. The western coast of the AP can generally be divided into two regions of distinct hydrographical regime: the Bransfield Strait and the central WAP. The Bransfield Strait is a deep (>2000m) basin running parallel to the coast of the AP, bounded to the northwest by the South Shetland Islands (Gordon et al., 1978). The central WAP shelf, on the other hand, is typically much shallower (~400m), with a number of sloped troughs that deepen towards the coast (Moffat & Meredith, 2018). These troughs allow for the intrusion of relatively warm and saline waters onto the shelf, sourced from mid-depths (~200m) of the ACC, termed Circumpolar Deep Waters (CDW). Whilst CDW is present in the Bransfield Strait, waters here are dominated by contributions of colder fresh water produced in the Weddell Sea (WSW) by seasonal sea-ice melting (Moffat & Meredith, 2018).

In recent decades, warming and shoaling of the CDW within the ACC has resulted in increased temperatures in both deep and surface waters on the central WAP (Schmidtko et al., 2014; Meredith & King, 2005), whilst the Bransfield Strait region has experienced weak to negative temperature trends over the same time period (Moffat & Meredith, 2018). Observed spatial patterns in glacier front retreat, notably a southerly increase and acceleration of retreat, have been used to infer that oceanographic regime, rather than air temperatures (and surface ablation), are the most important control on glacier stability in the region, due to basal melting of ice-shelves and tidewater glaciers by intruding mid-depth ocean waters (Cook et al., 2016).

Three sites were selected across the AP (Figure 2.1): Marian Cove, Börgen Bay, and Ryder Bay, encompassing a variety of fjord geometries, bathymetries, glacial retreat histories, oceanographic regimes, and climates. Seven coring locations were chosen in total, forming both a latitudinal transect between the fjords, and transects within fjords, to provide representative coverage of Antarctic fjord environments and to allow for an understanding of the differences between different fjord systems, and the variability that exists within individual fjords.

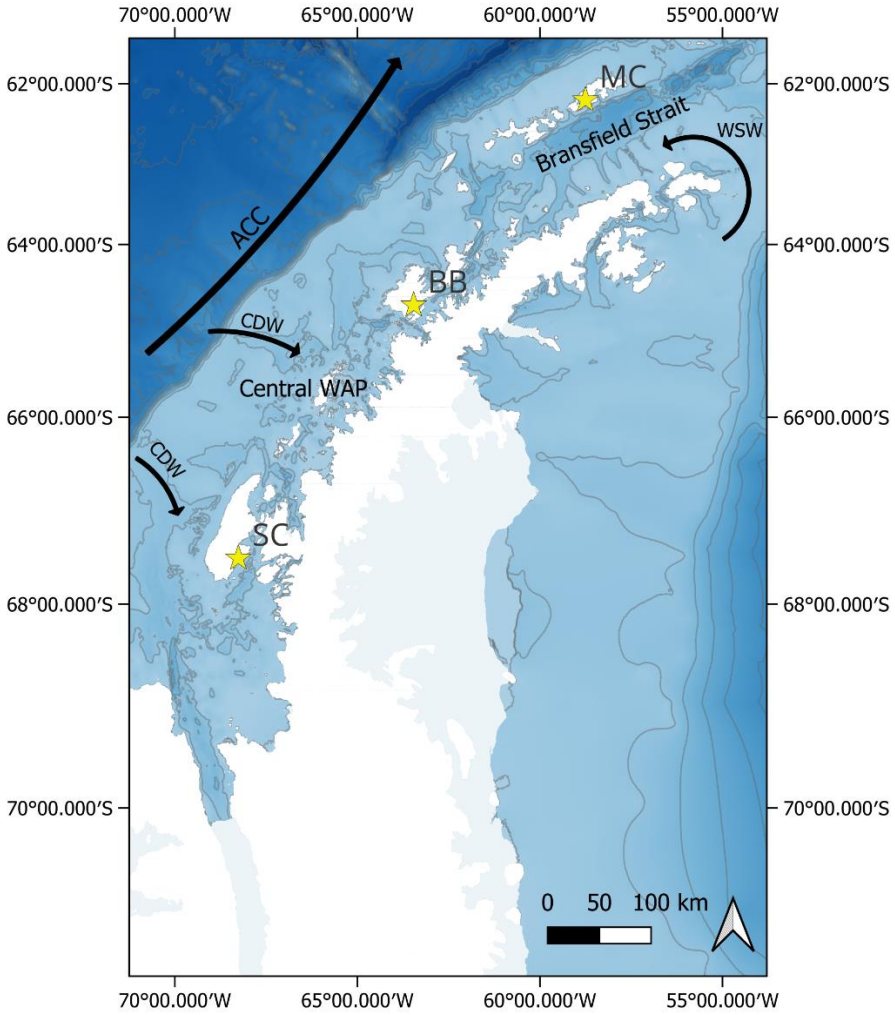

Figure 2.1. Overview of the AP. Stars indicate the three study sites: Marian Cove, Börgen Bay, and Ryder Bay (north to south). Contour lines are at 500m intervals and arrows indicate general circulation patterns of the ACC, CDW and WSW, as described in Moffat and Meredith, 2018. Bathymetric data were sourced from GEBCO (2022).

2.2 Marian Cove

Marian Cove (Figure 2.2), situated within Maxwell Bay on King George Island (South Shetland Islands), is the most northerly study site. Four major tidewater glaciers discharge into Maxwell Bay, with a total ice catchment area of 92 km^2, with the glacier at the head of Marian Cove contributing a catchment area of 15 km^2 (Munoz & Wellner, 2018). Contemporary mean surface air temperatures in Maxwell Bay, recorded at Bellinghausen Meteorological Station, are around -2˚c, varying from +1.6˚c in the summer to -6.9˚c in winter. A positive trend in mean

annual temperatures has been observed at Maxwell Bay from the period 1969-2001, followed by a reduced rate of warming between 2001-2019. Sea ice is typically present between July and October (Yoon et al., 1997). A relatively simple circulation pattern exists within Maxwell Bay, with a west to east circulation influenced by Coriolis deflection. Although the tributary fjords are too narrow for direct interference by the Coriolis effect, the general circulation patterns of Maxwell Bay are propagated into the fjords such that they exhibit the same pattern (Yoo et al., 2015).

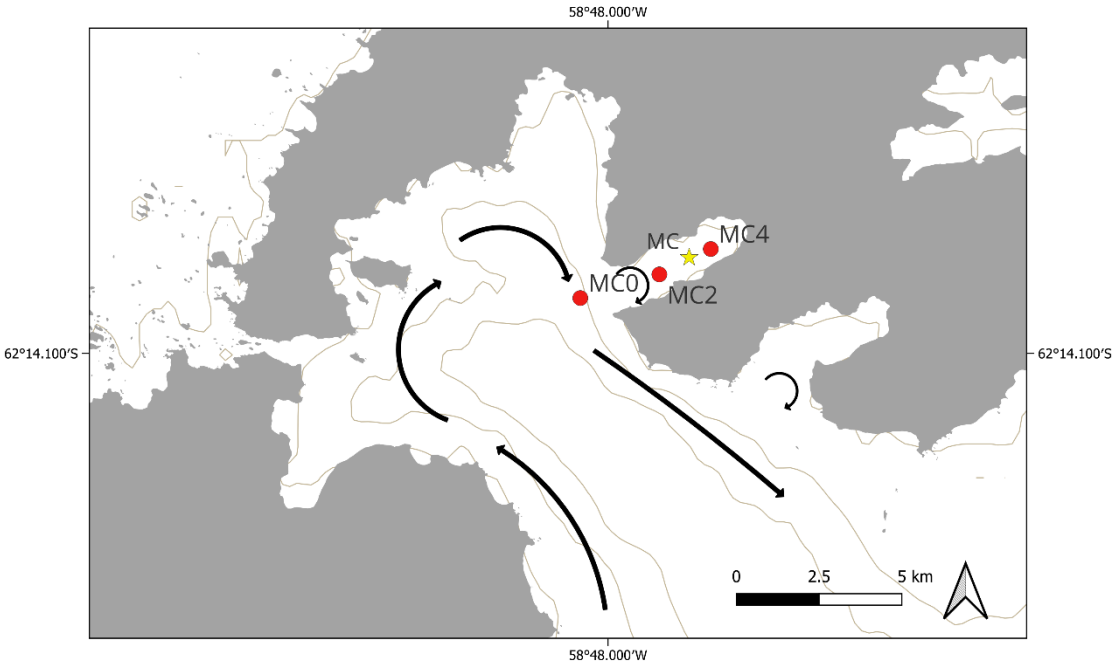

Figure 2.2. Overview of Maxwell Bay. Red circles indicate coring locations of the present study, yellow triangles represent coring locations of previous studies, and black arrows indicate general ocean currents as shown in Monien et al. (2011). Contours at 200m intervals were generated from bathymetric data sourced from GEBCO (2022).

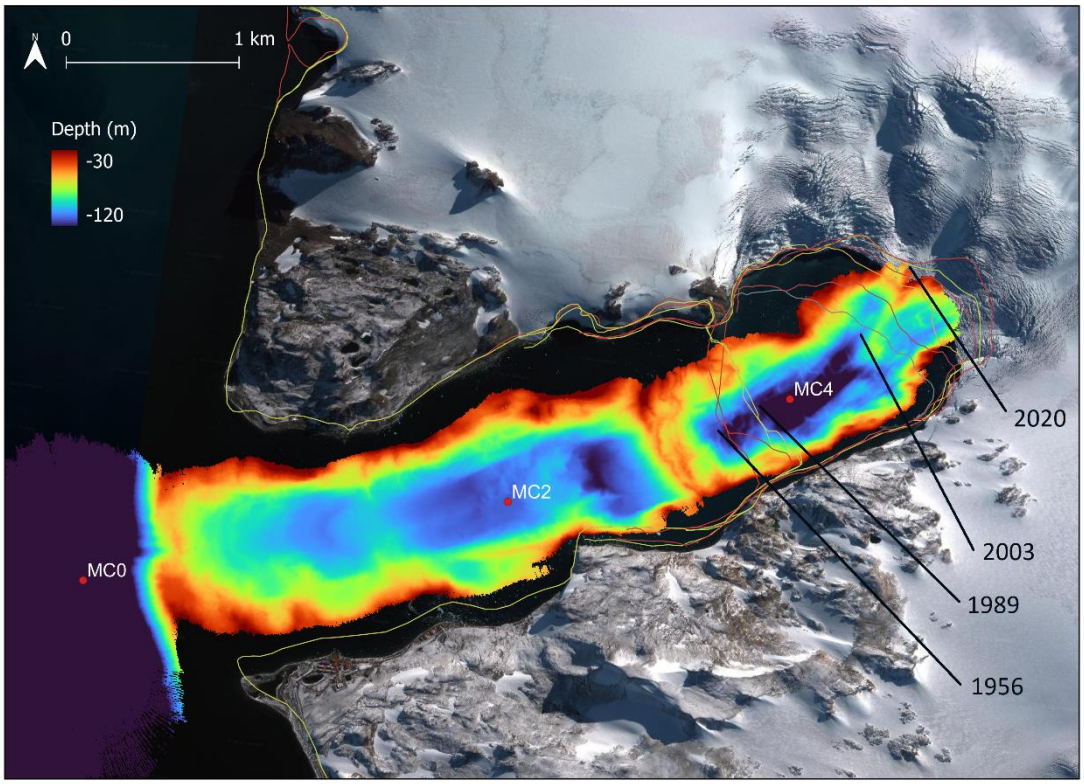

Figure 2.3. Bathymetry (Retallick et al., 2021) and satellite-derived ice front positions (Cook et al., 2014) of Marian Cove.

Marian Cove has a simple linear geometry, with a high length to width ratio and a tidewater glacier at the head, eroded into a bedrock consisting of volcaniclastic sediments intruded by Eocene granodiorite (Hur et al., 2001). In addition, various valley glaciers terminate on land on the northern cliffs of Marian Cove, with meltwater subsequently entering the cove via fluvial processes (Yoon et al., 1998). The cove is separated from Maxwell Bay by an entrance sill, approximately 70m in water depth, and contains two deep basins (max depth ~120m), which are also separated by a prominent sill feature (Figure 2.3). In the ice proximal zone, four distinct water masses are present: a surface layer of cold and turbid meltwater; a relatively warm inflow layer characteristic of general Maxwell Bay waters; a turbid and cold mid-depth layer of subglacial origin; and a deep layer comprised of remnant winter water (Yoo et al., 2015). Mixing between the waters of Maxwell Bay and Marian Cove is promoted by tidal forcing over the entrance sill. There has been no evidence of down-slope turbidity currents (Yoo et al., 1999, 2000).

Satellite data of ice front positions indicate that the tidewater glacier in Marian Cove has retreated by around 1.7 km since records began in 1956 (Figure 2.3). The glacier front position was relatively stable from 1956-1989, situated in shallow waters and in a narrowing of the fjord geometry. Several small re-advancements of the glacier front occurred during this time, notably in 1973, and between 1986-1989. At some point between 1989 and 2003 the frontal position then began to retreat across the deep, open water of the inner basin; retreat has continued until the present day.

Previous work on sediment cores from Maxwell Bay have found sediment mass accumulation rates (MARs) varying between 0.1-0.81 g cm^{-2} y^{-1} (Figure 2.2, Table 2.1). Direct comparison between results reported in different studies is difficult owing to varying methodologies – Boldt et al., 2013, for example, used alpha counting (α) to determine $^{210}Pb_{ex}$ and calculated MARs from linear regression of the logarithmic profile and dry bulk density, whilst Monien et al. (2011, 2017) determined $^{210}Pb_{ex}$ activity from gamma spectrometry (γ), and MARs from the CRS model. Several of these studies, however, reported on sediment accumulation rates from multiple cores, and general spatial patterns may be deduced. In Boldt et al. (2013) the highest MARs are found in core KC21, proximal to the ice front in Marian Cove (0.34-0.81 g cm^{-2} yr^{-1}), which drops by around half (0.11-0.44 g cm^{-2} yr^{-1}) in core KC22 in the central basin of the cove. Similar rates are found in KC14 and KC23 (0.14-0.39; 0.18-0.21 g cm^{-2} yr^{-1}) at the mouths of Collins Harbour and Potter Cove, respectively. At all sites a general increase in sedimentation rate over time is observed. In Potter Cove, Monien et al. (2017) found generally consistent rates, regardless of distance from the ice front, increasing from around 0.1-0.4 g cm^{-2} yr^{-1} over time. Monien et al. (2011) found relatively high MARs (0.2-0.66 g cm^{-2} yr^{-1}) in the main basin of Maxwell Bay, also increasing over time, with the periods of greatest acceleration in MAR occurring in the periods 1940-1980 and 1995-2005. Mean surface $^{210}Pb_{ex}$ concentrations, where reported, range from 92-94 Bq kg^{-1} within Potter Cove (Monien et al., 2017) to 239 Bq kg^{-1} in the main basin of Maxwell Bay (Monien et al., 2011).

Table 2.1. Previously reported sedimentation rates for Maxwell Bay. Where a change in MAR is reported both values are given. Core locations are shown in Figure 2.2.

Core	Study	Technique	MAR ($g\ cm^{-2}\ yr^{-1}$)	Surface $^{210}Pb_{ex}$ ($Bq\ kg^{-1}$)	^{137}Cs ($Bq\ kg^{-1}$)
KC21	Boldt et al. (2013)	α	0.34-0.81	-	-
KC22	Boldt et al. (2013)	α	0.11-0.44	-	-
KC14	Boldt et al. 2013	α	0.14-0.39	-	-
KC23	Boldt et al., 2013	α	0.18-0.21	-	-
PS 69/335-1	Monien et al., 2011	γ	0.2-0.66	239	Not detected
K44	Monien et al., 2017	γ	0.18	92	Not detected
P03	Monien et al., 2017	γ	0.10-0.40	94	Not detected
P09	Monien et al., 2017	γ	0.15-0.49	94	Not detected

In addition to sediment cores Monien et al. (2017) also report suspended particle matter (SPM) concentrations in water masses and accumulation in sediment traps in Potter Cove. They identified spatial patterns in SPM, with the south-western region of the cove experiencing the lowest water turbidity and accumulation in traps, and the eastern inner-region showing the highest turbidity and accumulation. These patterns are associated with the general circulation patterns in Potter Cove, with clear water flowing into the cove from Maxwell Bay, mixing with the very turbid water at the glacier front, and then flowing out of the bay along the south-eastern flank. High turbidity and accumulation in traps were also found in-front of the meltwater streams in ice-free areas along the cliffs near

the mouth of Potter Cove. A comparison between SPM in the traps Potter Cove in the upper water column (5m) and the lower water column (20m) suggests that up to 50% of SPM remains within the surface overflow and is exported out of the inner cove.

Yoon et al. (1998) found similar spatial patterns of sedimentation in Marian Cove, with the highest SPM concentrations occurring at the mouth and northern edge of the fjord, where glaciers commonly terminate on land, developing numerous meltwater streams. SPM concentrations in the surface water in Marian Cove were much higher than those in Maxwell Bay, and showed distinct spatial patterns, with peak SPM gradually decreasing southeast-wards, suggesting that Marian Cove is likely the most important sediment source within Maxwell Bay (Yoon et al., 1998). Within the water column of Marian Cove SPM decreases with depth, except for a pronounced turbid mid-depth layer (cold tongue) found only in the inner basin (Yoo et al., 2015). Significantly different morphological features of sediments within these two layers (surface and mid-depth) suggest that the suspended sediments in the mid-depth layer were transported by a horizontal buoyant plume, originating at depth from the marine-terminating ice front, as opposed to vertical settling of the supraglacial meltwater plume (Yoo et al., 2015)

2.3 Börgen Bay

Börgen Bay (Figure 2.4) is a 40 km^2 fjordic embayment on the southern coast of Anvers Island (Palmer Archipelago). It is divided into a wider but shallower sector to the west, and a narrower and deeper sector to the north, with tidewater glaciers present at the head of both sectors. Entrance sills at a depth of around 120m are present for both sectors, and in the northern sector water depths rapidly increase to over 300m in a bathymetric basin behind the sill (Figure 2.5). The mouth of the bay opens out to the Neumayer Channel and Wiencke Island to the south, beyond which lies the intersection of the Gerlache and Bismarck Straits. Unlike Marian Cove, Börgen Bay is relatively understudied, and as such its hydrographic regime and sedimentation rates are relatively unknown, though intrusions of CDW have been observed (K. Sheen*, pers. comms*).

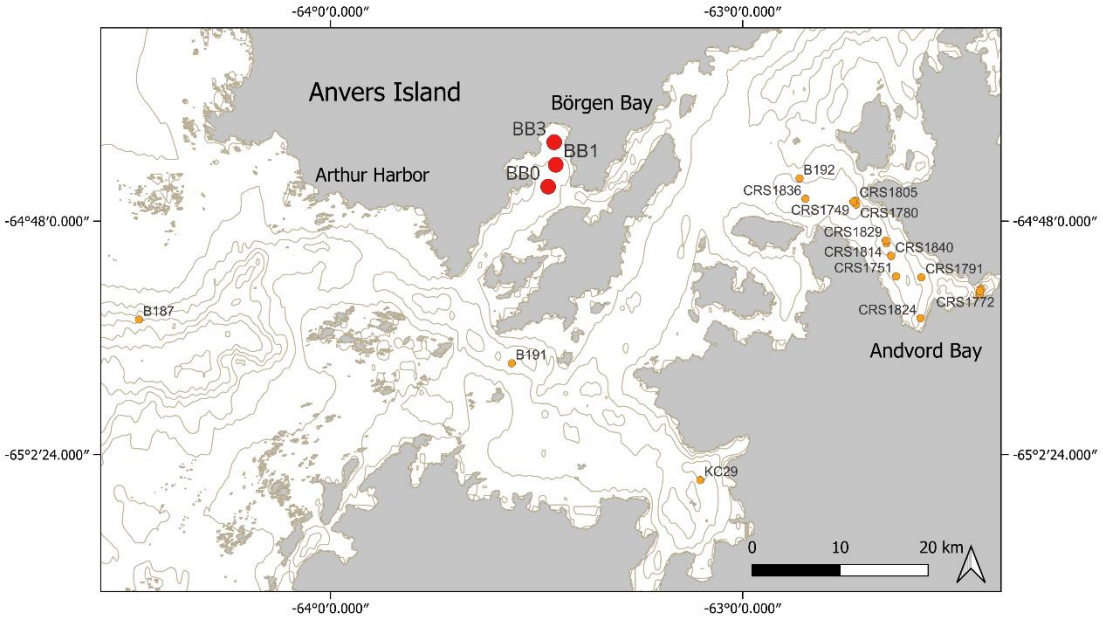

Figure 2.4. Overview of Börgen Bay and surrounding region. Red circles indicate coring locations of the present study and yellow triangles represent coring locations of studies reported in Table 2.2. Contours at 200m intervals were generated from bathymetric data sourced from GEBCO (2022).

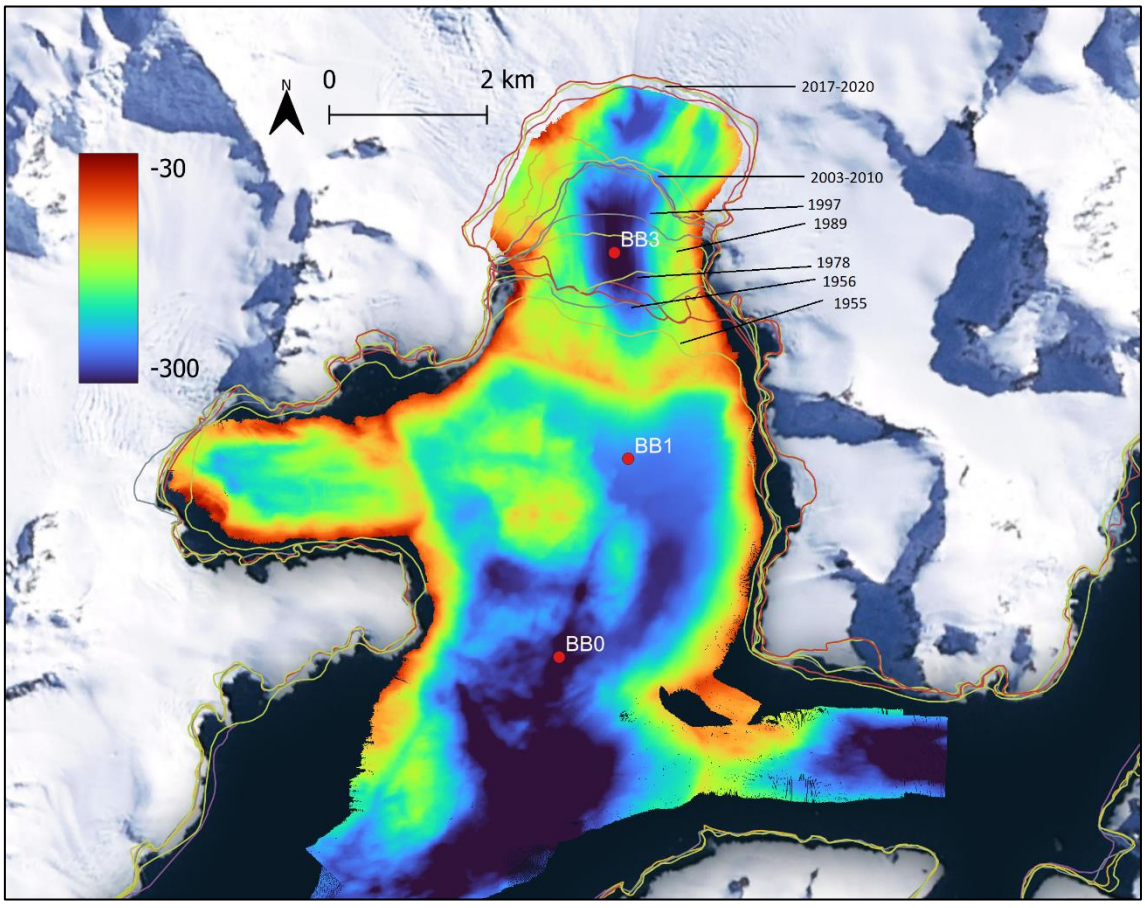

Figure 2.5. Bathymetry (Retallick et al., 2021) and satellite-derived ice front positions (Cook et al., 2014) of Börgen Bay.

The closest meteorological station to Börgen Bay, at Vernadsky/Faraday Research Base, recorded the greatest increase in temperatures of all Antarctic Peninsula meteorological stations over the 20th century (Turner et al., 2005), with a warming trend of 0.32˚C/decade in 1979-1997, though more recently has recorded a shift to a cooling trend of -0.47˚C/decade from 1999-2014 (Turner et al., 2016). The hydrography of the nearby Gerlache Strait represents a gradient between the two distinct deep-water regimes of the central WAP shelf to the south, dominated by warmer upper CDW, and the relatively cooler waters of the Bransfield Strait to the north (Lundesgaard et al., 2020).

Satellite data for Börgen Bay (Figure 2.5) indicate that similar to Marian Cove, glacier retreat has occurred in step-wise fashion. The first available satellite data (1955) indicates an ice front position close to the bathymetric sill at the mouth of the northern sector of the bay. By 1956 the ice-front appears to have retreated by 0.4 km, to a position where it remained relatively stable until 1978, possibly due to the narrow geometry of the fjord at this location. Sometime after 1978 the ice-front rapidly retreated another 0.8km to its 1989 position, followed by another period of relative stability until 1997. Further retreat, of around 0.5 km, then occurred between 1997 and 2003, followed by a stable front position until 2010, and then subsequent rapid retreat (of around 1 km) to its current position.

Previously reported sedimentation rates for the surrounding region (Table 2.2) range from 0.06 g cm^{-2} yr^{-1} (open waters in the Gerlache and Bismarck Straits) (Isla et al., 2002) to 0.56 g cm^{-2} yr^{-1} in Andvord Bay (Eidam et al., 2019). There have been no previous studies on sedimentation rates within Börgen Bay or the Neumayer Channel.

Table 2.2. Previously reported sedimentation rates for sites close to Börgen Bay. Core locations are shown in Figure 2.4.

Core	Study	Technique	MAR ($g\ cm^{-2}\ yr^{-1}$)	Surface $^{210}Pb_{ex}$ ($Bq\ kg^{-1}$)	^{137}Cs ($Bq\ kg^{-1}$)
B187	Isla et al., 2002	α	0.064	1000	-
B191	Isla et al., 2002	α	0.093	500	-
B192	Isla et al., 2002	α	0.063	250	-
CRS1771	Eidam et al., 2019	α	0.38	-	Not detected
CRS1772	Eidam et al., 2019	α	0.45	-	Not detected
CRS1824	Eidam et al., 2019	α	0.29	-	Not detected
CRS1791	Eidam et al., 2019	α	0.56	-	Not detected
CRS1751	Eidam et al., 2019	α	0.5	-	Not detected
CRS1840	Eidam et al., 2019	α	0.24	-	Not detected
CRS1814	Eidam et al., 2019	α	0.44	-	Not detected
CRS1829	Eidam et al., 2019	α	0.2	-	Not detected
CRS1780	Eidam et al., 2019	α	0.23	-	Not detected
CRS1805	Eidam et al., 2019	α	0.23	-	Not detected
CRS1749	Eidam et al., 2019	α	0.15	-	Not detected
CRS1836	Eidam et al., 2019	α	0.37	-	Not detected
KC29	Boldt et al., 2013	α	0.27	-	-
KC57	Boldt et al., 2013	α	0.44	-	-

2.4 Ryder Bay

Ryder Bay (Figure 2.6) is a shallow and wide coastal embayment on the south-eastern edge of Adelaide Island, in the northern part of Marguerite Bay. There

are no significant transverse ridges in Ryder Bay, though bathymetry is nonetheless complex (Figure 2.7), with several raised sections and a notable deep basin (>500 m) landward of the sampling site. The bedrock of Ryder Bay is primarily comprised of granodiorite (Brimhall et al., 1988).

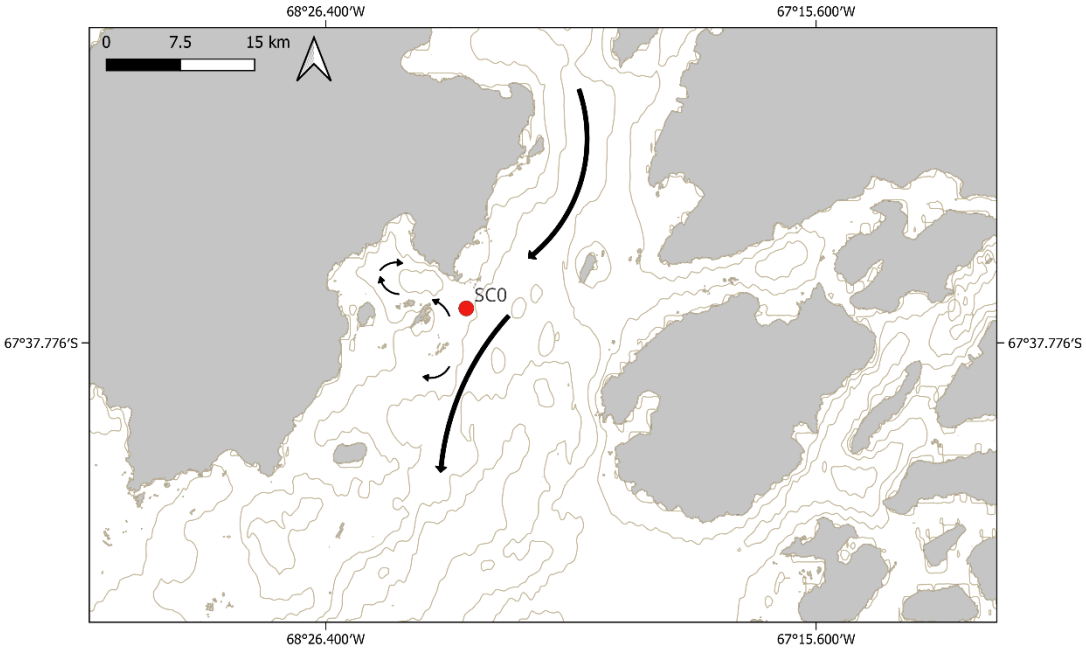

Figure 2.6. Overview of Ryder Bay and surrounding region. Red dot represents coring location, and black arrows indicate general circulation patterns after Webb et al. (2020). Contours at 200m intervals were generated from bathymetric data sourced from GEBCO (2022).

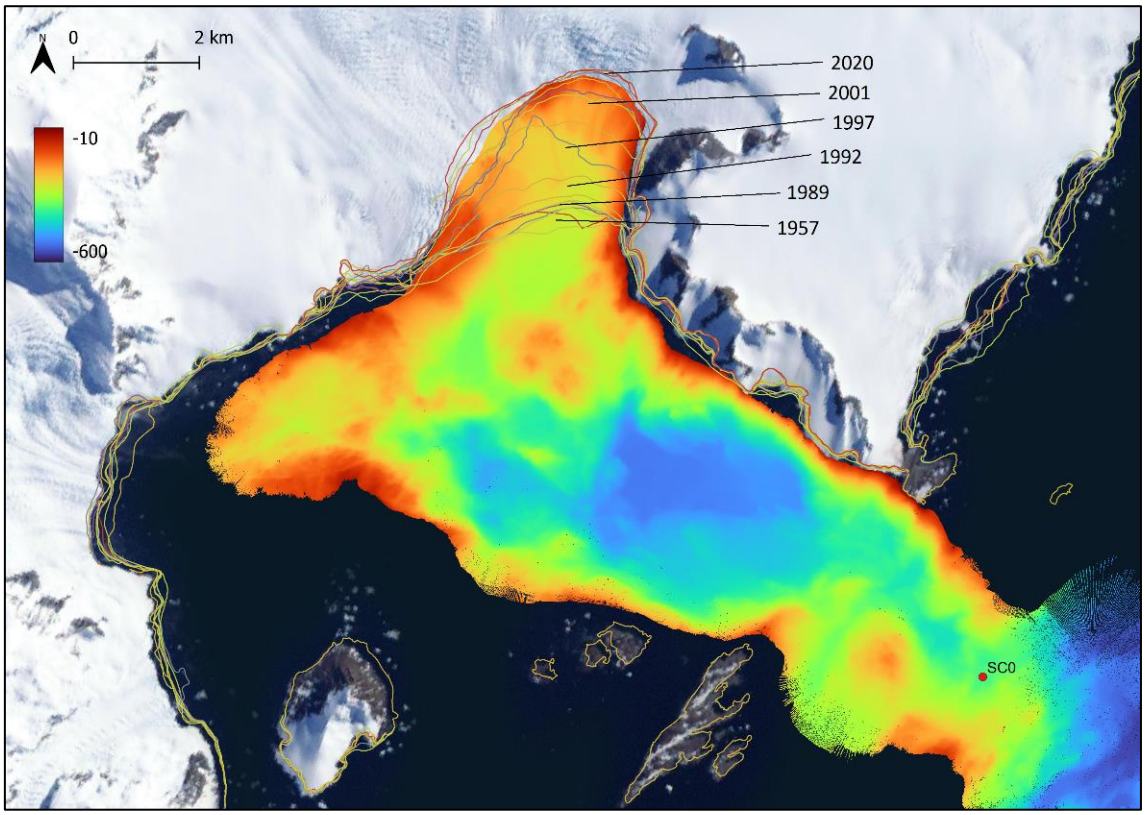

Figure 2.7. Bathymetry (Retallick et al., 2021) and satellite-derived ice front positions (Cook et al., 2014) of Ryder Bay.

The hydrography of Marguerite Bay is heavily influenced by upper CDW, which funnels into the bay via Marguerite Trough, a bathymetric low, and mixes with overlying cold and fresh Antarctic Surface Water (AASW) to form modified upper CDW which floods the shelf (Clarke et al., 2008). The open geometry of Ryder Bay allows for water to be readily exchanged with Marguerite Bay, with a general circulation pattern consisting of water entering to the south and flowing west past Lagoon Island and Sheldon Glacier before exiting the bay to the east, south of Rothera Point (Webb et al., 2020).

Atmospheric temperatures, recorded at nearby Rothera Research Station, have shown the same pattern as the rest of the AP, with a rise in temperatures up until the end of the 20th century followed by a cessation of warming, with a peak occurring at around 1990. The ice front of the glacier in nearby Sheldon Cove (Figure 2.7) was stable until around 1989, following which it rapidly retreated until 2003, where it remained relatively stable, slowly retreating to its current position.

Chapter 3: Methodology

3.1 ^{210}Pb Age-depth Models and Sediment Mass Accumulation Rates

The seven sediment cores used in this study were collected over two cruises on the *RRS James Clark Ross*. On the first cruise, JR18003, cores BB1, BB3, MC2, and MC4 were collected, whilst on the second cruise, JR19002, cores BB0, MC0 and SC0 were collected. In both instances a BAS Oktopus 12-core multicorer, fitted with transparent core sleeves of 0.5m length and 9.4 cm diameter, was deployed to retrieve the sediment cores (Figure 3.1).

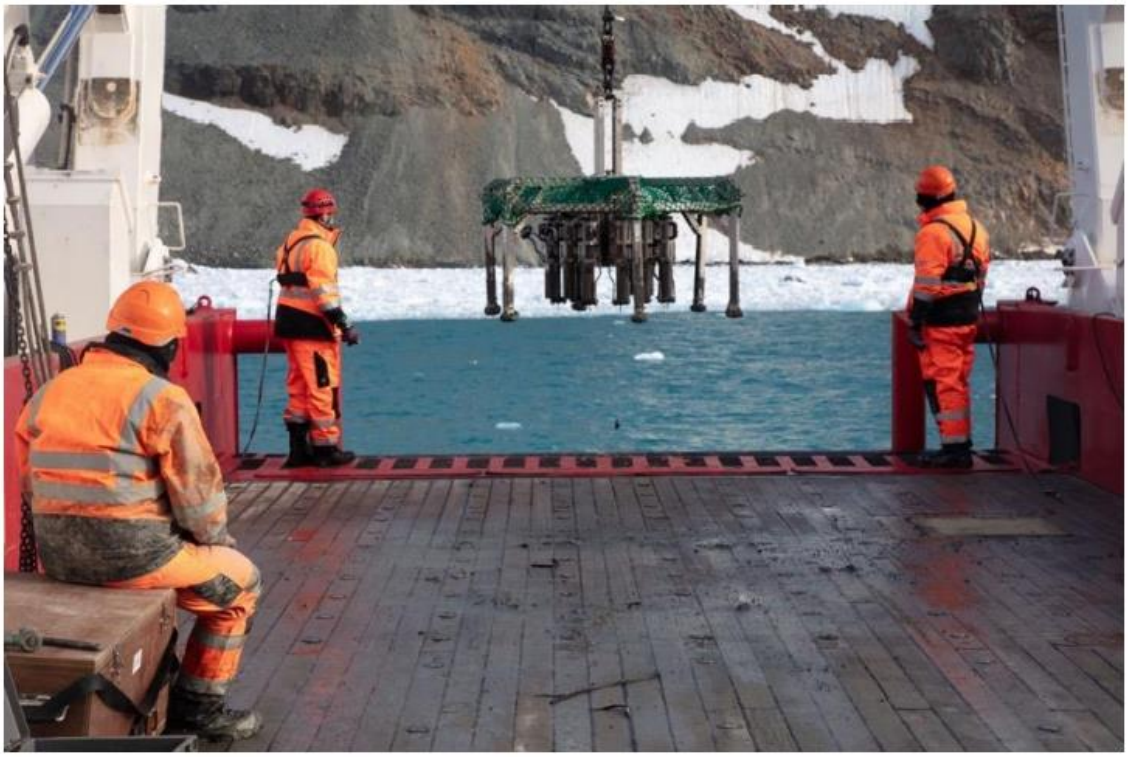

Figure 3.1. Photograph of multicore deployment (source: JR18003 Cruise Report, 2019).

The 12 cores collected were processed and subsampled onboard according to their intended analysis. The cores used for ^{210}Pb analysis in this study were collected according to sampling procedures for sedimentation rate (BB1, BB3, and MC2), organic carbon (MC4), and eDNA (BB0, MC0 and SC0). The onboard sub-sampling procedure for the upper two centimetres differed between these cores: for the eDNA and organic carbon cores, the cores were subsampled every

0.5cm down to 2cm depth, whilst the sedimentation rate cores were subsampled every other centimetre. Below 2cm depth the eDNA cores were subsampled every 1cm down to 4cm depth, and then every 2cm for the rest of the core, whilst the organic carbon cores were subsampled every 1cm down to 10cm depth, and then every 2cm to the bottom of the core. The sedimentation rate cores were sub-sampled every 1cm for the entirety of the core. The subsampling strategies for the different cores are outlined in Figure 3.2. Sediment slices were then placed in aluminium foil-lined petri dishes and stored in a freezer at -80˚C. Samples were procured for the present study in August 2021.

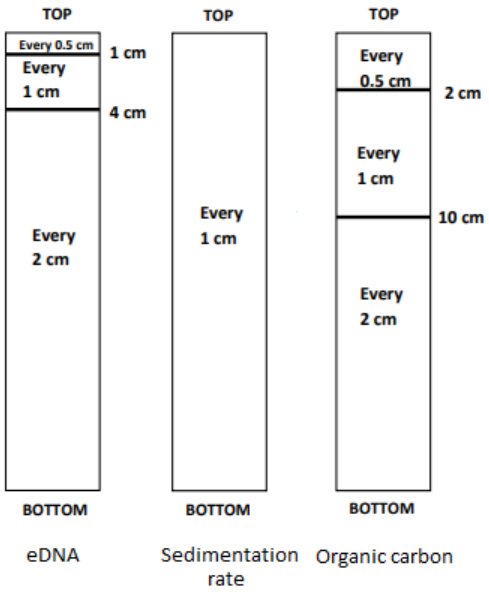

Figure 3.2. Multicore subsampling strategies.

The sediment slices in the petri dishes were transferred to glass vials and weighed, freeze-dried for 48hrs, and then re-weighed to determine water content. For the eDNA cores (BB0, MC0 and SC0), dry samples were then gently disaggregated with pestle and mortar and passed through a 2 mm sieve to remove the gravel fraction. The sediment was then placed in a standard aluminium container, weighed, and subsequently sealed using electrical tape and incubated for 21 days to restore radioactive equilibrium between ^{226}Ra and its daughter isotope ^{214}Pb. The samples were then sent to Dr Martha Hall at the Consolidated Radio-Isotope Facility (CoRIF) at the University of Plymouth for

analysis using an EG&G Ortec Planar detector system, calibrated to a known standard. Samples were counted for a minimum of 48 hours, and isotopes ^{210}Pb, ^{214}Pb, ^{241}Am, and ^{137}Cs were determined from gamma emissions at 46.5, 295.3, 59.5 and 661.6 KeV respectively.

Following successful determination of ^{210}Pb activity in the eDNA core subsamples, further subsamples from cores BB1, BB3, MC2 and MC4 were prepared for analysis. Dry samples were gently disaggregated and passed through a 0.5 mm sieve, packed into standard well-type radiometry vials, and then sealed using melted wax and left to incubate for 21 days. Samples were then sent to Dr Karen Leslie at the University of Exeter Geography Radiometry Laboratory, where samples were counted for 48 hours in a HPGe well-type detector, using the same KeV lines described above.

Dry bulk density of each sample was determined using water content, assuming water density of 1.026 g cm^{-3} (with a porewater salinity of 0.035 g g^{-1}) and inorganic sediment particle density of 2.65 g cm^{-3}. Organic matter was low across all cores (<1%), so no correction was necessary. The activity of ^{214}Pb was subtracted from total ^{210}Pb activity to determine ^{210}Pb$_{ex}$ activity concentrations, which were then plotted against cumulative dry mass, rather than depth, to avoid the shape of the profile being affected by variation in porosity along the core. First, the data were assessed to determine the validity of applying an age-depth model; all cores displayed a characteristic region of logarithmic decay, and thus were deemed suitable (Appleby et al., 2001).

The depth of the surface mixed layer (SML) was identified as the depth at which logarithmic decay begins, and the equilibrium depth was identified as the depth at which ^{210}Pb$_{ex}$ is at or close to zero. In order to apply the CRS model, the entire ^{210}Pb$_{ex}$ inventory of a given core must be known. Due to onboard sub-sampling methodologies this was unable to be measured, and thus it was necessary to interpolate missing values, as is standard in the literature (e.g., Barsanti et al., 2020). An exponential regression model of ^{210}Pb$_{ex}$ against cumulative mass depth within the region of radiometric decay was applied to each core, and values were interpolated from this model (or, if within the surface mixed layer, calculated as an average of the values above and below). Furthermore, in cores which failed

to penetrate to sufficient depth to reach equilibrium, this regression model was used to extrapolate $^{210}Pb_{ex}$ until equilibrium depth was reached. As radiometric decay is exponential, and all analytical measurements contain some degree of uncertainty, including background levels of radiation, measurement of $^{210}Pb_{ex}$ activity will never reach zero (MacKenzie et al., 2011), and thus an arbitrarily low value must instead be chosen – in this case, 5% of surface values (W. Blake, *pers. comms*). This was corroborated by non-depth dependant (irregular) variations in $^{210}Pb_{ex}$ activity below the interpreted equilibrium depth. The CRS model, described in detail in section 1.3.2, was then applied to the $^{210}Pb_{ex}$ data.

Uncertainties in the ^{210}Pb activity concentrations, derived from counting statistics and propagated by the quadratic propagation of uncertainty method, are presented to one standard error. Mass accumulation rates (MAR) for the region of radiometric decay were calculated following equation 14 of section 1.3.2. Extremely low $^{210}Pb_{ex}$ values were not included in calculation of mean MARs as they have significant associated uncertainties, nor were they included in the regression models used to interpolate and extrapolate missing $^{210}Pb_{ex}$ values.

Analytical errors were identified on the basis of ^{214}Pb activity measurements. ^{214}Pb is produced *in-situ* and is in equilibrium with the unsupported fraction of ^{210}Pb. As such, it should remain relatively consistent down-core, and should always remain lower than $^{210}Pb_{total}$. If either of these conditions are not met, a sample was considered erroneous; this was the case for one sample (BB3 8cm), and the value for this sample was instead interpolated.

3.2 Carbon Content

All laboratory analyses relating to the generation of data regarding carbon content (percent weight) of the sediment cores were conducted by Dr Alejandro Román-González; subsequent calculations and interpretations were conducted by the author. The cores analysed were collected from separate multi-core tubes from the same array (deployment) as those used for ^{210}Pb analysis, and thus while the age-depth models generated from the ^{210}Pb data should be representative, small differences in compaction during the coring process may result in minor age offsets.

The onboard subsampling process for the OC cores is outlined in Figure 3.2. The core slices that were then used for carbon analysis consisted of the entire upper 2cm (0.5, 1, 1.5, and 2cm), 5cm, 10cm, and 20cm depth, as well as the lowest recovered sample. The sediment slices were transferred to glass vials and weighed, freeze-dried for 48hrs, and then re-weighed to determine water content. The dry sediment was then homogenised and ~20mg was transferred to standard elemental microanalysis d10-12 tin capsules, and analysed using a Carbon Combustion Analyser at the University of Exeter Geography Radiometry Laboratory. Measurements prior to- and after acid digestion provided measurements of total carbon (TC) and total organic carbon (TOC); inorganic carbon (IC) was calculated as the difference between the two.

In total, 52 samples were analysed for TC, with 24 of these being analysed for TOC and replicated to determine measurement uncertainty. Upon data acquisition, average IC was calculated for each core and subtracted from TC for the 28 samples for which a direct TOC measurement was not available. IC was low and invariable down-core for all cores (0.091±0.07 %), and thus this approach was deemed suitable.

Chapter 4: Results

4.1 ^{210}Pb Age-Depth Models and Sediment Mass Accumulation Rates

All cores recovered for analysis had a length in the range of 20-30cm, with the exception of MC4 at 12cm, yielding 100 subsamples for analysis for radio-isotope activities in total. Surface ^{210}Pb activities ranged from 84±8 Bq kg^{-1} (MC4) to 379±26 Bq kg^{-1} (BB0), generally increasing away from the ice front within the individual fjords. A surface mixed layer was present in five of the seven cores, ranging in depth from 2 to 6 cm.

All cores exhibited a region of radiometric decay (Figure 4.1). In cores MC0, MC2, MC4, and BB1 ^{210}Pb$_{ex}$ concentrations exhibited a consistent rate of decrease throughout the entire region of decay (r^2 >0.7), whilst cores BB0, SC0 and BB3 exhibited a marked change in the rate of decrease. Equilibrium depth was not reached in cores MC0, MC4 and BB3, and thus ^{210}Pb$_{ex}$ concentration was extrapolated in order to determine *A*(0). For MC0 and BB3 a strong correlation (r^2 = 0.96 and 0.70, respectively) through a reasonable number of data points (n = 10 and 8) led to relatively high confidence in the extrapolated data. Due to the short length of MC4, however, only 4 data points were present within the region of radiometric decay, and as such despite a significant relationship (p<0.05) and strong correlation (r^2 = 0.96), the resulting age-depth model and MARs should be interpreted with caution.

No peaks in the fallout radionuclides ^{137}Cs and ^{241}Am were detected in any cores due to very low activity concentrations (and thus high relative uncertainties); this is consistent with observations reported in other studies on the AP and precludes independent validation of the age-depth models (e.g., Monien et al., 2011; Eidam et al., 2019). All isotope data used to construct age-depth models and calculate mass accumulation rates can be found in the appendix.

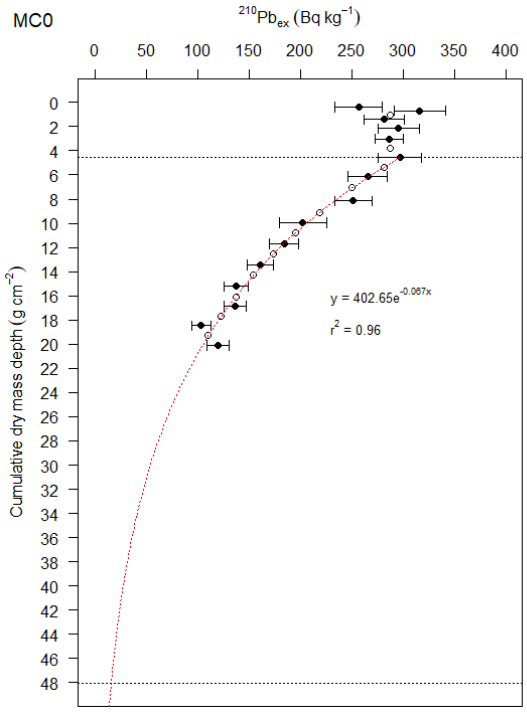
MC0
$^{210}Pb_{ex}$ (Bq kg^{-1})
Cumulative dry mass depth (g cm^{-2})
y = 402.65e$^{-0.067x}$
r^2 = 0.96

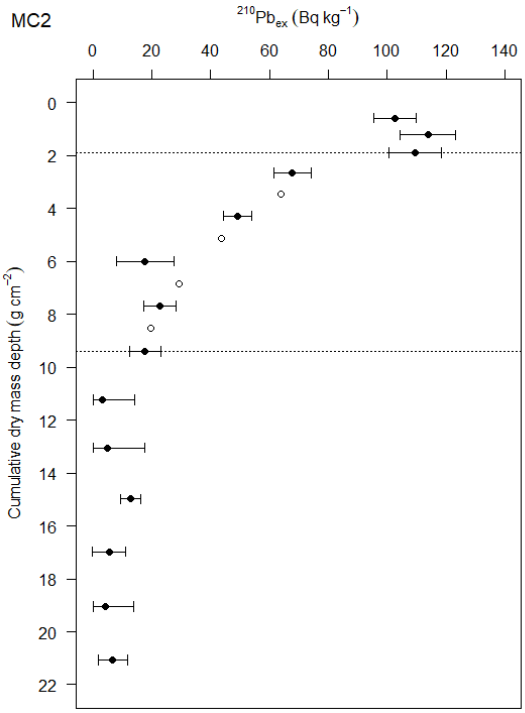
MC2
$^{210}Pb_{ex}$ (Bq kg^{-1})
Cumulative dry mass depth (g cm^{-2})

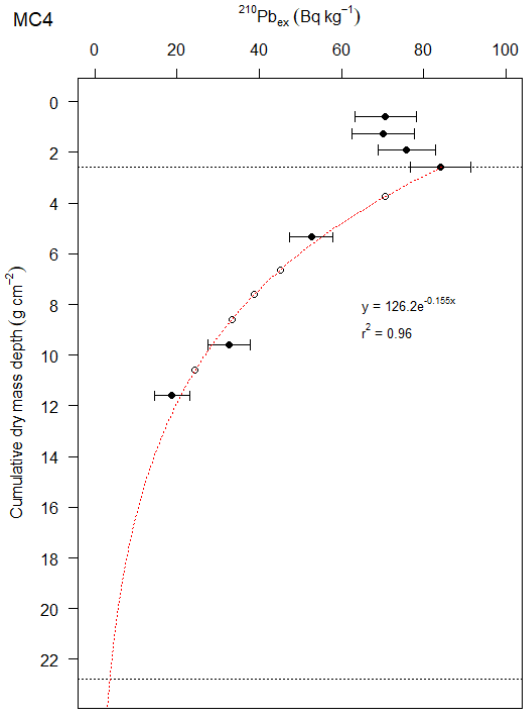
MC4
$^{210}Pb_{ex}$ (Bq kg^{-1})
Cumulative dry mass depth (g cm^{-2})
y = 126.2e$^{-0.155x}$
r^2 = 0.96

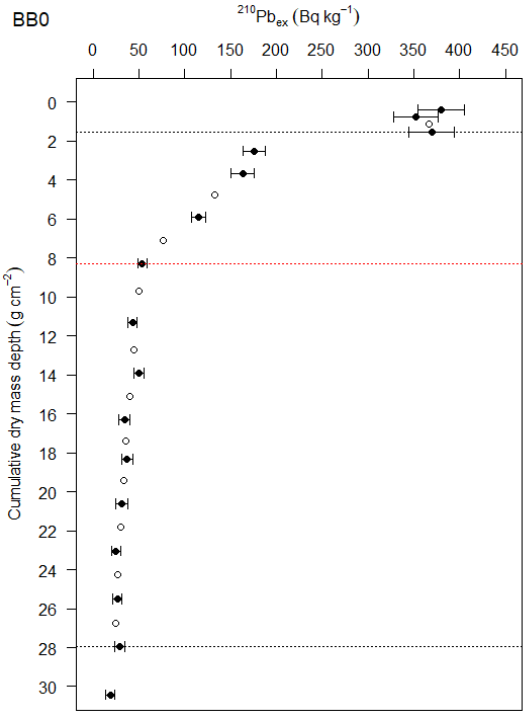
BB0
$^{210}Pb_{ex}$ (Bq kg^{-1})
Cumulative dry mass depth (g cm^{-2})

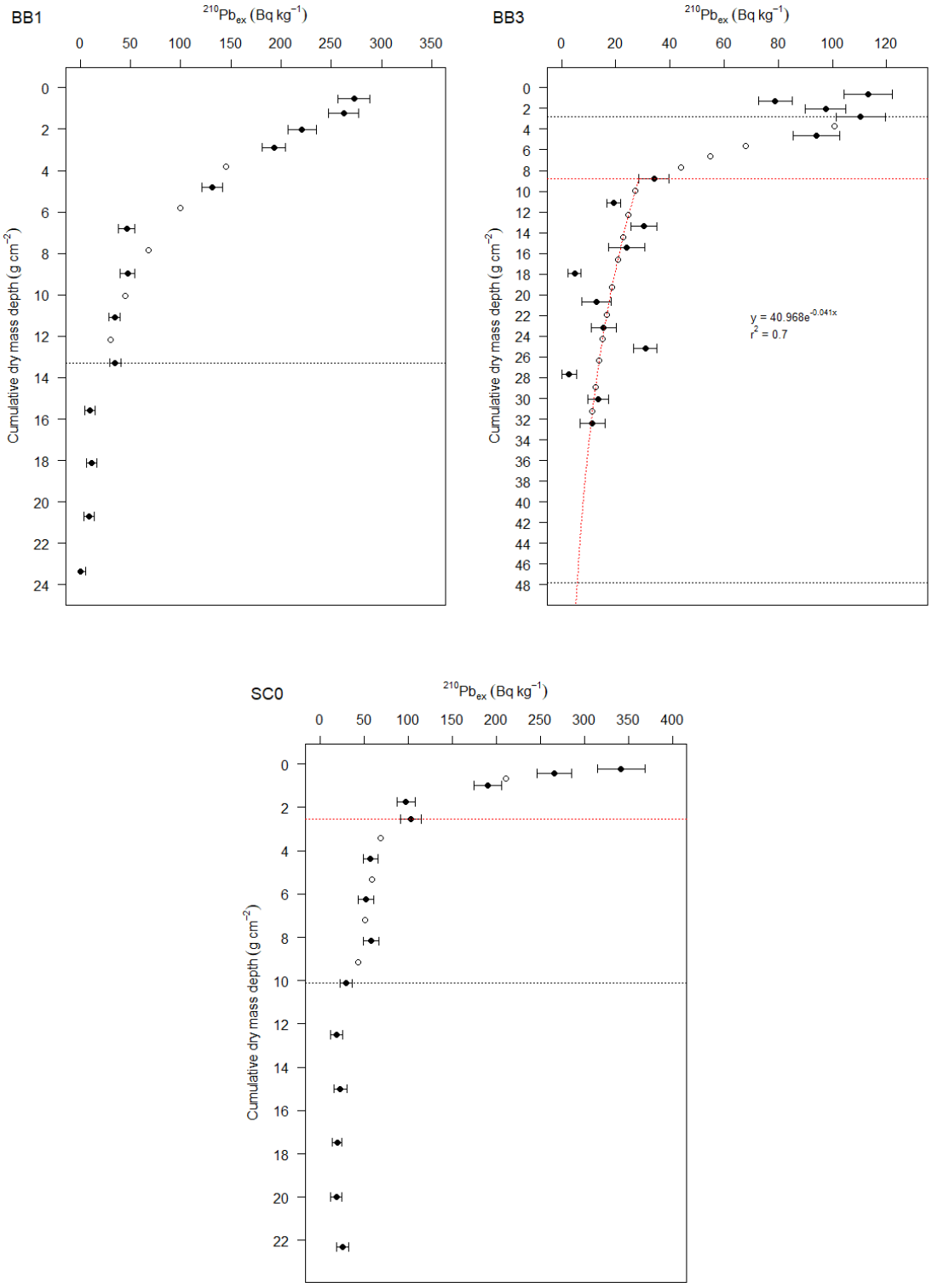

Figure 4.1. $^{210}Pb_{ex}$ activity concentration profiles. Black dotted lines represent the interpreted surface mixed layer (top) and equilibrium depth (bottom). Horizontal red-dotted lines indicate a change in the slope of exponential decay. For cores in which equilibrium depth is not reached, the exponential regression curve used to extrapolate values is represented by a red-dotted line. Error bars represent 1σ. Open symbols represent interpolated values.

The estimated ages (Figure 4.2) of the base of the cores ranged from 46 ±2 (MC0) to >111 years (BB0), and MARs (Figure 4.3) ranged from 0.04±0.02 g cm^{-2} yr^{-1} (base of SC0) to 0.75±0.11 g cm^{-2} yr^{-1} (BB3). In Marian Cove, the highest rate was found in core MC0 (mean = 0.41±0.04 g cm^{-2} yr^{-1}), outside the mouth of the fjord, followed by the ice-proximal location, MC4 (mean = 0.15±0.02 g cm^{-2} yr^{-1}), with the lowest MARs occurring in the mid-fjord core, MC2 (mean = 0.08±0.02 g cm^{-2} yr^{-1}). There was no significant (p<0.05) relationship between MAR and depth-in-core for any of the Marian Cove cores.

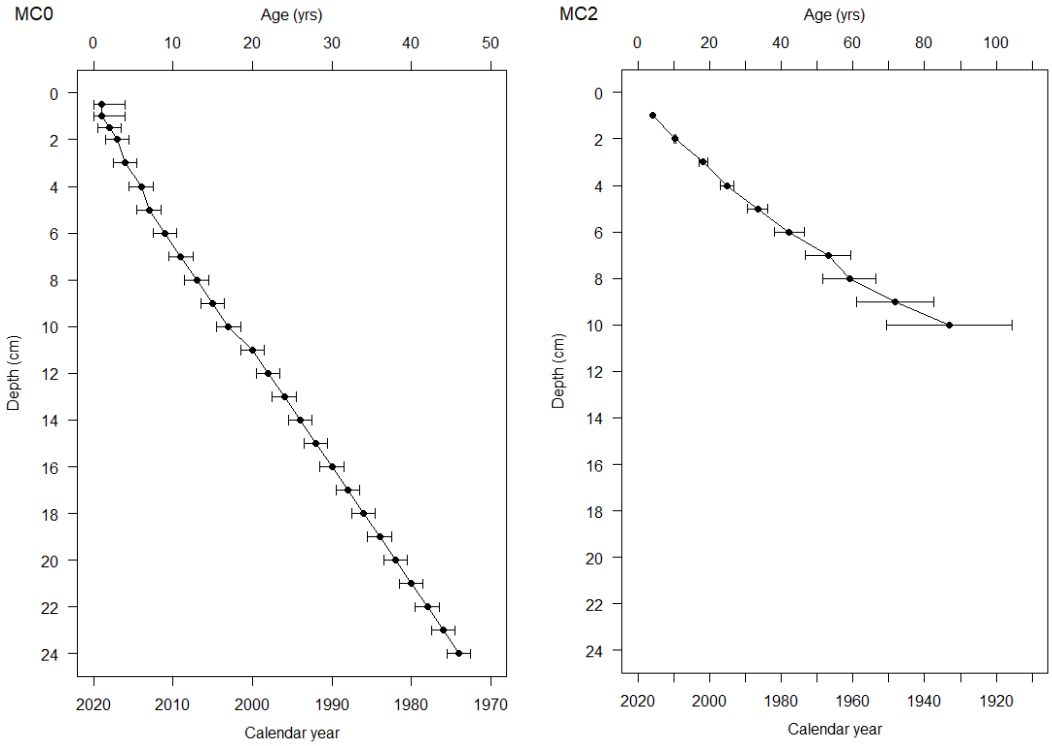

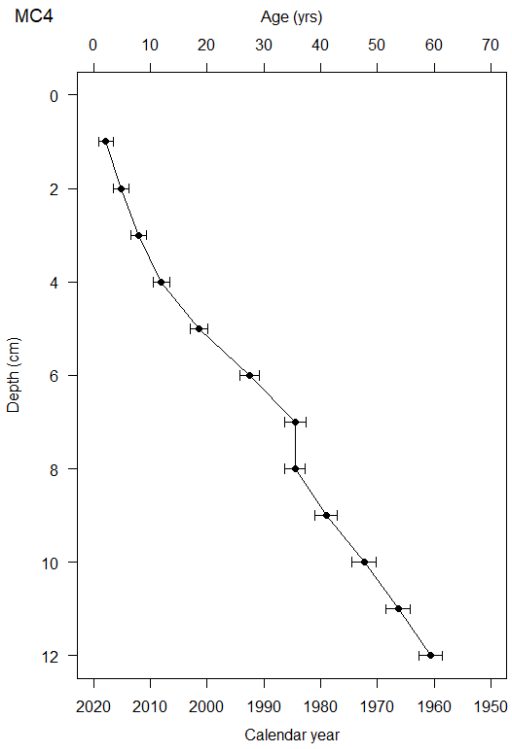
MC4
Age (yrs)
0 10 20 30 40 50 60 70
Depth (cm)
0 2 4 6 8 10 12
2020 2010 2000 1990 1980 1970 1960 1950
Calendar year

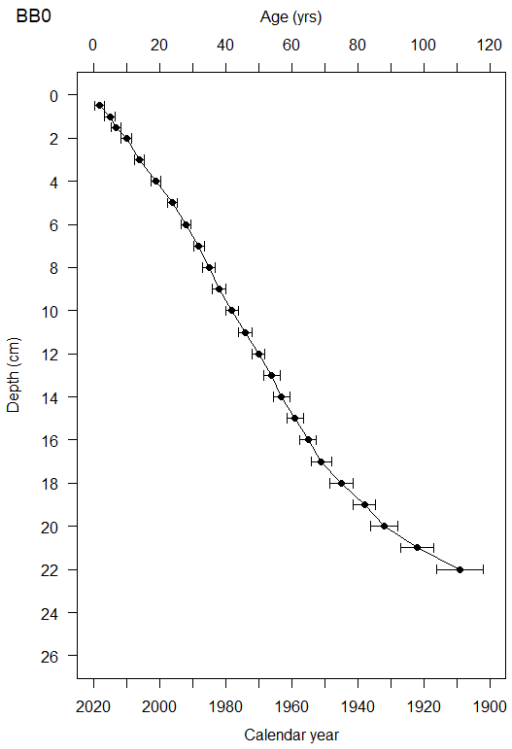
BB0
Age (yrs)
0 20 40 60 80 100 120
Depth (cm)
0 2 4 6 8 10 12 14 16 18 20 22 24 26
2020 2000 1980 1960 1940 1920 1900
Calendar year

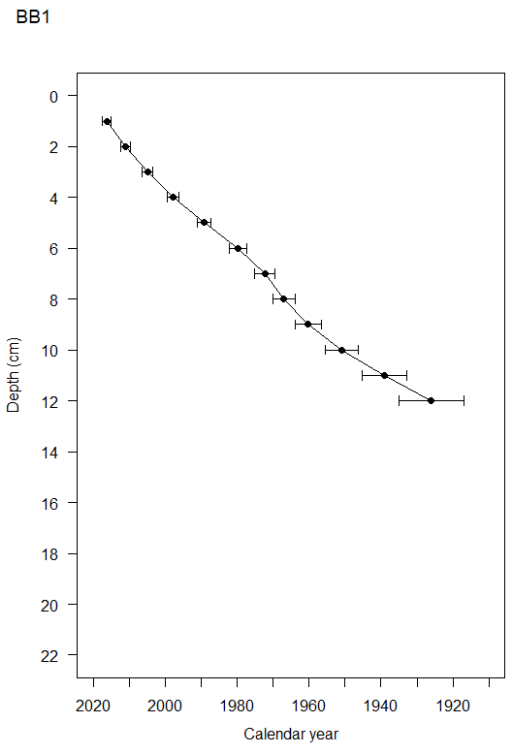
BB1
Depth (cm)
0 2 4 6 8 10 12 14 16 18 20 22
2020 2000 1980 1960 1940 1920
Calendar year

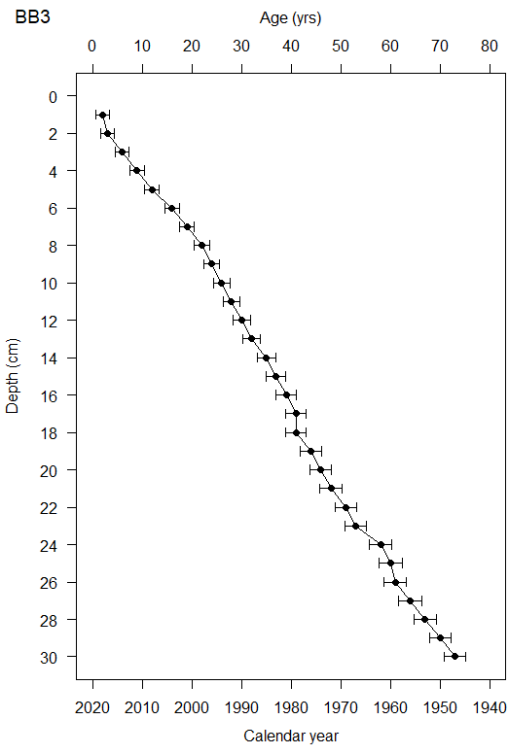
BB3
Age (yrs)
0 10 20 30 40 50 60 70 80
Depth (cm)
0 2 4 6 8 10 12 14 16 18 20 22 24 26 28 30
2020 2010 2000 1990 1980 1970 1960 1950 1940
Calendar year

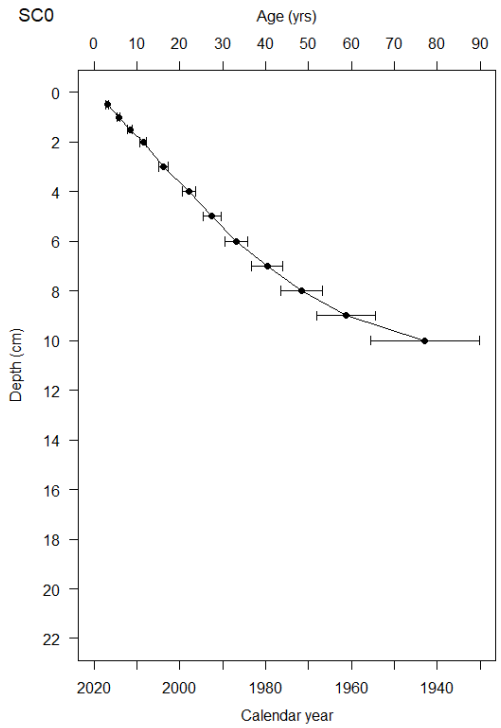

Figure 4.2. ^{210}Pb-derived ages plotted against depth-in-core. Error bars = 1σ.

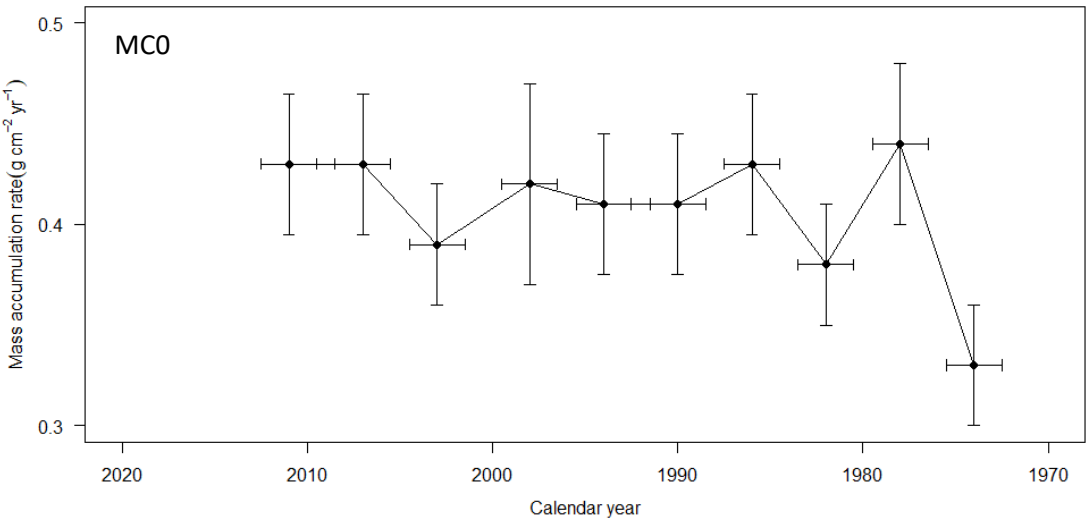

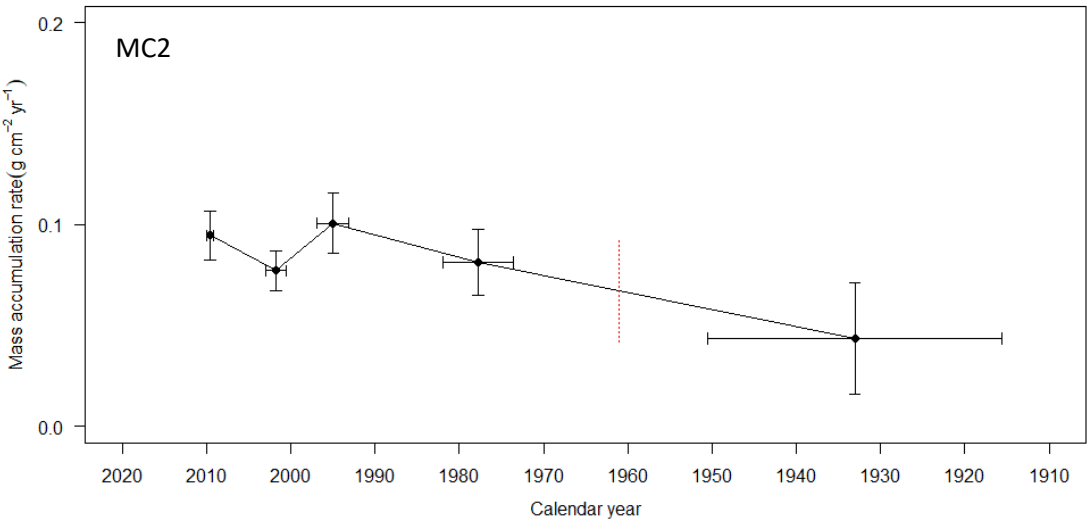
MC2
Mass accumulation rate(g cm^{-2} yr^{-1})
0.0
0.1
0.2
2020
2010
2000
1990
1980
1970
1960
1950
1940
1930
1920
1910
Calendar year

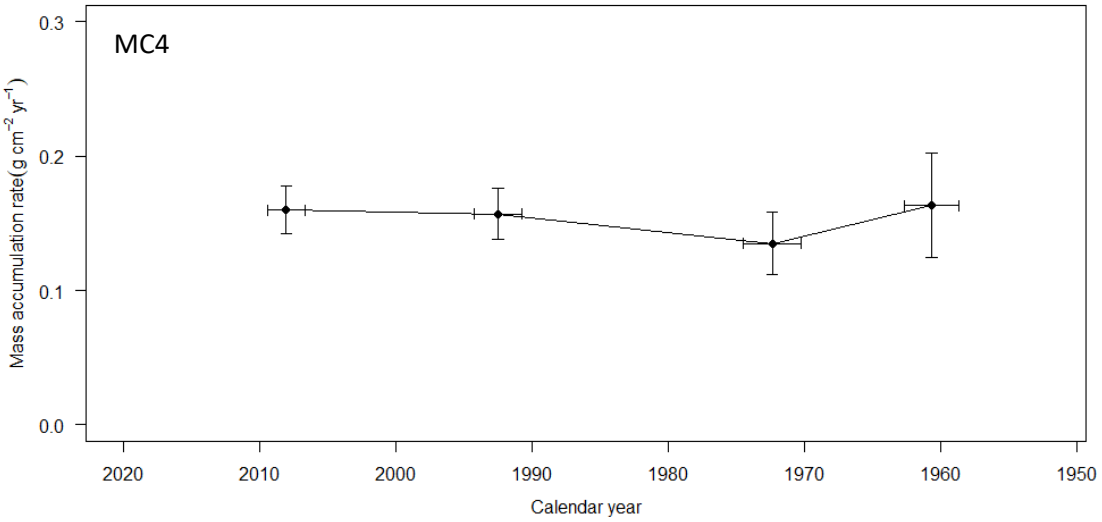
MC4
Mass accumulation rate(g cm^{-2} yr^{-1})
0.0
0.1
0.2
0.3
2020
2010
2000
1990
1980
1970
1960
1950
Calendar year

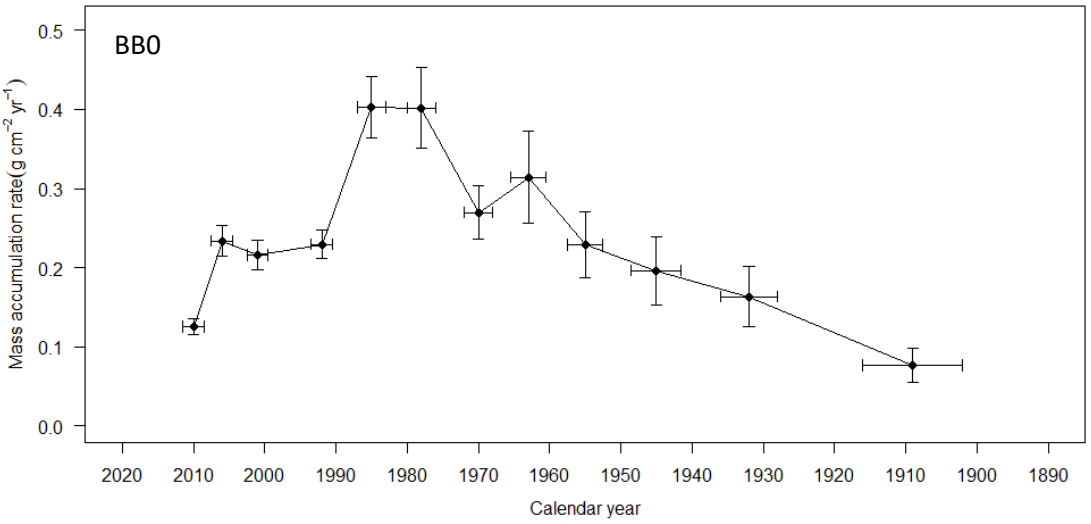
BB0
Mass accumulation rate(g cm^{-2} yr^{-1})
0.0
0.1
0.2
0.3
0.4
0.5
2020
2010
2000
1990
1980
1970
1960
1950
1940
1930
1920
1910
1900
1890
Calendar year

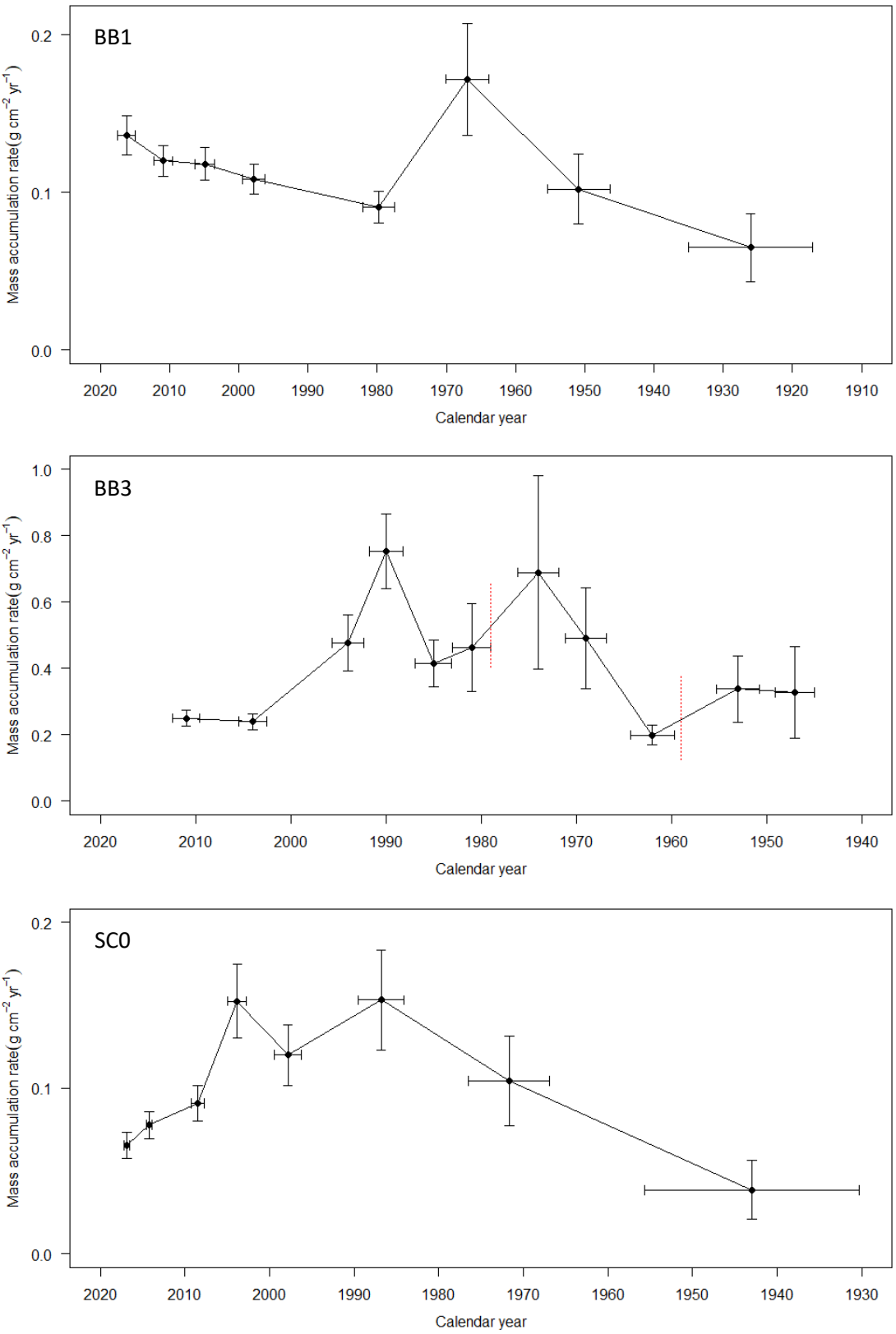

Figure 4.3. Mass accumulation rates. Red dashed lines indicate very low $^{210}Pb_{ex}$ values, which result in very high calculated MAR values but have significant associated uncertainty. Error bars = 1σ.

In Börgen Bay the highest rates were found proximal to the ice-front in core BB3 (mean = 0.42±0.11 g cm^{-2} yr^{-1}), followed by the outer bay site BB0 (mean = 0.24±0.03 g cm^{-2} yr^{-1}), with the mid-fjord site, BB1, again exhibiting the lowest MARs (mean = 0.11±0.02 g cm^{-2} yr^{-1}). Although there was no linear relationship between depth and MAR, general patterns in MAR, characterised by one or more peaks at mid-depth, were observed in all three Börgen Bay cores.

From the base of BB0 MAR steadily increased with depth up to a peak of 0.40±0.04/0.05 g cm^{-2} yr^{-1} at 10 and 8cm depth (calendar years 1985±2 and 1978±2), followed by decreasing MARs. A much smaller peak was observed at 14cm (1963), though was within the range of uncertainty (1σ) of the samples above and below, and as such may simply be an artefact of analytical error. For core BB1 MAR increased with decreasing depth, with the exception of a pronounced peak at 8cm (1967±3) of 0.17±0.04 g cm^{-2} yr^{-1}. In BB3, MAR was highly variable, with a peak of 0.75±0.22 g cm^{-2} yr^{-1} at 12cm (1989±2). At 18 and 26cm (1978±2 and 1958±2) extremely low $^{210}Pb_{ex}$ values were observed, corresponding to very high calculated MARs, though the magnitude of these peaks had significant associated uncertainties and as such they were not included in plots or calculations of mean MAR, represented instead with red dotted lines as “episodic sediment delivery events” (Boldt et al., 2013). MARs for SC0 at Ryder Bay (mean = 0.10±0.02 g cm^{-2} yr^{-1}) exhibited a similar pattern, with peaks of MARs of 0.15±0.02/0.03 g cm^{-2} yr^{-1} at 6cm and 3 cm depth (1987±5 and 2004±2), followed by decreasing MARs with depth.

Table 4.1. Summary of relevant ^{210}Pb results for each core.

Core name	Depth (m)	Latitude (˚)	Longitude (˚)	Distance from ice front (km)	Surface $^{210}Pb_{ex}$ (Bq kg^{-1})	±	SML depth (cm)	Mean MAR (g cm^{-2} yr^{-1})	±
Marian Cove									
MC0	225	-62.220	-58.816	5.5	316	25	6	0.41	0.04
MC2	110	-62.214	-58.770	3	114	10	3	0.08	0.02
MC4	124	-62.207	-58.740	1.3	84	8	4	0.15	0.02
Börgen Bay									
BB0	313	-64.765	-63.473	7.4	379	26	2	0.24	0.03
BB1	258	-64.741	-63.451	4.9	273	16	-	0.11	0.02
BB3	301	-64.717	-63.454	2.3	113	9	4	0.42	0.11
Ryder Bay									
SC0	364	-67.598	-68.102	13	342	27	-	0.10	0.02

4.2 Carbon Content

Concentrations of TOC were relatively consistent across all sediment cores, with mean values ranging from 0.28-0.60 ±0.02%, though varied significantly with depth. Typically, profiles consisted of an upper-most section of relatively uniform concentrations (2-5cm) followed by decreasing values with depth; in some cores (MC2, BB3, and SC0), however, no uniform upper section was present. Cores MC0, MC2, and BB3 additionally exhibited a lower region of uniform concentrations, though it is unclear whether the absence of such patterns in the other cores was a result of low sampling resolution in the deeper sections (e.g., core SC0). In cores SC0 and BB0 relatively uniform concentrations were observed mid-depth in the core, with subsequent decreased values. Generally, the highest carbon concentrations were found in the most ice-distal sites, and the lowest in the ice-proximal sites. Between fjord systems, Ryder Bay exhibited the highest concentrations, followed by Marian Cove, then Börgen Bay.

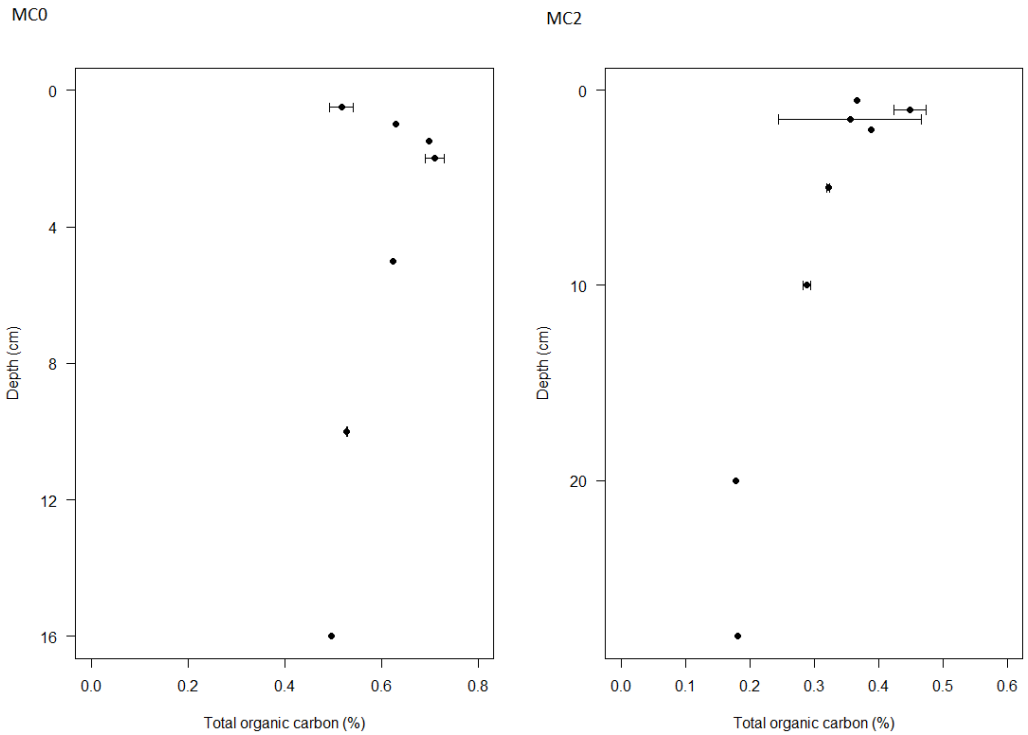

MC4

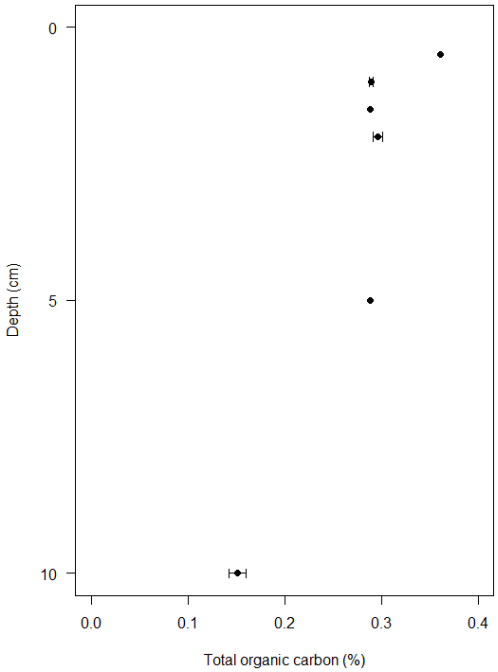

BB0

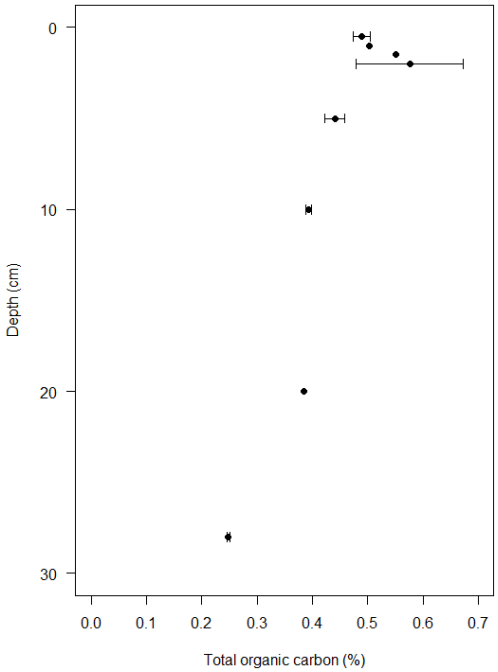

BB1

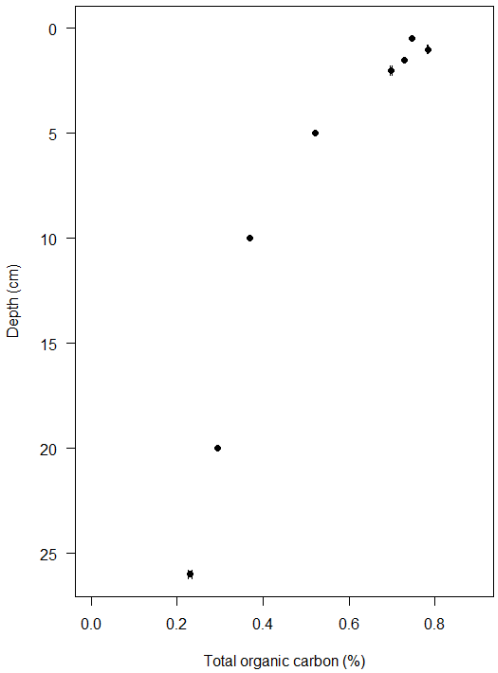

BB3

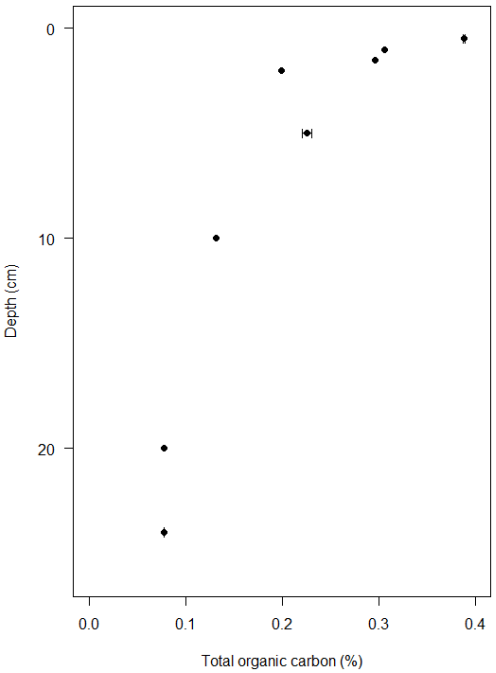

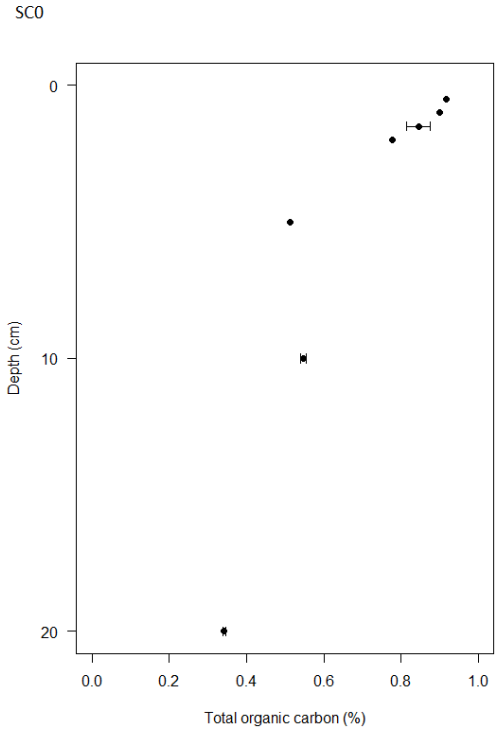

Figure 4.4. Total organic carbon content. Where possible, error bars denote 1σ.

Chapter 5: Discussion

5.1 ^{210}Pb Age-Depth Models and Sediment Mass Accumulation Rates

Surface activity concentration of $^{210}Pb_{ex}$ depends on various factors, which can be broadly categorized into factors controlling flux to the water column, and factors controlling removal by, and deposition within, the sediment. $^{210}Pb_{ex}$ flux to the water column at any particular site is controlled by regional atmospheric concentration of ^{210}Pb, processes controlling removal of ^{210}Pb to the water surface (precipitation and dry deposition), and subsequent redistribution of these ^{210}Pb-enriched waters by ocean currents (Appleby, 2001). The fraction of this ^{210}Pb that then reaches the sediment and is deposited on the seafloor is modulated by grain size (^{210}Pb preferentially adsorbs to fine-grained particles), sedimentation rate (dilution of ^{210}Pb), and residence time of both the particles and the ^{210}Pb-enriched water within the water column. Thus, spatial and temporal variations in $^{210}Pb_{ex}$ surface activities are of interest independent of their application in age-depth modelling, as they can inform on variations in local conditions.

5.1.1 Marian Cove

The $^{210}Pb_{ex}$ surface activity concentrations of the cores in this study varied markedly. In Marian Cove, MC0 surface $^{210}Pb_{ex}$ was 316±25 Bq kg^{-1}, dropping to 113±10 Bq kg^{-1} for MC2, and 84±8 Bq kg^{-1} for MC4. A reasonable hypothesis to explain this pattern would be increased sedimentation rates proximal to the ice-front at the head of the fjord resulting in dilution of $^{210}Pb_{ex}$. However, mass accumulation rates for the three sites refute this, with MC0 exhibiting the greatest average MARs. Proximity to the retreating ice-front may still partially explain this pattern, though instead due to the more proximal sites receiving coarser material which less readily adsorbs ^{210}Pb and has a lower residence time within the water due to rapid sinking. However, as grain-size typically exhibits an exponential relationship with distance from the fjord-head (Domack & Ishman, 1993), and MC2 is already at considerable distance (3 km) from the ice front, further changes in mean grain size towards site MC0 will likely be negligible. Additionally, grain-

size effects will be limited by the sample preparation procedure described in section 4.1.

A more likely explanation is that $^{210}Pb_{ex}$ activity varies within the water column above the sites. The general circulation within Maxwell Bay (Figure 2.2) shows that water enters the bay to the south-west and moves clockwise around the bay. It is suggested that as the water circulates past the site at MC0, $^{210}Pb_{ex}$ is rapidly scavenged by fine-grained SPM. This ^{210}Pb-depleted water then circulates into Marian Cove, where $^{210}Pb_{ex}$ is further scavenged by the surface SPM within the cove. However, Yoon et al. (2015) demonstrated that the majority of surface SPM is exported out of Marian Cove, removing this ^{210}Pb from the fjord. As such, the coarser sediment that ends up deposited within the cove is severely limited in ^{210}Pb, whilst comparatively higher concentrations of ^{210}Pb are found outside the fjord, such as at site MC0. These patterns are enhanced by the water-depth from which the cores are taken: site MC0 is in greater water depth than MC2 and MC4, which allows for a greater residence time of sediment particles within the water column and subsequently greater ^{210}Pb adsorption (Eidam et al., 2019).

The MARs reported for Marian Cove in this study were of a similar magnitude to those reported in previous studies, which range from 0.1-0.8 g cm^{-2} yr^{-1} (Table 2.1). Cores MC2 and MC4 were taken from the same individual mid- and inner-fjord basins as cores KC21 and KC22 from Boldt et al. (2013). MARs reported for the lower part of KC22 are similar to the mean MAR calculated for MC2, though diverge in the upper part of the core. The MARs reported for KC21, on the other hand, are two to four times higher than those calculated here for MC4, possibly reflecting a high degree of variability in sedimentation within these basins, as KC21 was taken closer to the northern edge of the cove, while core MC4 was situated in the deepest part of the basin.

The typical glacimarine down-fjord gradient in mass accumulation rates was not observed in Marian Cove, suggesting a diverse source of sediments (Munoz & Wellner, 2016). Previous work on SPM in Marian Cove suggests that most surface SPM is transported out of the cove and exported to Maxwell Bay, and thus the mid-depth cold tongue generated from subglacial meltwater represents the most important source of sediments within the cove (Yoo et al., 2015). The

data presented here lend credence to this hypothesis, with sedimentation rates within the cove (sites MC2 and MC4) being substantially lower than those just outside the fjord mouth (MC0). Furthermore, as this cold-tongue occurs at depth, it would be unable to override the bathymetric sill separating the innermost basin from the middle basin, explaining the low sedimentation rates for MC2. Numerous meltwater streams, from land-terminating glaciers, enter the bay to the north of Marian Cove, and likely contribute to the higher sedimentation rates at MC0. Whilst the more open-ocean setting of MC0 might result in greater primary productivity and thus biogenic sedimentation, OC content of all cores at Marian Cove was low (<1% - see section 4.2), and thus this would be relatively uninfluential on overall sediment accumulation rates. This spatial pattern of sedimentation rates within Marian Cove, despite recent rapid retreat of the tide-water glacier at the head of the cove, suggests that meltwater processes may be a more important control on sedimentation rates than calving and subaqueous ablation.

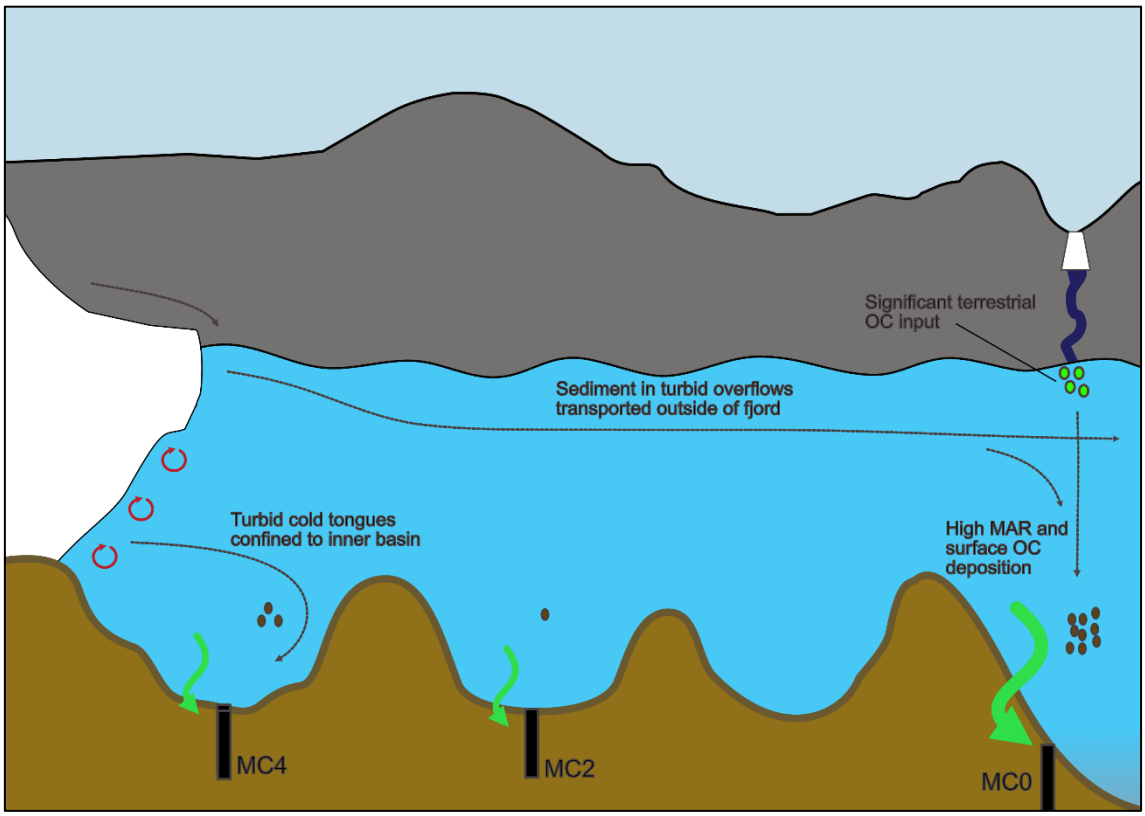

Figure 5.1. Inferred physical and biological processes occurring in Marian Cove.

Vertical profiles of $^{210}Pb_{ex}$ in all cores at Marian Cove suggest steady state accumulation over time, with no appreciable changes in the exponential decay

function. Resultingly, none of the cores in Marian Cove exhibited temporal trends in MAR. These findings are surprising given the increasing temperature and precipitation over the past 50 years (Turner et al., 2016). This is particularly interesting when compared with the results presented in Boldt et al. (2013), who reported a shift in sedimentation rates, generally occurring between 10-20cm depth, on the basis of which they inferred a shift of glaciation style in the South Shetland Islands from cold- to warm-based. Monien et al. (2017) also reported an increase in MAR in recent decades, though this trend was only present in two cores (P03 and P09), while core K44, located proximally to core P03, showed no increase. The results of this current study, as well as those presented in Monien et al. (2017), indicate that not only are spatial patterns in mean MAR highly variable, temporal shifts in MARs may also be dampened by local processes, highlighting the potential problems with using MARs in AP fjords to infer regional paleoenvironmental changes.

5.1.2 Börgen Bay

In Börgen Bay $^{210}Pb_{ex}$ surface activities varied substantially. As observed at Marian Cove, the outer site, BB0, had the highest $^{210}Pb_{ex}$ activity at 379±26 Bq kg^{-1} (of a similar magnitude to MC0), followed by BB1 at 273±16 Bq kg^{-1}, and finally BB3 at 113±9 Bq kg^{-1}. This pattern can likely be explained by sedimentation dynamics; BB3 has higher sedimentation rates than BB0 and BB1, and due to proximity to the ice-front would be expected to have a higher contribution of coarser particles, both of which would act to reduce the supply of $^{210}Pb_{ex}$ to the seabed sediments.

Cores BB0 and BB3 exhibited a marked change in the rate of decrease of $^{210}Pb_{ex}$ down-core (at 10-12cm and 8cm depth, respectively), providing preliminary evidence of variable MARs over time, whilst the decrease in activity of $^{210}Pb_{ex}$ in core BB1 was relatively consistent over-time.

The MARs for cores taken from Börgen Bay varied, though all fall within the range of previously reported MARs for nearby Gerlache Strait, Bismarck Strait and Andvord Bay (Table 2.2). BB3, proximal to the ice front, had the highest MAR, with a mean of 0.42 g cm^{-2} yr^{-1}, with the intermediate core site (BB1) exhibiting

the lowest mean MARs of 0.11 g cm^{-2} yr^{-1}, and the distal site (BB0) recording mean MARs of 0.24 g cm^{-2} yr^{-1}.

Both BB1 and BB0 are located outside the main northern-sector fjord, within the larger embayment, and thus the lack of a proximal-distal gradient in MAR may reflect additional sediment sources within the main bay region. However, the relatively high rates of MAR found in BB3 indicate that unlike at MC, a substantial fraction of glacial sediment yield is deposited within the inner basin of the fjord. The glacier in the western sector of Börgen Bay may also contribute sediment to sites BB1 and BB0, though given the lower rates for BB1, despite greater proximity to the western-sector glacier than BB0, this is likely minimal.

In many fjord systems, productivity (and thus biogenic sedimentation) increases towards the fjord mouth due to reduced turbidity and a more stable upper water column (Domack & Ishman, 1993); this is unlikely the primary cause of the difference between BB0 and BB1, as although carbon flux was greater at BB0, carbon content was relatively similar for both cores, indicating that the difference is due to lithic sedimentation.

In some studies unexpectedly low MARs have been attributed to winnowing of fine material by strong currents (typical of estuarine circulation in fjords) (Munoz & Wellner, 2016), but again, this is unlikely to be the cause of the differences observed here, as under such circumstances one would expect significantly lower $^{210}Pb_{ex}$ activity in BB1 – this was not the case.

Alternatively, the differences in MARs may simply be a function of circulation patterns, either due to circulation dynamics outside the bay resulting in allochthonous input from the Neumeyer Channel, or intra-bay circulation dynamics that result in sediment-laden meltwater and icebergs being directed away from the site at BB1. One such plausible scenario might be strong surface flow resulting from estuarine circulation resulting in both a short residence time of icebergs and fine material remaining in suspension over the site at BB1.

The maximum age at the base of BB3 indicates that sediment deposition has been occurring prior to the retreat of the ice front past the core location (Figure

2.5), implying that the ice-front observed in the satellite data was floating over the deep basin, rather than grounded. This would explain the pattern of ice retreat observed in the satellite data, whereby substantial retreat occurred in the middle of the ice front, but towards the edges, in shallower bathymetry, the ice front remained relatively stable. Furthermore, it would reconcile the differences in ice-front retreat between the western and northern sector. In the western, shallower sector of Börgen Bay, very little ice front retreat occurred over the satellite record, despite close proximity to the northern sector which underwent significant retreat, consistent with observations that glaciers with floating ice fronts are more susceptible to retreat than those with grounded termini (Silva et al., 2020).

Variations in MAR over time for all cores from Börgen Bay exhibited similar patterns, with peaks and troughs occurring synchronously, providing preliminary evidence for the validity of the associated age-depth models. The differences that do exist between cores are likely a result of the relative importance of glacier front retreat on the distance from the core site to the front. Rates of accumulation typically decrease exponentially away from the ice front (Cowan et al., 1997; Jaeger & Nittrouer, 1999), and the same rate of retreat will result in a relatively greater increase in distance to the ice front for proximal sites compared with distal sites. The retreat of 0.6 km between 1997-2003, for example, represented an increase in distance of 120% for BB3, but an increase of just 10% for BB0. Under such circumstances, BB0 could, in effect, be considered as a ‘control site’, simply recording variations in sediment production (albeit dampened by external sources), relatively unaffected by variations in frontal position, whilst the signal of sediment yield at BB3, on the other hand, is overprinted by the stronger effect of ice front retreat acting to increase the distance of the core site from the ice front. Furthermore, variations in MAR are interpreted to represent variations in lithic sedimentation, as in all cases carbon content was <1% (Figure 4.4).

At site BB3 a prominent peak in MAR was recorded at 1993 (±2). Extremely low $^{210}Pb_{ex}$ values, indicative of episodic sediment delivery (Boldt et al., 2013), were also measured at 1958 and 1978 (±2). As core BB3 has low initial concentrations of $^{210}Pb_{ex}$, and these minima occurred at depth, the propagated uncertainties associated with the magnitude of MAR calculated from these values are high, though the presence of such low values does indicate that substantial

sedimentation occurred (Boldt et al., 2013). The patterns of MAR for BB3 are likely a function of variations in glacial sediment yield, overprinted by periods of ice front instability and retreat which in turn led to a relative increase in the distance between the ice front and the core site and a subsequent reduction in the fraction of sediment reaching the core site. This would explain the reduction in the apparent magnitude in sedimentation for the peaks observed at 1993 compared to those towards the base of the core (when the core site would have been extremely ice-proximal).

In addition to generally low MARs, the only peak resolved in core BB1 (mid-bay) was at 1967 (±3), though the apparent lack in subsequent MAR peaks may be due to sampling resolution, as the low rates of accumulation resulted in low temporal sampling resolution, despite equal sampling with regards to depth-in-core.

In the most distal core (BB0) sedimentation rates steadily increased from the base of the core. At 1963 (±3) a slight increase in MAR was recorded, contemporaneous with the first episodic sediment delivery event in BB3 and the peak in MARs in BB1, though this is within the range of uncertainties associated with measurements of samples above and below. A subsequent peak, coincident with the second episodic sediment delivery event in BB3 (1978±2) was recorded at 1978 and 1985 (±2). It is unclear whether this represents continuously high sedimentation over this time period, or if a drop in MAR occurred in-between the samples.

In either case, the identification of these two peaks, concurrent with the two most prominent peaks in MAR in core BB3, would indicate that this represents a general increase in glacial sediment yield, as opposed to localised events. Interestingly, the 1993±2 peak in BB3 was not apparent in BB0. This may be due to sampling resolution, as no measurement was taken at 5cm depth (1991-2002), or may indicate that in core BB3 this was a discrete, localised event, as opposed to a general increase in sediment production. MARs remained low from this point until present, as was recorded for BB3, indicating a general reduction in sediment yield.

Glacier retreat on the mid- and southern- latitude WAP has been demonstrated to be primarily driven by the upwelling and warming of CDW, and the intrusion of this warm water into fjords and bays, resulting in increased ice calving and basal melting (Cook et al., 2016). Observations of Anvers Island corroborate this interpretation, as meltwater in the region is rare (Rundle, 1973; Honkala, 1970). Indeed, a study on a fjord system just 25km from Börgen Bay (Arthur Harbor), on the west coast of Anvers Island, found that though a small amount of meltwater drained from the glacier surface, no sub- or englacial meltwater was detected entering the fjord from the glacier, and that the most important sources of sediment were through direct subaqueous melting of the submerged ice-front and the melting of calved glacial ice (Ashley & Smith, 2000). The limited meltwater draining from the ice surface is likely to transport relatively little sediment, as observations of glacial ice from Anvers Island indicate that most sediment is entrained within the basal (~0.5 m) layer (Ashley & Smith, 2000). Furthermore, within Börgen Bay itself, calving processes appear to be a primary driver of modern ice front retreat (Meredith et al., 2022), and CDW has repeatedly been observed within the bay via CTD measurements (K. Sheen, *pers. comms*).

Under such a scenario, variations in glacial sediment yield will reflect the release of entrained sediment from melting glacial ice, as opposed to an increase in sediment *production* resulting from higher meltwater delivery to the ice-bed interface. This sediment release may occur *in situ*, from direct basal melting of the ice-front or tongue, whereupon coarse material would be deposited proximally, and finer material would be suspended within the water column and subsequently distributed by currents; or by the melting of calved ice, allowing for the distal deposition of coarse and fine material.

Here, it is argued that patterns of MAR in Börgen Bay can be explained by oceanographic regime, modulated by local bathymetry and fjord geometry, resulting in changes in entrained sediment release and the local depositional environment. Prior to observational (satellite) data, ice fronts were likely extended due to significantly cooler temperatures experienced during the Little Ice Age; bathymetric data indicate that this was the case in Börgen Bay, with glacial features on the seabed extending out to the Neumeyer Channel (Rodrigo & Herbstaedt, 2021).

The phase of retreat observed at the start of the satellite data (1955-1956) – which is four times higher than the retreat rate observed during other phases of retreat at Börgen Bay – may represent a continuation of a retreat from the mouth of the northern-sector fjord, whereupon it would have been stabilised by the narrow geometry and prominent sill. Narrower fjord-geometries and shallow bathymetries can function as pinning points for ice due to the increased lateral drag that is exerted on the glacier (Benn et al., 2007); this is a common feature of glacier retreat on the AP (Batchelor et al., 2019). Such a position, with an ice-tongue either directly pinned on a prominent sill, or terminating in the shallow waters above it, would limit the intrusion and access of CDW to the ice front and base (Smith et al., 2017), as well as inhibiting lateral stress and calving (Benn et al., 2007; Favier et al., 2016), thus limiting entrained-sediment release. This would explain the low MARs, and low variability in MAR, at BB0 prior to 1955.

Following this rapid retreat observed at 1955, increased access of CDW to the base of the ice-tongue and front of ice would have allowed for increased basal melting and release of entrained sediment during periods of intrusion of CDW, as well as increased calving, explaining the increased MARs at BB0, BB1 and BB3. The notable peaks in MAR observed in the cores likely represents phases of increased CDW intrusion, or shoaling and warming of already intruding CDW (Schmidtko et al., 2014), and/or periods of increased ice-front calving. Over the latter half of the 20th century, the ice tongue progressively calved and retreated over the deep basin of the northern sector. At present, the glacier has no notable ice-tongue (Meredith et al., 2022), suggesting that this frontal retreat observed in the satellite data is a record of ice-tongue collapse, as has been observed across the AP (Cook & Vaughan, 2010; Davies et al., 2012; Friedl et al., 2018; Gomez-Fell et al., 2021; Miles et al., 2022). It is suggested that the reduction in MARs after ~1990 in cores BB0 and BB3 is a function of the loss of this ice tongue: when the ice-tongue is lost, the contact area between CDW and glacial ice is reduced significantly, limiting melting to the vertical front of the ice, thus resulting in significantly less glacially-entrained sediment release, as well as a reduction in the rate of calving.

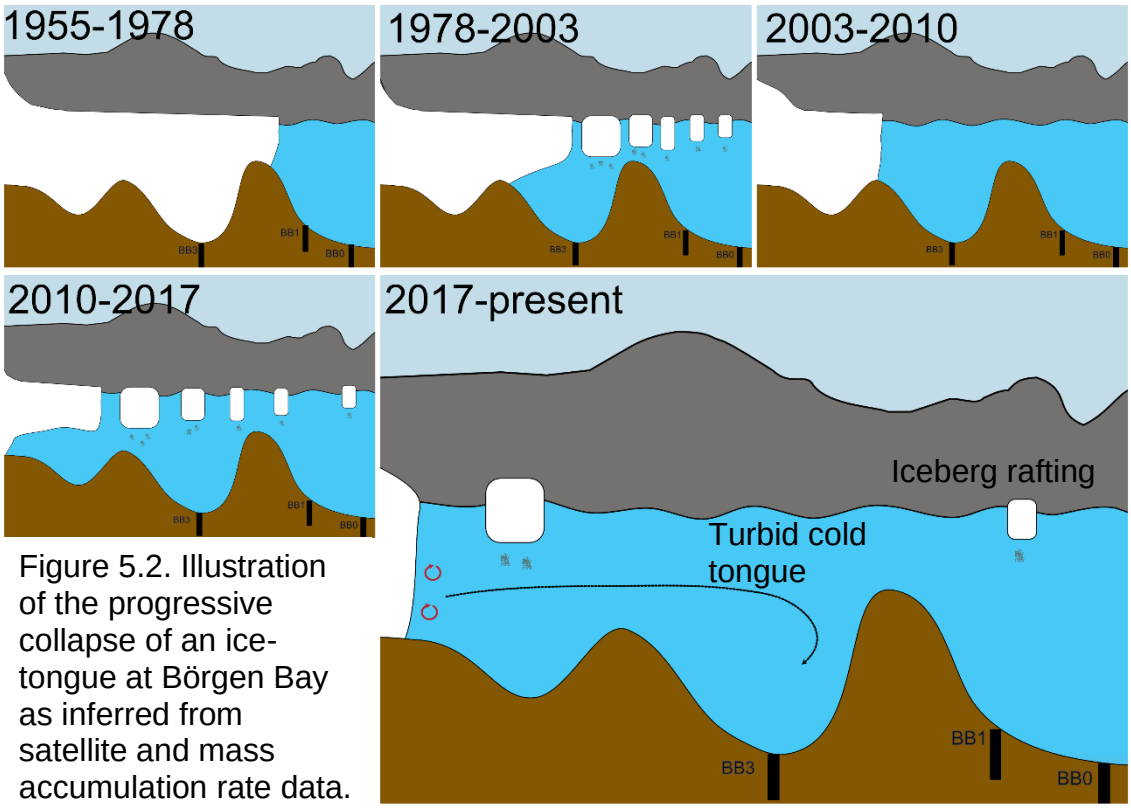

Figure 5.2. Illustration of the progressive collapse of an ice-tongue at Börgen Bay as inferred from satellite and mass accumulation rate data.

5.1.3 Ryder Bay

Core SC0 at Ryder Bay exhibited similar surface activities (350±27 Bq kg^{-1}) to the other outer-bay cores, implying a similar flux of ^{210}Pb across the AP. Two peaks in MAR at 1987 (±3) and 2004 (±1) were observed, coincident with the onset of ice-front retreat in the satellite record at 1989, which became relatively stable around 2003, indicating that these periods of high MAR may relate to ice-rafting of debris during calving events.

5.1.4 Summary of ^{210}Pb Age-Depth Models and Sediment Mass Accumulation rates

The patterns, magnitude and spatial variation in MARs at Marian Cove, Börgen Bay, and Ryder Bay implicate a diverse array of processes driving variations in sedimentation rates over the AP. In the north, sedimentation appears to be dominated by meltwater processes, with land-terminating glacial run-off contributing substantial sediment load and dampening the typical glacimarine proximal-distal gradient; at Marian Cove, the outermost core, MC0, had significantly higher MARs than the two intra-fjord sites. On the mid- and southern-

AP, on the other hand, sedimentation appears to be primarily driven by calving and the basal melting of ice by CDW. This is consistent with our understanding of climatic and oceanographic changes across the AP: in the north, surface air temperatures are frequently well above freezing, such that surface ablation and meltwater delivery to the ice-bed interface is significant (Monien et al., 2017; Meredith et al., 2018), whilst in the south, though air temperatures are significantly cooler, the shoaling and intensification of CDW has been shown to cause significant frontal retreat (Schmidtko et al., 2014; Cook et al., 2016). The apparent loss of a floating ice tongue in Börgen Bay's northern sector has worrying implications for future glacier stability (Miles et al., 2022)

Furthermore, these results have demonstrated that even within individual fjord systems, complex factors influence MARs at any given site, both spatially and temporally. General trends can be dampened or amplified by local processes, most notably the relative increase in distance to the core-site that occurs during frontal retreat, or overprinted by entirely different processes, with implications for studies that seek to reconstruct past glacial or climatic changes on the basis of sedimentation rates (Cowan et al., 2014; Cowan et al., 2010; Majewski et al., 2012; Milliken et al., 2009). Even the fundamental relationship between sedimentation and sediment production (erosivity) is complex, as variations in sedimentation rate can be a product of the release of entrained sediment, rather than any change to the production of sediment, complicating inferences on basin-wide erosion rates (e.g. Koppes et al., 2015; Wellner et al., 2016; Hogan et al., 2020). Overall, these results provide context for understanding past and future changes to sedimentation rates in AP fjords, but highlight the need to develop a rigorous understanding of individual fjord-systems and processes before undertaking such environmental reconstructions.

5.2 Carbon Content

Concentrations of organic carbon in all sediment cores analysed exhibited significantly decreasing values with depth. When organic matter, produced in the overlying water column, is deposited on the seafloor, it undergoes remineralisation by bacterial communities, and carbon is returned to the overlying seawater in the form of dissolved organic carbon (Keil et al., 2015).

Remineralisation is most significant in the upper, oxygenated sediment layers, and diminishes with depth, though will continue in the form of sulphate reduction to considerable depth.

The profiles of TOC observed in this study are interpreted to represent a function of progressive remineralisation of the freshly deposited surface TOC, leading to depleted values at depth. Such an interpretation is also consistent with the patterns in the rate of down-core decrease of TOC content, with the most significant decrease occurring just below the upper 2-5 cm, followed by continued, but slower reductions at mid-depth, and finally consistent concentrations at the base of cores of sufficient depth (age). The upper 2-5 cm of these cores generally corresponds to the depth of the surface mixed layer, as derived from the ^{210}Pb profiles, which would allow for oxygen replenishment and subsequently sustained aerobic respiration and rapid degradation of organic matter. Simultaneously, this mixing would result in homogenization of organic matter across this section, with freshly deposited organic matter interchanging with deeper, degraded matter. It would be expected, as was observed, that OC content would drop considerably just below this mixed layer, as no fresh organic matter is delivered to the sediment; oxygenation of the sediment would continue briefly until further burial prevents the percolation of porewaters and dissolution of oxygen, and all remaining oxygen is respired. Subsequently, in the sub- and anoxic zone, sulphate reduction would dominate, resulting in the slower, but continued degradation of OC resulting in the continued decrease in TOC observed, until OC is further buried. At this point, in the absence of oxygen and sulphur, remineralisation would cease, resulting in the relatively stable levels of TOC observed at the base of the older cores.

The fraction of the surface carbon that becomes remineralised is returned to the atmosphere, and thus has no effect on the partitioning of the carbon cycle, whilst the fraction of TOC that remains buried at depth is effectively sequestered, and thus represents carbon removed from the atmospheric and marine carbon reservoirs. Understanding the rate at which this occurs is crucially important for understanding the extent to which carbon is sequestered in the oceans, and has been a major focus of recent research.

5.2.1 Methodological Considerations

Antarctic fjords, in particular, have been highlighted as a potential significant sink of carbon as ice retreats and new benthic environments open up (Barnes et al., 2021). Organic carbon flux (g C m^{-2} yr^{-1}) can be calculated as MAR multiplied by TOC content (%). However, as demonstrated above, the carbon content of the upper and lower parts of the cores represent fundamentally different variables; carbon surface deposition (surface TOC%) and carbon burial/sequestration (lower TOC%). Therefore, two variables have been generated per core: deposition rate and burial rate of organic carbon. The difference between these two variables represents the fraction of deposited carbon that escapes remineralisation and eventually becomes sequestered: the burial efficiency. A summary of all terms used, and associated calculations, can be found in Table 5.1.

An important consideration of this methodology is the determination of the depth at which carbon can be considered sequestered. One approach would be to base this on the depth at which two consecutive measurements of TOC content are invariable, however, this is problematic for several reasons. Firstly, sampling resolution precludes this method for several of the cores, as only a single measurement is available at depth (core SC0, for example, consisted of a measurement at 20cm depth, with the previous measurement occurring at 10cm).

More fundamentally though (and irrespective of sampling strategies), this method may result in severe overestimation of carbon if ‘false plateaus’ are observed. The most obvious example of this issue can be seen when comparing core MC0 carbon contents to core BB0; in core BB0 a region of relatively consistent carbon content can be observed between 10 and 20cm, however the core penetrates to sufficient depth such that a subsequent reduction in content (at 28cm) is apparent. Core MC0, however, was shorter in length, such that, based on the above methodology, the relatively stable zone of carbon content observed after 10cm depth would be interpreted as sequestered carbon, when in fact it is likely that subsequent degradation would be observed at greater depths, as is seen in core BB0.

An alternative approach is to consider carbon deposited in sediment of sufficient age to be sequestered; typically this age is taken as 80-100 years (Koziorowska et al., 2018 and references therein). Comparing carbon content within each core with the age depth models generated in section 4, carbon burial rates have been determined for four of the cores. For three cores (MC0, MC4 and BB3) core depths were insufficient (and/or mass accumulation rates too high) to allow for the determination of carbon burial rates, as the lowermost samples are of insufficient age; remineralisation is likely still occurring at greater depths. Consequently, no determination of burial efficiency at these sites is possible.

It should be noted that whilst this “aged-carbon” approach is considered more appropriate than the one previously described, it is still subject to error. Notably, it relies on the assumption that all differences in carbon between the upper and lower samples is due to remineralisation, and ignores any changes in surface deposition over time as a result of varying primary production or degradation within the water column. Regionally, primary production in the Antarctic Peninsula has varied somewhat over recent decades due to changes in sea-ice duration and extent, though has been mitigated to some extent by photoinhibition due to increased intensity of ultraviolet-B radiation (Moreau et al., 2015). Long-term increases in primary productivity over the past century appears to be more pronounced in the southern regions of the AP, whilst in northern regions little change has been observed (Schofield et al., 2018). Furthermore, it is likely that some degradation of organic matter occurred in the surface layers of sediment prior to core collection such that carbon deposition rates are likely an underestimation of the true value; this effect will be more pronounced for cores with slower accumulation rates. These issues introduce some degree of uncertainty to estimations of carbon burial rates based on the above methodology, and are recognised as a limitation. Burial rates and efficiencies, should, therefore, be considered as maximum estimates.

Table 5.1. Summary of terms used in relation to carbon data

Term	Definition	Calculation	Unit
TOC content	The fraction of sediment comprised of TOC.	Experimental	%
MAR	The rate at which sediment accumulates.	Derived from ^{210}Pb data (see section 1.3)	g cm^{-2} yr^{-1}
Deposition rate	The flux of (organic) carbon to surface sediments.	MAR × surface TOC content	g C m^{-2} yr^{-1}
Burial rate	The flux of (organic) carbon to old (>100 yrs) sediment. Can be considered rate of sequestration.	MAR × deep TOC content	g C m^{-2} yr^{-1}
Burial efficiency	The fraction of (organic) carbon deposited in surface sediments that avoids remineralisation.	Burial rate / deposition rate	%
Preservation efficiency	The fraction of primary productivity that avoids remineralisation.	Burial rate / primary productivity	%

Table 5.2 Carbon flux, burial efficiencies, and preservation efficiencies of cores analysed in this study. No site-specific estimates of primary productivity were available for Börgen Bay.

Core name	Mean OC contents				Carbon flux					
	Surface		Buried		OC deposition rate		OC burial rate		OC burial	Preservation
	(%)	±	(%)	±	(g C m^{-2} yr^{-1})	±	(g C m^{-2} yr^{-1})	±	efficiency (%)	efficiency (%)
Marian Cove										
MC0	0.636	0.022	-	-	26.07	2.64	-	-	-	-
MC2	0.390	0.025	0.180	0.002	3.12	0.69	1.44	0.31	50	10[a]
MC4	0.305	0.004	-	-	4.57	0.75	-	-	-	-
Börgen Bay										
BB0	0.530	0.056	0.248	0.002	12.71	2.20	5.96	0.82	50	-
BB1	0.739	0.001	0.231	0.004	8.12	1.22	2.54	0.38	30	-
BB3	0.388	0.001	-	-	16.31	4.08	-	-	-	-
Ryder Bay										
SC0	0.860	0.030	0.343	0.004	8.60	1.58	3.43	0.62	40	2[b]

[a] Based on daily primary productivity reported in Yang (1990), assuming 100 days of productivity (Isla and DeMaster, 2021).

[b] Based on annual primary productivity reported in Rozema et al. (2017).

5.2.2 Interpretation of Results

Carbon deposition rates, burial rates, burial efficiencies and preservation efficiencies are presented in Table 5.2. Surface carbon deposition rates varied considerably between core sites, ranging from 3-26 g C m^{-2} yr^{-1}. The highest rate (26.07±2.64) was observed for the outer-fjord site of Marian Cove (MC0); considerably higher than the rates calculated for MC2 (3.12±0.69) and MC4 (4.57±0.75) within the cove. This may be due to the advection of organic matter due to local circulation patterns, or alternatively it could represent an input of allochthonous (terrestrial) carbon to site MC0, which receives much greater glacial sediment discharge due to its position adjacent to meltwater streams on the northern cliffs of Marian Cove. Gray et al. (2020), for example, describe significant algal blooms on the glaciers of the South Shetland Islands. Alternatively, this may represent input of petrogenic organic carbon (Berg et al., 2021), which would be problematic for estimations of carbon sequestration potential.

Preservation efficiencies (i.e., the fraction of marine primary production that avoids remineralisation in both the water column and sediment) lend credence to this hypothesis of increased terrestrial OC input. Taking a marine primary productivity estimate for Marian Cove of 14 g C m^{-2} yr^{-1} (calculated from daily rates of summer primary productivity reported by Yang (1990), and assuming 100 days of productivity as in Isla and DeMaster, 2021), and an assumed burial rate of 50% for MC0 and MC4 (for which direct calculations were not possible due to insufficient age), preservation efficiencies for the inner cove sites are estimated at 10 and 16% (for MC2 and MC4, respectively), consistent with observations across the AP (2-18% - Isla and DeMaster, 2021). Whilst MC0 sits outside of Marian Cove and so may be subject to more open-ocean conditions, even taking a higher primary productivity estimate of 30 g C m^{-2} yr^{-1} for Maxwell Bay (Yang et al. (1990), estimated preservation efficiency would be unreasonably high (43%) if marine primary productivity were the only source of organic carbon, indicating substantial allochthonous input. The contribution of terrestrial matter would not necessarily be proportionate to the excess preservation, however, as terrestrial organic matter is typically significantly more refractory than marine organic matter (Burdige, 2007; Cui et al., 2016; Smith et al., 2010).

At Börgen Bay, intra-fjord variability in surface OC deposition is lower. Values for BB0 and BB3 were similar (within 1σ), at 12.71±2.2 and 16.31±4.08 respectively, while slightly lower rates of carbon deposition were calculated for BB1. The consistency in deposition rates at BB0 and BB3 is surprising, as higher productivity is generally expected away from the fjord head (Domack & Ishman, 1993). This may instead indicate greater preservation within the water column at BB3 (for example due to adsorption to glacial iron (Faust et al., 2021)), or, alternatively, greater degradation of the surface carbon prior to core retrieval at BB0 due to lower mass accumulation rates. The lower deposition rates calculated for BB1 are possibly due to advection of OM away from the core site, consistent with interpretations of surface $^{210}Pb_{ex}$ activity, and/or, similar to above, related to pre-collection degradation.

When comparing entire fjord systems, marine carbon deposition rates were highest at Börgen Bay (12.38±2.50 g C m^{-2} yr^{-1}), followed by SC0 (8.6±1.58), and finally Marian Cove (3.85±0.72; not including MC0 due to inferred contribution of terrestrial OM). This is consistent with regional patterns of primary productivity across the AP, which indicate highest rates in the Gerlache Strait (close to Börgen Bay) of 300-750 g C m^{-2} yr^{-1} (Isla et al., 2002), followed by Ryder Bay (176-214 g C m^{-2} yr^{-1}; Rozema et al., 2017), and finally the Bransfield Strait (40-50 g C m^{-2} yr^{-1}; Isla & DeMaster, 2021). Preservation efficiency appears significantly lower at Ryder Bay than Marian Cove, consistent with observations of low export of primary production to depth reported by Weston et al. (2013), attributed to intensive grazing and remineralisation in the upper water-column.

Burial efficiencies were relatively consistent between coring locations (30-50%), though were only able to be calculated for four sites. This low sample size precludes robust analysis of factors driving burial efficiencies, though based on this preliminary evidence there appears to be little or no relationship between burial efficiency and mass accumulation rate, which is surprising given previous expectations (e.g., Arndt et al., 2013). Furthermore, there was little variation in burial efficiency between the three fjords, despite differences in climate and oceanographic regime, indicating some commonality across Antarctic Peninsula fjord systems.

Carbon burial rates are comparable to those found for cores from other continental shelf sites across the Antarctic Peninsula, in the Bransfield Strait (3.1-6.7 g C m^{-2} yr^{-1} – Masqué et al., 2002) and the Gerlache Strait (5-23 g C m^{-2} yr^{-1} – Isla et al., 2002). Burial rates reported for fjord sediments in Andvord Bay (18-24 g m^{-2} yr^{-1} – Eidam et al., 2019) were significantly higher than those reported for nearby Börgen Bay, though this difference is likely due to differing methodologies; Eidam et al. (2019) calculated burial rates based on carbon content of the upper 10cm of sediment, and thus their estimates should be considered closer to deposition rates (in which case, rates closely correspond to those observed at Börgen Bay).

Interestingly, despite remarkably similar burial rates, the carbon burial *efficiencies* were significantly higher at the continental shelf sites (60-80%) (Masqué et al., 2002; Isla et al., 2002) compared with the present study (30-50%), while the lower burial efficiencies in the fjords of this study were balanced out by higher surface depositional rates. Indeed studies of carbon burial in fjords in Patagonia (Sepúlveda et al., 2011) and Svalbard (Kuliński et al., 2014) suggest similar lower burial efficiencies (40-60%). This may indicate that the processes that govern burial efficiency (water oxygen concentration, sedimentation rates, and organic matter content) are different between fjord systems and other marine sites. However, the above processes *should* favour preservation in fjord systems, which typically experience high sedimentation rates and anoxic bottom waters (Bianchi et al., 2016).

It is suggested that this difference in burial efficiency instead arises from the depth of the water column above the seafloor, and the nature of organic matter that is therefore deposited. The cores analysed in this study were taken from relatively shallow water depths, ranging from 80-340m depth, whilst the cores analysed in Masqué et al. (2002) and Isla et al. (2002) were taken on the wider continental shelf from depths closer to 1 km. As organic matter sinks from the surface waters it is respired by microbial communities within the water column, such that the fraction that eventually reaches the seabed is already considerably depleted. As discussed in section 1.2.4, this process results in a form of fractionation, whereby the more labile material is preferentially respired, resulting in comparative

enrichment of refractory material for the organic matter that reaches the seafloor (Burdige, 2007, DeMaster et al., 2021). Organic matter that experiences a higher residence time within the water column (i.e., sinking through greater water depths) would be expected to experience a greater loss of labile material. On the contrary, in shallower water depths, organic matter spends less time in the water column, such that this labile material is preserved and deposited on the sediment surface, resulting in high surface sediment organic content (deposition). However, this labile material is more susceptible to remineralisation within the sediment; thus, while surface sediments in these fjords are high in OC, burial efficiencies are lower, such that the resulting carbon burial rates (sequestration) are more or less equal to those found on the continental shelf.

Alternatively, these differences in burial efficiency may represent higher sulphate concentrations at the fjord sites: the TOC concentration profiles presented in Masqué et al. (2002) exhibit degradation in the upper few centimetres, coincident with the depth of the surface mixed layer, followed by relatively stable levels, indicating a lack of deep sulphate reduction; the cores in the present study, on the other hand, showed continued degradation to considerable depths.

Regardless of causal factor, this discrepancy in burial efficiencies presents significant problems for estimations of fjord carbon burial rates based on surface carbon content. Smith et al. (2015), for example, estimate that 18 Mt of carbon is buried in fjords globally, on the basis of surface sediment OC content and a blanket burial efficiency of 80%, based on observations in Berner (1982). According to the results of the present study, this likely results in an overestimation of 40-50%, at least in the Antarctic Peninsula region. Similarly, estimations of the potential of Antarctic fjords as a negative feedback on climate change (Barnes et al., 2020; Zwerschke et al., 2022) may be exaggerated.

Chapter 6: Conclusions

Mass accumulation rates for all fjords studied were within the range of previously reported MARs from across the AP. No long-term trends in MAR were observed at any of the sites, though at Börgen Bay synchronous peaks in MAR were observed, culminating with the highest MARs circa 1980-1990. This is interpreted to represent the progressive collapse of a floating ice tongue due to the intrusion of CDW, with implications for future glacier stability (Miles et al., 2022). At Marian Cove, the typical proximal-distal gradient in MAR was absent, suggesting a diverse source of sediments, most notably the input from pro-glacial meltwater streams from land-terminating ice.

Surface deposition rates of organic carbon varied, with the highest fjord-wide rates occurring at Börgen Bay, followed by Sheldon Cove and Marian Cove, though anomalously high rates were observed outside the entrance to Marian Cove, attributed to terrestrial organic matter input. Whilst surface organic carbon deposition rates were greater than those reported for other sites across the Antarctic Peninsula continental shelf, burial efficiencies were significantly lower, resulting in similar burial rates of sequestered carbon. This has important implications for estimations of contemporary burial of organic carbon in fjords based on surface organic carbon content, suggesting that current calculations may be erroneously high.

Several limitations of the present study have been identified, and several recommendations are suggested for future research, in the following order of importance:

1. Validating the age-depth models
    - The age-depth models generated for the present study sites should be validated by independent chronostratigraphic markers. This has proved difficult for the Antarctic Peninsula region as bomb-fallout radio-isotope maxima are undetectable, there are no recent dateable tephra horizons (Lee et al., 2007), and there are no readily identifiable abrupt signals of human industry or land-use change.

Future avenues of investigation could relate to the establishment of nearby scientific research bases (the King Sejong Station at Marian Cove and the Rothera Research Station at Ryder Bay), for example with regards to lipid biomarkers (K. Afrifa, *pers. comms*).

2. Improving the accuracy of modern OC burial efficiency and burial rate estimations
    - Estimations of burial efficiency and rates presented here are calculated based on the relationship between modern and aged OC contents. This has certain limitations, notably the degradation of organic matter prior to core retrieval and the possibility of time-varying production rates, both of which could result in overestimations. An alternative approach would be to instead calculate carbon return flux on the basis of porewater measurements of dissolved organic carbon (Koziorowska et al., 2018).

3. Increasing sample size to better assess factors influencing burial efficiency

4. Assessing the relative contribution of terrestrial and marine organic matter
    - Effort should be made to determine the relative contribution of marine and terrestrial organic matter, and the possible presence of petrogenic organic carbon (particularly for core MC0), based on the isotopic composition of fatty acid components (e.g. Berg et al., 2021).

References

Andrews, J.T., Milliman, J.D., Jennings, A.E., Rynes, N. and Dwyer, J., 1994. Sediment thicknesses and Holocene glacial marine sedimentation rates in three East Greenland fjords (ca. 68 N). The Journal of Geology, 102(6), pp.669-683.

Appleby, P.G., 2001. Chronostratigraphic techniques in recent sediments. In Tracking environmental change using lake sediments (pp. 171-203). Springer, Dordrecht.

Appleby, P.G. and Oldfield, F., 1978. The calculation of lead-210 dates assuming a constant rate of supply of unsupported 210Pb to the sediment. Catena, 5(1), pp.1-8.

Appleby, P.G. and Oldfield, F., 1992. Applications of lead-210 to sedimentation studies. In Uranium-series disequilibrium: applications to earth, marine, and environmental sciences. 2. ed.

Appleby, P.G., Nolan, P.J., Gifford, D.W., Godfrey, M.J., Oldfield, F.J.A.N., Anderson, N.J. and Battarbee, R.W., 1986. 210Pb dating by low background gamma counting. Hydrobiologia, 143(1), pp.21-27.

Arendt, K.E., Agersted, M.D., Sejr, M.K. and Juul-Pedersen, T., 2016. Glacial meltwater influences on plankton community structure and the importance of top-down control (of primary production) in a NE Greenland fjord. Estuarine, Coastal and Shelf Science, 183, pp.123-135.

Arndt, S., Jørgensen, B.B., LaRowe, D.E., Middelburg, J.J., Pancost, R.D. and Regnier, P., 2013. Quantifying the degradation of organic matter in marine sediments: A review and synthesis. Earth-science reviews, 123, pp.53-86.

Ashley, G.M. and Smith, N.D., 2000. Marine sedimentation at a calving glacier margin. Geological Society of America Bulletin, 112(5), pp.657-667.

Barnes, D.K. and Souster, T., 2011. Reduced survival of Antarctic benthos linked to climate-induced iceberg scouring. Nature Climate Change, 1(7), pp.365-368.

Barnes, D.K., Sands, C.J., Cook, A., Howard, F., Roman Gonzalez, A., Muñoz–Ramirez, C., Retallick, K., Scourse, J., Van Landeghem, K. and Zwerschke, N.,

2020. Blue carbon gains from glacial retreat along Antarctic fjords: What should we expect?. Global Change Biology, 26(5), pp.2750-2755.

Barnes, D.K., Sands, C.J., Paulsen, M.L., Moreno, B., Moreau, C., Held, C., Downey, R., Bax, N., Stark, J.S. and Zwerschke, N., 2021. Societal importance of Antarctic negative feedbacks on climate change: blue carbon gains from sea ice, ice shelf and glacier losses. The Science of Nature, 108(5), pp.1-14.

Barsanti, M., Garcia-Tenorio, R., Schirone, A., Rozmaric, M., Ruiz-Fernández, A.C., Sanchez-Cabeza, J.A., Delbono, I., Conte, F., Godoy, J.D.O., Heijnis, H. and Eriksson, M., 2020. Challenges and limitations of the 210Pb sediment dating method: Results from an IAEA modelling interlaboratory comparison exercise. Quaternary Geochronology, 59, p.101093.

Batchelor, C.L., Dowdeswell, J.A., Hogan, K.A., Larter, R.D., Parsons, E. and West, O., 2019. Processes and patterns of glacier-influenced sedimentation and recent tidewater glacier dynamics in Darbel Bay, western Antarctic Peninsula. Antarctic Science, 31(4), pp.218-227.

Belcher, A., Henson, S.A., Manno, C., Hill, S.L., Atkinson, A., Thorpe, S.E., Fretwell, P., Ireland, L. and Tarling, G.A., 2019. Krill faecal pellets drive hidden pulses of particulate organic carbon in the marginal ice zone. Nature communications, 10(1), pp.1-8.

Benn, D.I. and Åström, J.A., 2018. Calving glaciers and ice shelves. Advances in Physics: X, 3(1), p.1513819.

Benn, D., & Evans, D.J.A. (2010). Glaciers and Glaciation, 2nd edition (2nd ed.). Routledge. https://doi.org/10.4324/9780203785010

Benn, D.I., Warren, C.R. and Mottram, R.H., 2007. Calving processes and the dynamics of calving glaciers. Earth-Science Reviews, 82(3-4), pp.143-179.

Berg, S., Jivcov, S., Kusch, S., Kuhn, G., White, D., Bohrmann, G., Melles, M. and Rethemeyer, J., 2021. Increased petrogenic and biospheric organic carbon burial in sub-Antarctic fjord sediments in response to recent glacier retreat. Limnology and Oceanography, 66(12), pp.4347-4362.

Betts, J.N. and Holland, H.D., 1991. The oxygen content of ocean bottom waters, the burial efficiency of organic carbon, and the regulation of

atmospheric oxygen. Palaeogeography, Palaeoclimatology, Palaeoecology, 97(1-2), pp.5-18.

Bianchi, T.S., Arndt, S., Austin, W.E., Benn, D.I., Bertrand, S., Cui, X., Faust, J.C., Koziorowska-Makuch, K., Moy, C.M., Savage, C. and Smeaton, C., 2020. Fjords as aquatic critical zones (ACZs). Earth-Science Reviews, 203, p.103145.

Binford, M.W., 1990. Calculation and uncertainty analysis of 210Pb dates for PIRLA project lake sediment cores. Journal of Paleolimnology, 3(3), pp.253-267.

Boldt, K.V., Nittrouer, C.A., Hallet, B., Koppes, M.N., Forrest, B.K., Wellner, J.S. and Anderson, J.B., 2013. Modern rates of glacial sediment accumulation along a 15° S-N transect in fjords from the Antarctic Peninsula to southern Chile. Journal of Geophysical Research: Earth Surface, 118(4), pp.2072-2088.

Bonczyk, M., 2013. A Determination of the Concentration Level of Lead 210 PB Isotope in Solid Samples for the Assessment of Radiation Risk Occuring in Coal Mines. Journal of Sustainable Mining, 12(2), pp.1-7.

Brimhall, G.H., Lewis, C.J., Ague, J.J., Dietrich, W.E., Hampel, J., Teague, T. and Rix, P., 1988. Metal enrichment in bauxites by deposition of chemically mature aeolian dust. Nature, 333(6176), pp.819-824.

Burdige, D.J., 2007. Preservation of organic matter in marine sediments: controls, mechanisms, and an imbalance in sediment organic carbon budgets? Chemical reviews, 107(2), pp.467-485.

Canfield, D.E. and Thamdrup, B.O., 2009. Towards a consistent classification scheme for geochemical environments, or, why we wish the term ‘suboxic’would go away. Geobiology, 7(4), pp.385-392.

Canfield, D.E., 1989. Sulfate reduction and oxic respiration in marine sediments: implications for organic carbon preservation in euxinic environments. Deep Sea Research Part A. Oceanographic Research Papers, 36(1), pp.121-138.

Cape, M.R., Straneo, F., Beaird, N., Bundy, R.M. and Charette, M.A., 2019. Nutrient release to oceans from buoyancy-driven upwelling at Greenland tidewater glaciers. Nature Geoscience, 12(1), pp.34-39.

Clark, J.S. and Patterson, W.A., 1984. Pollen, Pb-210, and opaque spherules; an integrated approach to dating and sedimentation in the intertidal environment. Journal of Sedimentary Research, 54(4), pp.1251-1265.

Clarke, A., Meredith, M.P., Wallace, M.I., Brandon, M.A. and Thomas, D.N., 2008. Seasonal and interannual variability in temperature, chlorophyll and macronutrients in northern Marguerite Bay, Antarctica. Deep Sea Research Part II: Topical Studies in Oceanography, 55(18-19), pp.1988-2006.

Cloern, J.E., 1987. Turbidity as a control on phytoplankton biomass and productivity in estuaries. Continental shelf research, 7(11-12), pp.1367-1381.

Cook, A.J. and Vaughan, D.G., 2010. Overview of areal changes of the ice shelves on the Antarctic Peninsula over the past 50 years. The cryosphere, 4(1), pp.77-98.

Cook, A.J., Fox, A.J., Vaughan, D.G. and Ferrigno, J.G., 2005. Retreating glacier fronts on the Antarctic Peninsula over the past half-century. Science, 308(5721), pp.541-544.

Cook, A.J., Holland, P.R., Meredith, M.P., Murray, T., Luckman, A. and Vaughan, D.G., 2016. Ocean forcing of glacier retreat in the western Antarctic Peninsula. Science, 353(6296), pp.283-286.

Cook, A.J., Vaughan, D.G., Luckman, A.J. and Murray, T., 2014. A new Antarctic Peninsula glacier basin inventory and observed area changes since the 1940s. Antarctic Science, 26(6), pp.614-624.

Costa, R.R., Mendes, C.R.B., Tavano, V.M., Dotto, T.S., Kerr, R., Monteiro, T., Odebrecht, C. and Secchi, E.R., 2020. Dynamics of an intense diatom bloom in the Northern Antarctic Peninsula, February 2016. Limnology and Oceanography, 65(9), pp.2056-2075.

Cowan, E.A., Cai, J., Powell, R.D., Clark, J.D. and Pitcher, J.N., 1997. Temperate glacimarine varves: an example from Disenchantment Bay, southern Alaska. Journal of Sedimentary Research, 67(3).

Cowan, E.A., Seramur, K.C., Powell, R.D., Willems, B.A., Gulick, S.P. and Jaeger, J.M., 2010. Fjords as temporary sediment traps: History of glacial erosion and deposition in Muir Inlet, Glacier Bay National Park, southeastern Alaska. Bulletin, 122(7-8), pp.1067-1080.

Crozaz, G., Picciotto, E. and De Breuck, W., 1964. Antarctic snow chronology with Pb210. Journal of Geophysical Research, 69(12), pp.2597-2604.

Cui, X., Bianchi, T.S., Savage, C. and Smith, R.W., 2016. Organic carbon burial in fjords: Terrestrial versus marine inputs. Earth and Planetary Science Letters, 451, pp.41-50.

Davies, B.J., Carrivick, J.L., Glasser, N.F., Hambrey, M.J. and Smellie, J.L., 2012. Variable glacier response to atmospheric warming, northern Antarctic Peninsula, 1988–2009. The Cryosphere, 6(5), pp.1031-1048.

DeMaster, D.J., Taylor, R.S., Smith, C.R., Isla, E. and Thomas, C.J., 2021. Using radiocarbon to assess the abundance, distribution, and nature of labile organic carbon in marine sediments. Global Biogeochemical Cycles, 35(6), p.e2020GB006676.

Domack, E.W. and Ishman, S., 1993. Oceanographic and physiographic controls on modern sedimentation within Antarctic fjords. Geological Society of America Bulletin, 105(9), pp.1175-1189.

Domack, E.W. and Williams, C., 1990. Fine structure and suspended sediment transport in three Antarctic fjords. Contributions to Antarctic Research I, 50, pp.71-89.

Ducklow, H.W., Baker, K., Martinson, D.G., Quetin, L.B., Ross, R.M., Smith, R.C., Stammerjohn, S.E., Vernet, M. and Fraser, W., 2007. Marine pelagic ecosystems: the west Antarctic Peninsula. Philosophical Transactions of the Royal Society B: Biological Sciences, 362(1477), pp.67-94.

Duprat, L.P., Bigg, G.R. and Wilton, D.J., 2016. Enhanced Southern Ocean marine productivity due to fertilization by giant icebergs. Nature Geoscience, 9(3), pp.219-221.

Egger, M., Riedinger, N., Mogollón, J.M. and Jørgensen, B.B., 2018. Global diffusive fluxes of methane in marine sediments. Nature Geoscience, 11(6), pp.421-425.

Eidam, E.F., Nittrouer, C.A., Lundesgaard, Ø., Homolka, K.K. and Smith, C.R., 2019. Variability of sediment accumulation rates in an Antarctic Fjord. Geophysical Research Letters, 46(22), pp.13271-13280.

Eilertsen, H.C. and Degerlund, M., 2010. Phytoplankton and light during the northern high-latitude winter. Journal of plankton research, 32(6), pp.899-912.

Farmer, J.G., Graham, M.C., Yafa, C., Cloy, J.M., Freeman, A.J. and MacKenzie, A.B., 2006. Use of 206Pb/207Pb ratios to investigate the surface integrity of peat cores used to study the recent depositional history and geochemical behaviour of inorganic elements in peat bogs. Global and Planetary Change, 53(4), pp.240-248.

Faust, J.C., Tessin, A., Fisher, B.J., Zindorf, M., Papadaki, S., Hendry, K.R., Doyle, K.A. and März, C., 2021. Millennial scale persistence of organic carbon bound to iron in Arctic marine sediments. Nature communications, 12(1), pp.1-9.

Favier, V., Krinner, G., Amory, C., Gallée, H., Beaumet, J. and Agosta, C., 2017. Antarctica-regional climate and surface mass budget. Current Climate Change Reports, 3(4), pp.303-315.

Fer, I. and Widell, K., 2007. Early spring turbulent mixing in an ice-covered Arctic fjord during transition to melting. Continental Shelf Research, 27(15), pp.1980-1999.

Friedl, P., Seehaus, T.C., Wendt, A., Braun, M.H. and Höppner, K., 2018. Recent dynamic changes on Fleming glacier after the disintegration of Wordie ice shelf, Antarctic peninsula. The Cryosphere, 12(4), pp.1347-1365.

Froelich, P., Klinkhammer, G.P., Bender, M.L., Luedtke, N.A., Heath, G.R., Cullen, D., Dauphin, P., Hammond, D., Hartman, B. and Maynard, V., 1979. Early oxidation of organic matter in pelagic sediments of the eastern equatorial Atlantic: suboxic diagenesis. Geochimica et cosmochimica acta, 43(7), pp.1075-1090.

Goldberg, E.D., 1963. Geochronology with 210Pb. Radioactive dating, pp.121-131.

Gomez-Fell, R., Rack, W., Purdie, H. and Marsh, O., 2022. Parker Ice Tongue Collapse, Antarctica, Triggered by Loss of Stabilizing Land-Fast Sea Ice. Geophysical Research Letters, 49(1), p.e2021GL096156.

Gordon, A.L. and Nowlin Jr, W.D., 1978. The basin waters of the Bransfield Strait. Journal of Physical Oceanography, 8(2), pp.258-264.

Grange, L.J. and Smith, C.R., 2013. Megafaunal communities in rapidly warming fjords along the West Antarctic Peninsula: hotspots of abundance and beta diversity. PloS one, 8(12), p.e77917.

Gray, A., Krolikowski, M., Fretwell, P., Convey, P., Peck, L.S., Mendelova, M., Smith, A.G. and Davey, M.P., 2020. Remote sensing reveals Antarctic green snow algae as important terrestrial carbon sink. Nature Communications, 11(1), pp.1-9.

Gustafsson, K.E. and Bendtsen, J., 2007. Elucidating the dynamics and mixing agents of a shallow fjord through age tracer modelling. Estuarine, Coastal and Shelf Science, 74(4), pp.641-654.

Hartnett, H.E., Keil, R.G., Hedges, J.I. and Devol, A.H., 1998. Influence of oxygen exposure time on organic carbon preservation in continental margin sediments. Nature, 391(6667), pp.572-575.

Hegseth, E.N. and Tverberg, V., 2013. Effect of Atlantic water inflow on timing of the phytoplankton spring bloom in a high Arctic fjord (Kongsfjorden, Svalbard). Journal of Marine Systems, 113, pp.94-105.

Henley, S.F., Cavan, E.L., Fawcett, S.E., Kerr, R., Monteiro, T., Sherrell, R.M., Bowie, A.R., Boyd, P.W., Barnes, D.K., Schloss, I.R. and Marshall, T., 2020. Changing biogeochemistry of the Southern Ocean and its ecosystem implications. Frontiers in marine science, 7, p.581.

Henrichs, S.M. and Reeburgh, W.S., 1987. Anaerobic mineralization of marine sediment organic matter: rates and the role of anaerobic processes in the oceanic carbon economy. Geomicrobiology Journal, 5(3-4), pp.191-237.

Henrichs, S.M. and Reeburgh, W.S., 1987. Anaerobic mineralization of marine sediment organic matter: rates and the role of anaerobic processes in the oceanic carbon economy. Geomicrobiology Journal, 5(3-4), pp.191-237.

Hock, R., De Woul, M., Radić, V. and Dyurgerov, M., 2009. Mountain glaciers and ice caps around Antarctica make a large sea-level rise contribution. Geophysical Research Letters, 36(7).

Hogan, K.A., Jakobsson, M., Mayer, L., Reilly, B.T., Jennings, A.E., Stoner, J.S., Nielsen, T., Andresen, K.J., Nørmark, E., Heirman, K.A. and Kamla, E., 2020. Glacial sedimentation, fluxes and erosion rates associated with ice retreat

in Petermann Fjord and Nares Strait, north-west Greenland. The Cryosphere, 14(1), pp.261-286.

Howe, J.A., Austin, W.E., Forwick, M., Paetzel, M., Harland, R.E.X. and Cage, A.G., 2010. Fjord systems and archives: a review. Geological Society, London, Special Publications, 344(1), pp.5-15.

Huh, C.A. and Su, C.C., 1999. Sedimentation dynamics in the East China Sea elucidated from 210Pb, 137Cs and 239,240 Pu. Marine Geology, 160(1-2), pp.183-196.

Humphrey, N.F. and Raymond, C.F., 1994. Hydrology, erosion and sediment production in a surging glacier: Variegated Glacier, Alaska, 1982–83. Journal of Glaciology, 40(136), pp.539-552.

Hur, S.D., Lee, J.I., Hwang, J. and Choe, M.Y., 2001. K-Ar age and geochemistry of hydrothermal alteration in the Barton Peninsula, King George Island, Antarctica. Ocean and Polar Research, 23(1), pp.11-21.

Isla, E. and DeMaster, D.J., 2021. Biogenic matter content in marine sediments in the vicinity of the Antarctic Peninsula: Recent sedimentary conditions under a diverse environment of production, transport, selective preservation and accumulation. Geochimica et Cosmochimica Acta, 304, pp.50-67.

Isla, E., Masqué, P., Palanques, A., Guillén, J., Puig, P. and Sanchez-Cabeza, J.A., 2004. Sedimentation of biogenic constituents during the last century in western Bransfield and Gerlache Straits, Antarctica: a relation to currents, primary production, and sea floor relief. Marine Geology, 209(1-4), pp.265-277.

Isla, E., Masqué, P., Palanques, A., Sanchez-Cabeza, J.A., Bruach, J.M., Guillén, J. and Puig, P., 2002. Sediment accumulation rates and carbon burial in the bottom sediment in a high-productivity area: Gerlache Strait (Antarctica). Deep Sea Research Part II: Topical Studies in Oceanography, 49(16), pp.3275-3287.

Jackson, R.H., Straneo, F. and Sutherland, D.A., 2014. Externally forced fluctuations in ocean temperature at Greenland glaciers in non-summer months. Nature Geoscience, 7(7), pp.503-508.

Jaeger, J.M. and Nittrouer, C.A., 1999. Sediment deposition in an Alaskan fjord; controls on the formation and preservation of sedimentary structures in Icy Bay. Journal of Sedimentary Research, 69(5), pp.1011-1026.

Jørgensen, B.B. and Kasten, S., 2006. Sulfur cycling and methane oxidation. In Marine geochemistry (pp. 271-309). Springer, Berlin, Heidelberg.

Keil, R., 2015. Hoard of fjord carbon. Nature Geoscience, 8(6), pp.426-427.

Kirchner, G. and Ehlers, H., 1998. Sediment geochronology in changing coastal environments: potentials and limitations of the 137Cs and 210Pb methods. Journal of Coastal Research, pp.483-492.

Kirchner, G., 2011. 210Pb as a tool for establishing sediment chronologies: examples of potentials and limitations of conventional dating models. Journal of Environmental Radioactivity, 102(5), pp.490-494.

Koide, M., Soutar, A. and Goldberg, E.D., 1972. Marine geochronology with210Pb. Earth and Planetary Science Letters, 14(3), pp.442-446.

Koppes, M. and Hallet, B., 2006. Erosion rates during rapid deglaciation in Icy Bay, Alaska. Journal of Geophysical Research: Earth Surface, 111(F2).

Koppes, M., Hallet, B., Rignot, E., Mouginot, J., Wellner, J.S. and Boldt, K., 2015. Observed latitudinal variations in erosion as a function of glacier dynamics. Nature, 526(7571), pp.100-103.

Koziorowska, K., Kuliński, K. and Pempkowiak, J., 2018. Comparison of the burial rate estimation methods of organic and inorganic carbon and quantification of carbon burial in two high Arctic fjords. Oceanologia, 60(3), pp.405-418.

Kuliński, K., Kędra, M., Legeżyńska, J., Gluchowska, M. and Zaborska, A., 2014. Particulate organic matter sinks and sources in high Arctic fjord. Journal of Marine Systems, 139, pp.27-37.

Lalonde, K., Mucci, A., Ouellet, A. and Gélinas, Y., 2012. Preservation of organic matter in sediments promoted by iron. Nature, 483(7388), pp.198-200.

Lamarche-Gagnon, G., Wadham, J.L., Sherwood Lollar, B., Arndt, S., Fietzek, P., Beaton, A.D., Tedstone, A.J., Telling, J., Bagshaw, E.A., Hawkings, J.R. and Kohler, T.J., 2019. Greenland melt drives continuous export of methane from the ice-sheet bed. Nature, 565(7737), pp.73-77.

Laufkötter, C., Stern, A.A., John, J.G., Stock, C.A. and Dunne, J.P., 2018. Glacial iron sources stimulate the southern ocean carbon cycle. Geophysical Research Letters, 45(24), pp.13-377.

Lee, Y.I., Lim, H.S., Yoon, H.I. and Tatur, A., 2007. Characteristics of tephra in Holocene lake sediments on King George Island, West Antarctica: implications for deglaciation and paleoenvironment. Quaternary Science Reviews, 26(25-28), pp.3167-3178.

Legrand, M., Preunkert, S., Jourdain, B., Guilhermet, J., Alekhina, I. and Petit, J.R., 2013. Water-soluble organic carbon in snow and ice deposited at Alpine, Greenland, and Antarctic sites: a critical review of available data and their atmospheric relevance. Climate of the Past, 9(5), pp.2195-2211.

Llanillo, P.J., Aiken, C.M., Cordero, R.R., Damiani, A., Sepúlveda, E. and Fernández-Gómez, B., 2019. Oceanographic variability induced by tides, the intraseasonal cycle and warm subsurface water intrusions in Maxwell Bay, King George Island (West-Antarctica). Scientific reports, 9(1), pp.1-17.

Lundesgaard, Ø., Winsor, P., Truffer, M., Merrifield, M., Powell, B., Statscewich, H., Eidam, E. and Smith, C.R., 2020. Hydrography and energetics of a cold subpolar fjord: Andvord Bay, western Antarctic Peninsula. Progress in Oceanography, 181, p.102224.

MacKenzie, A.B., Hardie, S.M.L., Farmer, J.G., Eades, L.J. and Pulford, I.D., 2011. Analytical and sampling constraints in 210Pb dating. Science of the Total Environment, 409(7), pp.1298-1304.

Masqué, P., Isla, E., Sanchez-Cabeza, J.A., Palanques, A., Bruach, J.M., Puig, P. and Guillén, J., 2002. Sediment accumulation rates and carbon fluxes to bottom sediments at the Western Bransfield Strait (Antarctica). Deep Sea Research Part II: Topical Studies in Oceanography, 49(4-5), pp.921-933.

Meredith, M.P. and King, J.C., 2005. Rapid climate change in the ocean west of the Antarctic Peninsula during the second half of the 20th century. Geophysical Research Letters, 32(19).

Meredith, M.P., Inall, M.E., Brearley, J.A., Ehmen, T., Sheen, K., Munday, D., Cook, A., Retallick, K., Van Landeghem, K., Gerrish, L. and Annett, A., 2022.

Internal tsunamigenesis and ocean mixing driven by glacier calving in Antarctica. Science advances, 8(47), p.eadd0720.

Miles, B.W., Stokes, C.R., Jamieson, S.S., Jordan, J.R., Gudmundsson, G.H. and Jenkins, A., 2022. High spatial and temporal variability in Antarctic ice discharge linked to ice shelf buttressing and bed geometry. Scientific reports, 12(1), pp.1-14.

Milliken, K.T., Anderson, J.B., Wellner, J.S., Bohaty, S.M. and Manley, P.L., 2009. High-resolution holocene climate record from maxwell bay, south shetland islands, antarctica. Geological Society of America Bulletin, 121(11-12), pp.1711-1725.

Moffat, C. and Meredith, M., 2018. Shelf–ocean exchange and hydrography west of the Antarctic Peninsula: a review. Philosophical Transactions of the Royal Society A: Mathematical, Physical and Engineering Sciences, 376(2122), p.20170164.

Monien, D., Monien, P., Brünjes, R., Widmer, T., Kappenberg, A., Busso, A.A.S., Schnetger, B. and Brumsack, H.J., 2017. Meltwater as a source of potentially bioavailable iron to Antarctica waters. Antarctic Science, 29(3), pp.277-291.

Monien, P., Schnetger, B., Brumsack, H.J., Hass, H.C. and Kuhn, G., 2011. A geochemical record of late Holocene palaeoenvironmental changes at King George Island (maritime Antarctica). Antarctic Science, 23(3), pp.255-267.

Moore, C.M., Mills, M.M., Arrigo, K.R., Berman-Frank, I., Bopp, L., Boyd, P.W., Galbraith, E.D., Geider, R.J., Guieu, C., Jaccard, S.L. and Jickells, T.D., 2013. Processes and patterns of oceanic nutrient limitation. Nature geoscience, 6(9), pp.701-710.

Moreau, S., Mostajir, B., Bélanger, S., Schloss, I.R., Vancoppenolle, M., Demers, S. and Ferreyra, G.A., 2015. Climate change enhances primary production in the western Antarctic Peninsula. Global Change Biology, 21(6), pp.2191-2205.

Mortensen, J., Lennert, K., Bendtsen, J. and Rysgaard, S., 2011. Heat sources for glacial melt in a sub-Arctic fjord (Godthåbsfjord) in contact with the Greenland Ice Sheet. Journal of Geophysical Research: Oceans, 116(C1).

Mugford, R.I. and Dowdeswell, J.A., 2011. Modeling glacial meltwater plume dynamics and sedimentation in high-latitude fjords. Journal of Geophysical Research: Earth Surface, 116(F1).

Mulder, T. and Syvitski, J.P., 1995. Turbidity currents generated at river mouths during exceptional discharges to the world oceans. The Journal of Geology, 103(3), pp.285-299.

Müller, P.J. and Suess, E., 1979. Productivity, sedimentation rate, and sedimentary organic matter in the oceans—I. Organic carbon preservation. Deep Sea Research Part A. Oceanographic Research Papers, 26(12), pp.1347-1362.

Munoz, Y.P. and Wellner, J.S., 2016. Local controls on sediment accumulation and distribution in a fjord in the West Antarctic Peninsula: implications for palaeoenvironmental interpretations. Polar Research, 35(1), p.25284.

Munoz, Y.P. and Wellner, J.S., 2018. Seafloor geomorphology of western Antarctic Peninsula bays: a signature of ice flow behaviour. The Cryosphere, 12(1), pp.205-225.

Nelleman, C., Corcoran, E., Duarte, C.M., Valdes, L., DeYoung, C., Fonseca, L. and Grimsditch, G., 2009. Blue carbon: The role of healthy oceans in binding carbon. UNEP/FAO/UNESCO/IUCN/CSIC.

Olid, C., Garcia-Orellana, J., Martínez-Cortizas, A., Masqué, P., Peiteado, E. and Sanchez-Cabeza, J.A., 2008. Role of surface vegetation in 210Pb-dating of peat cores. Environmental science & technology, 42(23), pp.8858-8864.

Oliva, M., Navarro, F., Hrbáček, F., Hernandéz, A., Nývlt, D., Pereira, P., Ruiz-Fernandéz, J. and Trigo, R., 2017. Recent regional climate cooling on the Antarctic Peninsula and associated impacts on the cryosphere. Science of the Total Environment, 580, pp.210-223.

Palanques, A., Isla, E., Masqué, P., Puig, P., Sánchez-Cabeza, J.A., Gili, J.M. and Guillén, J., 2002. Downward particle fluxes and sediment accumulation rates in the western Bransfield Strait: Implications of lateral transport for carbon cycle studies in Antarctic marginal seas. Journal of Marine Research, 60(2), pp.347-365.

Pennington, W., Tutin, T.G., Cambray, R.S. and Fisher, E.M., 1973. Observations on lake sediments using fallout 137Cs as a tracer. Nature, 242(5396), pp.324-326.

Pritchard, H., Ligtenberg, S.R., Fricker, H.A., Vaughan, D.G., van den Broeke, M.R. and Padman, L., 2012. Antarctic ice-sheet loss driven by basal melting of ice shelves. Nature, 484(7395), pp.502-505.

Retallick, K., Van Landeghem, K., Fremand, A., Howard, F., Sands, C., Roman-Gonzalez, A., Barnes, D., Jenkins, S., 2021. Seafloor bathymetry of Sheldon Cove, Börgen Bay and Marian Cove, merged and gridded from EM122 multibeam echosounder data collected for the project NE/P003087/1. Polar Data Centre, Natural Environment Research Council, UK Research & Innovation.

Rignot, E. and Jacobs, S.S., 2002. Rapid bottom melting widespread near Antarctic ice sheet grounding lines. Science, 296(5575), pp.2020-2023.

Robbins, J.A. and Herche, L.R., 1993. Models and uncertainty in 210Pb dating of sediments. Internationale Vereinigung für theoretische und angewandte Limnologie: Verhandlungen, 25(1), pp.217-222.

Rodrigo, C. and Herbstaedt, R., 2021. Submarine landforms and seismic facies in Börgen Bay, Anvers Island: Imprints of the past glacial behaviour and climate influence in the Western Antarctic Peninsula. Polar Science, 29, p.100695.

Rozema, P.D., Kulk, G., Veldhuis, M.P., Buma, A.G., Meredith, M.P. and van de Poll, W.H., 2017. Assessing drivers of coastal primary production in northern Marguerite Bay, Antarctica. Frontiers in Marine Science, 4, p.184.

Ruiz-Fernández, A.C., Sánchez-Cabeza, J.A., Bojorquez-Sanchez, S., Bojorquez-Leyva, H., Perez-Bernal, L.H., Mellado-Vazquez, P.G., Alonso-Hernández, C., Diaz-Ascencio, M., Gerardo-Abaya, J., Quejido Cabezas, J. and Sericano, J.L., 2009. Heavy metals and sediment fluxes in Coatzacoalcos River estuary: A history of land use changes. Geochimica et Cosmochimica Acta Supplement, 73, p.A1133.

Rundle, A.S., 1973. Glaciology of the Marr Ice Piedmont, Anvers Island, Antarctica. Research Foundation and the Institute of Polar Studies, The Ohio State University.

Rysgaard, S., Nielsen, T.G. and Hansen, B.W., 1999. Seasonal variation in nutrients, pelagic primary production and grazing in a high-Arctic coastal marine ecosystem, Young Sound, Northeast Greenland. Marine Ecology Progress Series, 179, pp.13-25.

Sabatier, P., Moernaut, J., Bertrand, S., Van Daele, M., Kremer, K., Chaumillon, E. and Arnaud, F., 2022. A review of event deposits in lake sediments. Quaternary, 5(3), p.34.

Sahade, R., Lagger, C., Torre, L., Momo, F., Monien, P., Schloss, I., Barnes, D.K., Servetto, N., Tarantelli, S., Tatián, M. and Zamboni, N., 2015. Climate change and glacier retreat drive shifts in an Antarctic benthic ecosystem. Science Advances, 1(10), p.e1500050.

Sanchez-Cabeza, J.A. and Ruiz-Fernández, A.C., 2012. 210Pb sediment radiochronology: an integrated formulation and classification of dating models. Geochimica et Cosmochimica Acta, 82, pp.183-200.

Sanchez-Cabeza, J.A., Ruiz-Fernández, A.C., Ontiveros-Cuadras, J.F., Bernal, L.H.P. and Olid, C., 2014. Monte Carlo uncertainty calculation of 210Pb chronologies and accumulation rates of sediments and peat bogs. Quaternary Geochronology, 23, pp.80-93.

Schirone, A., Rožmarić, M., Barsanti, M., Raiteri, G., Sanchez-Cabeza, J.A., García-Tenorio, R. and Osvath, I., 2022. Assessment of measurement accuracy in 210Pb dating sediment methods. Quaternary Geochronology, 69, p.101255.

Schmidtko, S., Heywood, K.J., Thompson, A.F. and Aoki, S., 2014. Multidecadal warming of Antarctic waters. Science, 346(6214), pp.1227-1231.

Schofield, O., Brown, M., Kohut, J., Nardelli, S., Saba, G., Waite, N. and Ducklow, H., 2018. Changes in the upper ocean mixed layer and phytoplankton productivity along the West Antarctic Peninsula. Philosophical Transactions of the Royal Society A: Mathematical, Physical and Engineering Sciences, 376(2122), p.20170173.

Scourse, J.D., Wanamaker, A.D., Weidman, C., Heinemeier, J., Reimer, P.J., Butler, P.G., Witbaard, R. and Richardson, C.A., 2012. The marine radiocarbon bomb pulse across the temperate North Atlantic: A compilation of Δ14C time

histories from Arctica islandica growth increments. Radiocarbon, 54(2), pp.165-186.

Sepúlveda, J., Pantoja, S. and Hughen, K.A., 2011. Sources and distribution of organic matter in northern Patagonia fjords, Chile (~ 44–47 S): a multi-tracer approach for carbon cycling assessment. Continental Shelf Research, 31(3-4), pp.315-329.

Silva, A.B., Arigony-Neto, J., Braun, M.H., Espinoza, J.M.A., Costi, J. and Jaña, R., 2020. Spatial and temporal analysis of changes in the glaciers of the Antarctic Peninsula. Global and Planetary Change, 184, p.103079.

Smith, J.A., Andersen, T.J., Shortt, M., Gaffney, A.M., Truffer, M., Stanton, T.P., Bindschadler, R., Dutrieux, P., Jenkins, A., Hillenbrand, C.D. and Ehrmann, W., 2017. Sub-ice-shelf sediments record history of twentieth-century retreat of Pine Island Glacier. Nature, 541(7635), pp.77-80.

Smith, J.N., 2001. Why should we believe 210Pb sediment geochronologies?. Journal of Environmental Radioactivity, 55(2), pp.121-123.

Smith, R.W., Bianchi, T.S. and Savage, C., 2010. Comparison of lignin phenols and branched/isoprenoid tetraethers (BIT index) as indices of terrestrial organic matter in Doubtful Sound, Fiordland, New Zealand. Organic Geochemistry, 41(3), pp.281-290.

Smith, R.W., Bianchi, T.S., Allison, M., Savage, C. and Galy, V., 2015. High rates of organic carbon burial in fjord sediments globally. Nature Geoscience, 8(6), pp.450-453.

Stibal, M., Gözdereliler, E., Cameron, K.A., Box, J.E., Stevens, I.T., Gokul, J.K., Schostag, M., Zarsky, J.D., Edwards, A., Irvine-Fynn, T.D. and Jacobsen, C.S., 2015. Microbial abundance in surface ice on the Greenland Ice Sheet. Frontiers in microbiology, 6, p.225.

Syvitski, J.P., Asprey, K.W., Clattenburg, D.A. and Hodge, G.D., 1985. The prodelta environment of a fjord: suspended particle dynamics. Sedimentology, 32(1), pp.83-107.

Toth, D.J. and Lerman, A.B.R.A.H.A.M., 1977. Organic matter reactivity and sedimentation rates in the ocean. American Journal of Science, 277(4), pp.465-485.

Truffer, M. and Motyka, R.J., 2016. Where glaciers meet water: Subaqueous melt and its relevance to glaciers in various settings. Reviews of Geophysics, 54(1), pp.220-239.

Turner, J., Barrand, N.E., Bracegirdle, T.J., Convey, P., Hodgson, D.A., Jarvis, M., Jenkins, A., Marshall, G., Meredith, M.P., Roscoe, H. and Shanklin, J., 2014. Antarctic climate change and the environment: an update. Polar record, 50(3), pp.237-259.

Turner, J., Colwell, S.R., Marshall, G.J., Lachlan-Cope, T.A., Carleton, A.M., Jones, P.D., Lagun, V., Reid, P.A. and Iagovkina, S., 2005. Antarctic climate change during the last 50 years. International journal of Climatology, 25(3), pp.279-294.

Turner, J., Lu, H., White, I., King, J.C., Phillips, T., Hosking, J.S., Bracegirdle, T.J., Marshall, G.J., Mulvaney, R. and Deb, P., 2016. Absence of 21st century warming on Antarctic Peninsula consistent with natural variability. Nature, 535(7612), pp.411-415.

Tyson, R.V., 2005. The" productivity versus preservation" controversy: cause, flaws, and resolution. Special Publication-SEPM, 82, p.17.

Van der Merwe, P., Wuttig, K., Holmes, T., Trull, T.W., Chase, Z., Townsend, A.T., Goemann, K. and Bowie, A.R., 2019. High lability Fe particles sourced from glacial erosion can meet previously unaccounted biological demand: Heard Island, Southern Ocean. Frontiers in Marine Science, 6, p.332.

Vermassen, F., Wangner, D.J., Dyke, L.M., Schmidt, S., Cordua, A.E., Kjær, K.H., Haubner, K. and Andresen, C.S., 2019. Evaluating ice-rafted debris as a proxy for glacier calving in Upernavik Isfjord, NW Greenland. Journal of Quaternary Science, 34(3), pp.258-267.

Walker, M., 2005. Quaternary dating methods. John Wiley and Sons.

Webb, A.L., Hughes, K.A., Grand, M.M., Lohan, M.C. and Peck, L.S., 2020. Sources of elevated heavy metal concentrations in sediments and benthic marine invertebrates of the western Antarctic Peninsula. Science of the Total Environment, 698, p.134268.

Weston, K., Jickells, T.D., Carson, D.S., Clarke, A., Meredith, M.P., Brandon, M.A., Wallace, M.I., Ussher, S.J. and Hendry, K.R., 2013. Primary production

export flux in Marguerite Bay (Antarctic Peninsula): Linking upper water-column production to sediment trap flux. Deep Sea Research Part I: Oceanographic Research Papers, 75, pp.52-66.

Yallop, M.L., Anesio, A.M., Perkins, R.G., Cook, J., Telling, J., Fagan, D., MacFarlane, J., Stibal, M., Barker, G., Bellas, C. and Hodson, A., 2012. Photophysiology and albedo-changing potential of the ice algal community on the surface of the Greenland ice sheet. The ISME journal, 6(12), pp.2302-2313.

Yang, J.S., 1990. Nutrients, Chlorophyll-a and Primary Productivity in Maxwell Bay, King George Island, Antarctica.

Yoo, K.C., Lee, M.K., Yoon, H.I., Lee, Y.I. and Kang, C.Y., 2015. Hydrography of Marian Cove, King George Island, West Antarctica: implications for ice-proximal sedimentation during summer. Antarctic Science, 27(2), pp.185-196.

Yoo, K.C., Yoon, H.I., Kang, C.Y., Kim, B.K. and Oh, J.K., 2000. Water column structure and dispersal pattern of suspended particulate matter (SPM) in a floating ice-dominated fjord, Marian Cove, Antarctica during austral summer. The Sea: JOURNAL OF THE KOREAN SOCIETY OF OCEANOGRAPHY, 5(4), pp.295-304.

Yoo, K.C., Yoon, H.I., Oh, J.K., Kim, Y.D. and Kang, C.Y., 1999. Water column properties and dispersal pattern of suspended particulate matter (SPM) of Marian Cove during austral summer, King George Island, West Antarctica. The Sea: JOURNAL OF THE KOREAN SOCIETY OF OCEANOGRAPHY, 4(4), pp.266-274.

Yoon, H.I., Han, M.W., Park, B.K., Oh, J.K. and Chang, S.K., 1997. Glaciomarine sedimentation and palaeo-glacial setting of Maxwell Bay and its tributary embayment, Marian Cove, South Shetland Islands, West Antarctica. Marine Geology, 140(3-4), pp.265-282.

Yoon, H.I., Park, B.K., Domack, E.W. and Kim, Y., 1998. Distribution and dispersal pattern of suspended particulate matter in Maxwell Bay and its tributary, Marian Cove, in the South Shetland Islands, West Antarctica. Marine Geology, 152(4), pp.261-275.

Zaborska, A., Carroll, J., Papucci, C. and Pempkowiak, J., 2007. Intercomparison of alpha and gamma spectrometry techniques used in 210Pb geochronology. Journal of environmental radioactivity, 93(1), pp.38-50.

Zaborska, A., Włodarska-Kowalczuk, M., Legeżyńska, J., Jankowska, E., Winogradow, A. and Deja, K., 2018. Sedimentary organic matter sources, benthic consumption and burial in west Spitsbergen fjords–Signs of maturing of Arctic fjordic systems?. Journal of Marine Systems, 180, pp.112-123.

Ziegler, A.F., Cape, M., Lundesgaard, Ø. and Smith, C.R., 2020. Intense deposition and rapid processing of seafloor phytodetritus in a glaciomarine fjord, Andvord Bay (Antarctica). Progress in Oceanography, 187, p.102413.

Ziegler, A.F., Smith, C.R., Edwards, K.F. and Vernet, M., 2017. Glacial dropstones: islands enhancing seafloor species richness of benthic megafauna in West Antarctic Peninsula fjords. Marine Ecology Progress Series, 583, pp.1-14.

Zwerschke, N., Sands, C.J., Roman-Gonzalez, A., Barnes, D.K., Guzzi, A., Jenkins, S., Muñoz-Ramírez, C. and Scourse, J., 2022. Quantification of blue carbon pathways contributing to negative feedback on climate change following glacier retreat in West Antarctic fjords. Global Change Biology, 28(1), pp.8-20.

Appendix

Table A1: Isotope data used to construct age-depth models and calculate mass accumulation rates. Sample surface area = 63.62 cm^2. Uncertainty = 1σ.

Core	Sample depth	Sample thickness	Dry bulk density	$^{210}Pb_{total}$	±	^{214}Pb	±
	cm	cm	g cm^{-3}	Bq kg^{-1}		Bq kg^{-1}	
MC0	0.5	0.5	0.77	270	23	13	1
MC0	1	0.5	0.63	330	25	14	2
MC0	2	0.5	0.77	295	20	14	1
MC0	3	1	0.74	308	20	12	1
MC0	4	1	0.85	299	14	12	1
MC0	6	1	0.75	310	21	13	1
MC0	8	1	0.80	278	19	12	1
MC0	10	1	1.07	263	18	12	1
MC0	12	1	0.85	214	23	12	1
MC0	14	1	0.87	196	14	12	1
MC0	16	1	0.87	172	13	11	1
MC0	18	1	0.91	149	11	11	1
MC0	20	1	0.79	146	11	10	1
MC0	22	1	0.81	114	9	11	1
MC0	24	1	0.83	132	11	12	1
MC2	1	1	0.58	144	7	42	2
MC2	2	1	0.64	152	9	38	1
MC2	3	1	0.68	146	9	36	2
MC2	4	1	0.76	104	7	36	1
MC2	6	1	0.82	86	5	37	2
MC2	8	1	0.87	52	10	34	2
MC2	10	1	0.84	66	6	43	2
MC2	12	1	0.86	56	6	38	2
MC2	14	1	0.94	41	6	38	3
MC2	16	1	0.90	45	7	40	2
MC2	18	1	0.99	51	4	38	2
MC2	20	1	0.99	44	6	38	2
MC2	22	1	1.05	43	5	38	2
MC2	24	1	1.01	45	5	38	2
MC4	1	1	0.57	102	8	31	2
MC4	2	1	0.68	96	8	26	2
MC4	3	1	0.65	104	7	28	2
MC4	4	1	0.68	111	8	27	2
MC4	6	1	1.61	80	5	28	2
MC4	8	1	0.97	-	-	27	1
MC4	10	1	1.00	63	5	30	2
MC4	12	1	1.01	51	5	32	2
BB0	0.5	0.5	0.81	394	25	15	1
BB0	1	0.5	0.71	368	24	16	1
BB0	2	0.5	0.80	387	25	18	1
BB0	3	1	0.97	191	12	15	1

BB0	4	1	1.14	177	12	14	1
BB0	6	1	1.14	133	8	18	1
BB0	8	1	1.19	70	5	16	1
BB0	10	1	1.63	58	5	10	1
BB0	12	1	1.19	65	6	15	1
BB0	14	1	1.19	50	6	16	1
BB0	16	1	0.95	54	6	17	1
BB0	18	1	1.22	48	6	16	1
BB0	20	1	1.21	41	5	16	1
BB0	22	1	1.24	42	5	15	1
BB0	24	1	1.20	46	5	17	1
BB0	26	1	1.26	34	5	15	1
BB1	1	1	0.54	313	16	41	2
BB1	2	1	0.69	301	15	39	2
BB1	3	1	0.79	263	15	41	2
BB1	4	1	0.86	234	12	41	2
BB1	6	1	0.99	166	10	35	2
BB1	8	1	1.00	80	9	33	4
BB1	10	1	1.11	82	8	34	2
BB1	12	1	1.04	68	6	34	2
BB1	14	1	1.12	66	6	31	2
BB1	16	1	1.17	49	6	39	2
BB1	18	1	1.29	46	6	35	2
BB1	20	1	1.30	39	5	30	2
BB1	22	1	1.33	27	6	38	2
BB3	1	1	0.66	141	9	28	2
BB3	2	1	0.60	107	7	28	2
BB3	3	1	0.78	123	8	25	2
BB3	4	1	0.79	140	9	29	2
BB3	6	1	0.93	124	9	29	2
BB3	8	1	1.03	6	1	2	0
BB3	10	1	1.10	62	6	28	2
BB3	12	1	1.21	42	3	23	2
BB3	14	1	1.10	53	5	23	2
BB3	16	1	0.98	58	7	34	1
BB3	18	1	1.33	25	0	21	1
BB3	20	1	1.38	33	5	20	1
BB3	22	1	1.22	47	5	31	2
BB3	24	1	0.94	63	5	32	2
BB3	26	1	1.35	28	3	25	2
BB3	28	1	1.15	41	4	28	2
BB3	30	1	1.18	41	5	30	2
SC0	0.5	0.5	0.43	366	27	24	2
SC0	1	0.5	0.43	286	20	20	2
SC0	2	0.5	0.59	212	16	22	2
SC0	3	1	0.77	118	11	20	1
SC0	4	1	0.79	127	12	24	2
SC0	6	1	0.96	78	9	21	2
SC0	8	1	0.94	74	9	21	2
SC0	10	1	0.96	81	9	23	2

SC0	12	1	0.98	51	7	21	2
SC0	14	1	1.25	40	7	21	2
SC0	16	1	1.25	43	8	20	2
SC0	18	1	1.23	37	5	17	1
SC0	20	1	1.27	37	7	18	1
SC0	22	1	1.13	46	7	20	1